Research on Engineering Structures & Materials

Volume 5 Issue 3 September 2019 P-ISSN: 2148-9807 E-ISSN: 2149-4088

www.jresm.org

MIM Research Group

The International Journal of **Research on Engineering Structures and Materials (RESM)** is a peer-reviewed open access journal (p-ISSN: 2148-9807; o-ISSN: 2149-4088) published by MIM Research Group. It is published in February, June, September, and December.

The main objective of RESM is to provide an International academic platform for researchers to share scientific results related to all aspects of mechanical, civil and material engineering areas.

RESM aims the publication of original research articles, reviews, short communications technical reports, and letters to the editor on the latest developments in the related fields.

All expenditures for the publication of the manuscripts are most kindly reimbursed by *MIM Research Group*. Thus, authors do not need to pay for publishing their studies in the journal.

The scope of the journal covers (but not limited to) behavior of structures, machines and mechanical systems, vibration, impact loadings and structural dynamics, mechanics of materials (elasticity, plasticity, fracture mechanics), material science (structure and properties of concrete, metals, ceramics, composites, plastics, wood, etc.,), nano-materials performances of new and existing buildings and other structural systems, design of buildings and other structural systems, seismic behavior of buildings and other structural systems, repair and strengthening of structural systems, case studies and failure of structural systems, safety and reliability in structural and material engineering, use of new and innovative materials and techniques in energy systems and mechanical aspects of biological systems (biomechanics and biomimetics).

The topics covered in RESM include:

- Structural Engineering
- Mechanical Engineering
- Material Engineering
- Earthquake Engineering
- Nano-technology
- Energy Systems
- Biomechanics and Biomimetics

Abstracting and Indexing
Please visit http://www.jresm.org for more information.

Graphics and Design

H Ersen Balcıoğlu ersen.balcioglu@usak.edu.tr

Yunus Demirtaş yunus.demirtas@usak.edu.tr

RESEARCH on ENGINEERING STRUCTURES & MATERIALS

Published by MIM Research Group

RESEARCH on ENGINEERING STRUCTURES & MATERIALS

Editorial Board

Editorial Office

Editorial Board Members

Advisory Board Members

Advisory Board Members

In This Issue

Research on Engineering Structures & Materials
MIM Reseach Group Publications
ISSN 2148-9807
http://www.jresm.org

In This Issue

Research on Engineering Structures & Materials
MIM Reseach Group Publications
ISSN 2148-9807
http://www.jresm.org

Research on Engineering Structures & Materials
journal homepage: http://jresm.org
MIM Research Group

Research Article

Comparison of the compression characteristics of 2D braided and circular knitted carbon/epoxy composite tubes

Seçkin Erden*,a,1, Mustafa Ertekinb,2, Gözde Ertekinc,2, Arzu Marmaralıd,2

[1] *Department of Mechanical Engineering, Faculty of Engineering, Ege University, İzmir, Turkey*
[2] *Department of Textile Engineering, Faculty of Engineering, Ege University, İzmir, Turkey*

Article Info

Article history:
Received 06 Dec 2018
Revised 04 Mar 2019
Accepted 18 Mar 2019

Keywords:

Circular knitting;
2D biaxial braiding,
Carbon/epoxy tubular composite;
Braiding angle;
Compression testing

Abstract

Two-(biaxial and triaxial) and three-dimensional braided fabric structures are generally used as structural components in various industries such as ballistic, aerospace, automotive, energy, medical, marine, construction, and sports applications. Due to the advantages of braided structures like high level of uniformity, near net-shape manufacturing, design flexibility, repairability, low manufacturing cost, and damage resistance capability, braiding process have been preferred widely in the manufacturing of composite products.
This study reports the influence of the braiding angle on the compression behaviour of carbon/epoxy tubular composites manufactured based on 2D biaxial braided fabrics, and also their comparison with that of the circular knitted ones. In order to determine the effect of braiding angle, 2D biaxial braids were manufactured by using three different braiding angles (62°, 67°, and 75°). Composite tube specimens were manufactured by vacuum bagging technique and their compression tests were performed. The results imply that braided carbon/epoxy tubes could be more suitable for the cases requiring smaller deformation and higher compressive stresses when compared to the circular knitted ones.

1. Introduction

Braiding is defined as a textile process of intertwining at least three parallel strands (or yarns) of fibre in order to manufacture narrow fabrics like cords and ropes with non-orthogonal fibre orientation, or in order to cover (overbraid) some profiles [1, 2]. In their simplest form, braids consist of single layers of yarns that are diagonally interlaced by moving supply packages around one another, typically by horn gears [3]. The principal difference between the braided and other fabric-processing methods such as weaving and knitting is that woven fabrics are formed by orthogonal interlacing of yarns while knitted fabrics are formed by inter-looping yarns, whereas conventional braiding forms non-orthogonal, multidirectional (typically, two- or three-directional) fabrics without any loops [1]. Braids can be linear products (ropes), curved or plane shell, or solid structures (one, two or three-dimensional fabrics) with constant or variable cross-section, and have closed or open appearance [2]. Braided structures are characterized by bias yarn orientation, and are defined, according to the German Industry Standard DIN 60000, as 2D or 3D fabrics with even thread density and closed fabric appearance. The threads are aligned in the radial direction in a 2D braid, whereas fibres are oriented in through-thickness direction in 3D braids [4]. 2D braiding methods such as sleeve braiding and round braiding are primarily used for textile applications like the production of cords, ropes, or simple cord braids. They can also be used for reinforcement

---

*Corresponding author: seckin.erden@ege.edu.tr
aorcid.org/0000-0002-8560-3585; borcid.org/0000-0002-5492-7982; corcid.org/0000-0003-2150-9255; dorcid.org/0000-0001-6251-0645
DOI: http://dx.doi.org/10.17515/resm2019.80me1206

purposes in special applications. More complex structures become feasible by 3D-braiding methods. These methods are mainly used for the production of three-dimensional reinforcement structures for lightweight construction [5].

Due to its easy production, which does not involve yarn preparatory processes, braids are one of the most cost-effective production methods. From natural fibres such as cotton, silk, wool, and linen, to regenerated and synthetic fibres, metallic fibres, all of yarn compositions can be easily converted into braided structures [6]. Two-(biaxial and triaxial) and three-dimensional braided fabric structures are generally used as structural components in various industries such as civil infrastructure, transportation, ballistic, aerospace and space, automotive, medical, and sports applications [6, 7].

Braiding process can also be preferred for the production of complex shapes with nonregular cross-sections (round, square, triangle, flat, etc.). The nonregular cross-section generates modification of the braiding angle on different areas of the part to be produced. Braiding angle, which is defined as the angle of the fibres with respect to the longitudinal 0 degree-axis, is the most important parameter that determines the cover factor of braided structure [8] (Fig. 1). This angle can be between 1° and 89°, but is usually in the range of 30°–80° in practice [2, 9]. It is closely related to process parameters such as the braid diameter, the take-up speed, and the rotational speed of the carriers [8]. A low carrier speed with a higher take-up speed results in loose braided structures with low braiding angles, which consequently have a low cover factor. But, high carrier speed and low take-up speed result in closely packed braided structures having higher braiding angles and better cover factors [6].

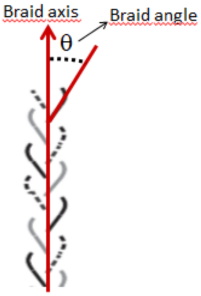

Fig. 1. Braid angle.

Due to the high level of uniformity, near net-shape manufacturing, applicability of a very wide range of shapes, design flexibility, repairability, low manufacturing cost, minimum material waste, and damage resistance capability of braided structures, braiding process have been widely employed in the production of composites [10]. Braided composites that are one type of composite material distinguished by their inter-woven structure are fibrous composite materials that consist of long fibres impregnated by a matrix. Braided composites are defined as angle-ply composites and characterized by the alignment of their yarns that are interlaced diagonally about an axis [11]. Change in this braiding angle parameter will in turn change reinforcement properties of the resulting composite product. Wall thickness, weight fraction or fibre volume fraction, reinforcement angle are some properties of the produced composite that will be affected.

Braiding technique allows continuous production of composite products having variable cross-section, arbitrary shapes, custom material property, custom yarn patterning, and hybrid reinforcement. Biaxial and triaxial reinforcements are achievable by this manufacturing method. Typical examples of braided composite products are aircraft frame [12], engine bleed valve duct, satellite structure parts, scaffolds for articular cartilage [13] and fighter inlet duct [14], propeller blade for turboprop planes [15], field hockey stick [16], and tubes with different shapes and variable cross-sections. Other continuous composite profile production techniques comparable to braiding are filament winding and pultrusion. Filament winding is widespread known for biaxial reinforcements, while pultrusion yields unidirectionally (UD) reinforced composites with constant cross-section. Some example composite products for filament winding are large diameter pipes, blades, and aeroplane fuselage. Pultrusion is well-known for composite profile products for construction industry especially, and smaller diameter pipes.

A considerable amount of literature has been published on braided composites. Rajesh et al. compared dynamic mechanical and free vibration behaviour of natural fibre braided fabric composites with conventional and knitted ones, and reported that the braided yarn fabric enhances the stiffness of the composite structure and hence results in higher natural frequencies while knitted fabric reinforcement enhances modal loss factor of the composite structure due the spiral orientation of yams and large gaps [17]. Rios-Soberanis et al. used textiles of different architecture to manufacture epoxy based composites in order to study failure events under tensile load by using acoustic emission technique which is a powerful characterization tool due to its link between acoustic emission data and fracture mechanics, which makes this relation a very useful from the engineering point of view [18]. Ma and Gao reviewed the development and features of three types of textile structures, including weaving, knitting, and braiding and described the impact tension behaviours and the damage mechanisms of textile structural composites [19]. Ren et al. compared the effectiveness of laminar composite z-directional microfiber reinforcement in improving fracture toughness with that of a 3-D braided 8-layer glass fibre preform/epoxy composite plate. The results showed that the Mode I fracture toughness (G(l)) of the 3-D braided preform reinforced composites are about 10 times of the 2-D layered glass fabric laminar composites [20]. Goyal et al. focused on 2 x 2 biaxial braided composites and developed three-dimensional finite element micromechanics models for two material systems: glass fibre/epoxy matrix and carbon fibre/epoxy matrix [21].

In this study, it is aimed to investigate the effect of the braiding angle on the compression behaviour of carbon/epoxy tubular composites manufactured based on 2D biaxial braided fabrics, and also their comparison with that of the circular knitted ones. In order to determine the effect of braiding angle, 2D biaxial braids were manufactured by using three different braiding angles (62°, 67°, and 75°). Composite tube specimens were manufactured by vacuum bagging technique, and their compression tests were performed.

2. Material and Method

2.1. Material

Carbon 3K yarns (AKSAca, Turkey) were used in the production of braided and circular knitted structures. These yarns were preferred due to their thickness, easy processability and availability in the market. The characteristics of the yarns are listed in Table 1.

Table 1. The characteristics of the Carbon 3K yarns

Property	
Tensile strength	3800 MPa
Tensile modulus	240 GPa
Strain	1.6 %
Density	1.78 g/cm^3
Yield	200 g/1000m
Sizing type & amount	1.0-1.5 %

2.2 Braiding Process

Biaxial 2D braided carbon structures were produced by using a laboratory type braiding machine having 48 spools. Yarns were wound on spools by a winding machine. Carriers move spools in opposite directions along a circular path. Yarn ends are fixed on a mandrel and interlace as shown in Fig. 2. Interlaced yarns move through the convergence zone of the machine, towards the mandrel, which takes the fabric up the loom. The yarns follow helical paths on the mandrel and interlace each time the spools meet [22]. Braiding over Teflon release film coated mandrels allowed the introduction of curvature in the reinforcement without cutting the yarns. In order to determine the effect of braid angle, three different braid angles (62°, 67°, and 75°) were chosen during braiding process.

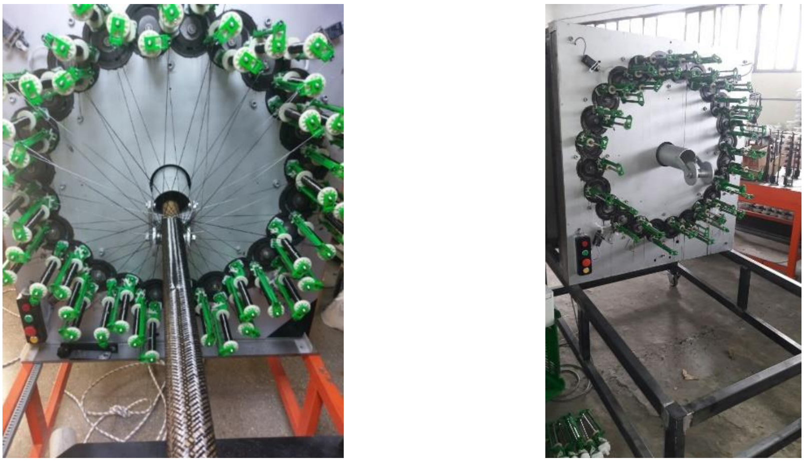

Fig. 2. 2D braiding machine

2.3 Knitting Process

A mechanical single jersey circular knitting machine CKM 01, Faycon (İpekçioğlu Makine, Turkey) was used for the production of circular knitted fabrics (Fig. 3). Carbon fibres were knitted into a circular knitted tube in a single jersey weave pattern [23].

Fig. 3. Mechanical single jersey circular knitting machine.

2.4 Carbon/Epoxy Tube Production

The resin mixture was prepared by mixing KL674A epoxy resin and KL674B hardener in a ratio of 60:40 parts by weight respectively. Resin amount used was calculated by 2:1 weight ratio to the fibres. Two layers of the knitted sock were stretched along the length of the tube and tightly slid onto the iron bar tube with a diameter of 50 mm, to get a thickness of 1.5 mm. Then the structures were vacuum infused (Fig. 4). Similarly, for braided tube production, carbon fibre braided mandrels having a diameter of 50 mm were vacuum infused, again with a 2:1 resin/fibre weight ratio.

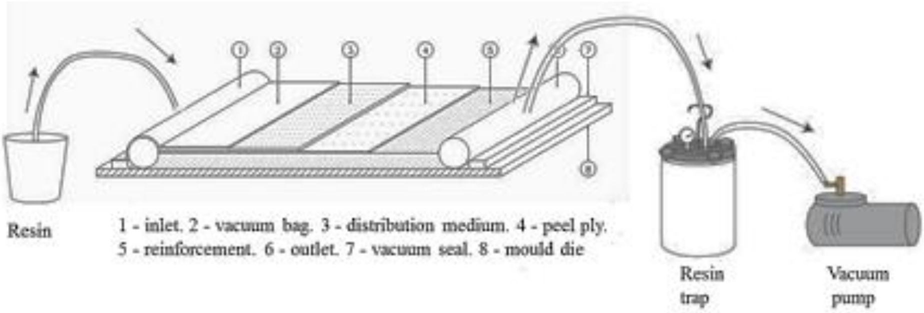

Fig. 4. Typical vacuum infusion lay-up components [23]

The resin mixture was kept in the pot. A transparent plastic tube was dipped into the resin pot and connected to the inlet stuck on the tube. The tube was wrapped in a plastic bag with ends sealed and the rubber hose (outlet) from the waste pot was connected to vacuum so that the resin is drawn through the length of the tube wetting all the sections uniformly. After the resin had wetted out the entire tube length, it was cured at room temperature for 24 hours. After cooling, the cured tube was removed from the iron bar by sliding out.

2.5 Compression Testing

Axial compression tests [24] were conducted on 50 mm long composite tube specimens using a Shimadzu AGIS universal tester equipped with a 100 kN compression apparatus (Fig. 5). Cross-head speed was held constant at 0.033 m/s. Wall thickness values of the composite tubes, which are required for compressive stress calculations, were measured using a digital calliper (Mitutoyo).

(a) (b)

Fig. 5. Universal tension-compression tester (a) and compression testing of tubes (b)

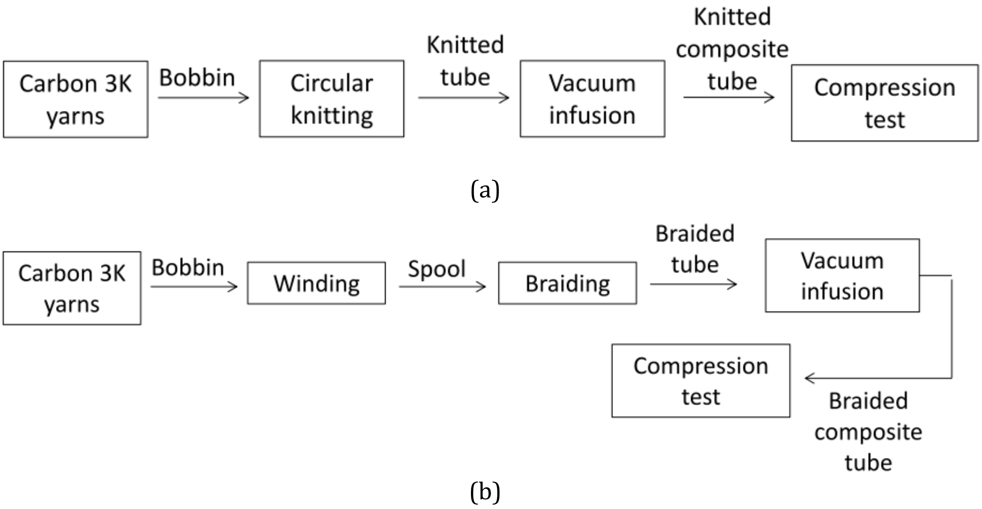

Fig. 6. Methodology of the experiments for the circular knitted composite tubes (a), and the braided composite tubes (b).

3. Results and Discussions

Measured wall thickness values and compression test results of the circular knitted and the three different braided carbon/epoxy tubes are given in Table 2.

Table 2. Compression test data of carbon/epoxy tubes

Property	Knitted	62° braided	67° braided	75° braided
Wall thickness [mm]	1.5	0.45	0.52	0.67
Compression load [N]	3461±108	1514±108	1809±455	4711±707
Compressive stress [MPa]	14.3±0.5	22.6±1.6	23.1±4.0	47.6±8.1

Figure 7 shows a typical stress-strain curve for the compression test results of knitted carbon/epoxy composite tubes. A typical deformed specimen shape is also attached in the figure. The specimens experienced diamond shaped buckling, and then returned to their initial shapes some period after the tests.

Typical compressive behaviours of braided carbon/epoxy composite tubes are also given in Fig. 8. As can be compared from Table 2, increasing braiding angle changes the maximum stress value. This effect is in accordance with the diamond shaped buckling mode mentioned by Harte and Fleck, who state that there are four possible modes of buckling for braided circular tubes in axial compression: Fibre microbuckling, Diamond shaped buckling, Concertina buckling, and Euler buckling [24]. An example image for diamond shaped buckling mode occurring in the specimens can be seen in Fig. 9. The specimens returned to their initial shapes shortly just after the tests.

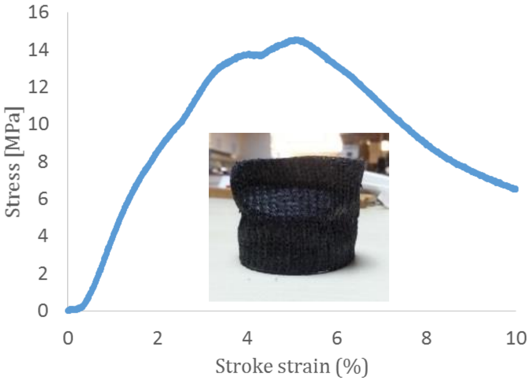

Fig. 7. Typical stress-strain graph for the compression test of knitted tubes.

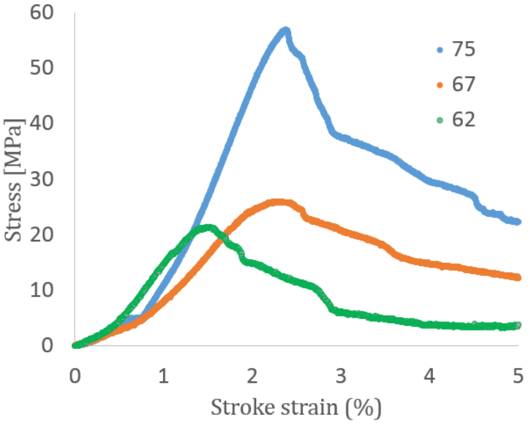

Fig. 8. Typical stress-strain graphs for the compression tests of braided tubes.

When Table 2 is examined, it is clearly seen that wall thickness changes by braiding angle, which in turn affects the compressive stress value of the tube. Knitted tube bears high load, but in expense of having higher wall thickness, which in turn counts for more cost. This allows one to be able to apply only low stress values to these tubes. As they have a highly curved yarn structure, they have low structural strength [25]. When compared to knitted ones, load values that can be carried are smaller for 62° and 67° braided tubes. But, because of their thinner walls, they can bear higher compressive stresses. Contrarily, in the case of 75° braided tube, compression load is higher than the knitted one although its wall thickness is about 2.2 times smaller.

Another outcome is that the strain at maximum stress value is smaller for the braided tubes than that of the knitted ones. Additionally, load value settles at higher strain values for the knitted tubes when compared to the braided ones.

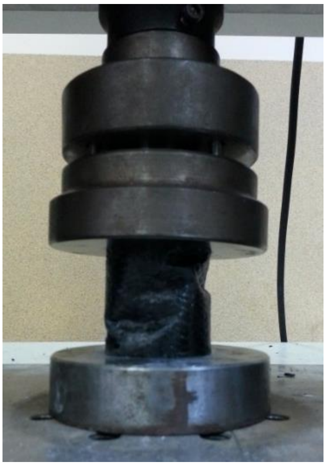

Fig. 9. Diamond shaped buckling of braided tubes during compression testing.

4. Conclusion

Carbon/epoxy tubular composites were successfully manufactured based on 2D biaxial braided fabrics and circular knitted fabrics. Three different braiding angles (62°, 67°, and 75°) were investigated. Compression test results of the composites were analysed. From the results of this study, the following conclusions can be drawn:

- When compressive load was applied, all specimens experienced diamond shaped buckling. This was expected as a consequence of the chosen length/diameter ratio of approximately 1:1. The braided tube composites returned to their original shape immediately after unloading while the knitted tube could recover to its initial shape after a much longer time.
- Braiding technique ended up in thinner tubes when compared to circular knitting. Braided tubes with 62°, 67°, and 75° braiding angle resulted in wall thickness values of 0.45, 0.52, and 0.67 mm, respectively. This was caused by the decrease in the take-up speed. On the other hand, circular knitted tubes had a wall thickness of 1.5 mm. This value is approximately 3.3, 2.9, and 2.2 folds when compared to the case of braided tubes.
- Thinner tubes obtained in case of braiding technique will obviously result in lighter composite structures when compared to the case of knitting technique. This will also reduce the material costs together with transportation, storage, ease of handling, etc.
- When compared to the knitted ones, thinner structures that were obtained by braiding experienced higher compressive stress values as a matter of course. Although the circular knitted tube beared higher load when compared to 62° and 67° braided tubes, it experienced less compressive stress. On the other hand, 75° braided tube could bear higher load even than that of the knitted one despite its thinner wall thickness.
- Knitted tube structure had a higher failure strain or deformation range compared to that of the braided ones.
- The strain at maximum stress is smaller for the braided tubes than that of the knitted ones. Increase in braiding angle seems to increase this strain value, which seems to approach a limit for high braiding angles.
- Load value (Compression stress) settles at higher strain values for the knitted tubes when compared to the braided ones.

- The results imply that braided carbon/epoxy tubes could be more suitable for smaller deformation cases with high compressive stress when compared to the knitted composite tubes.
- Future studies may be conducted for additional braiding angle values. Compression loads/stresses can be analysed as a function of varying cross-sections or wall thickness values.

Acknowledgements

This work was financially supported by Ege University Scientific Research Project Office [grant number 16-MÜH-044].

References

[1] Bogdanovich AE. An overview of three-dimensional braiding technologies, in "Advances in Braiding Technology: Specialized Techniques and Applications." Y. Kyosev (Ed.), Elsevier, UK, 2016, 3. https://doi.org/10.1016/B978-0-08-100407-4.00001-6

[2] Kyosev Y. Braiding Technology for Textiles, Elsevier, UK, 2015.

[3] Hearle JWS. Introduction, in "Advances in 3D Textiles", X. Chen (Ed.), Elsevier, UK, 2015. https://doi.org/10.1016/B978-1-78242-214-3.00001-2

[4] Sontag T, Yang H, Gries T, Ko F. Recent advances in 3D braiding technology, in "Advances in 3D Textiles", X.Chen (Ed.), Elsevier, UK, 2015, 154-155. https://doi.org/10.1016/B978-1-78242-214-3.00007-3

[5] Laourine E. Braided semifinished products and braiding techniques, in "Textile Materials for Lightweight Constructions", C. Cherif (Ed.), Springer-Verlag, Germany, 2016, 291. https://doi.org/10.1007/978-3-662-46341-3_8

[6] Alagirusamy R, Padaki NV. Introduction to braiding, in "Braided Structures and Composites", S. Rana and R. Fangueiro (Eds.), CRC Press, Boca Raton, 2016, 9, 14-15.

[7] Gao YT, Ko FK, Hu H. Integrated design for manufacturing of braided preforms for advanced composites Part I: 2D braiding. Applied Composite Materials, 2013;20(6): 1007-1023. https://doi.org/10.1007/s10443-012-9303-6

[8] Legrand X, Cochrane C, Koncar V. A complex shaped-reinforced thermoplastic composite part made of commingled yarns with an integrated sensor, in "Smart Textiles and Their Applications", V. Koncar (Ed.), Elsevier, UK, 2016, 355. https://doi.org/10.1016/B978-0-08-100574-3.00016-3

[9] Gries T, Stueve J, Grundmann T, Veit D. Textile structures for load-bearing applications in automobiles, in "Textile Advances in Automotive Industry", R. Shishoo (Ed.), CRC Press Boca Raton, 2008, 304.

[10] Arold B, Gessler A, Metzner C, Birkefeld K. Braiding processes for composite manufacture, in "Advances in Composites Manufacturing and Process Design", P. Boisse (Ed.), Elsevier, UK, 2015. https://doi.org/10.1016/B978-1-78242-307-2.00001-4

[11] Carey JP. Introduction to braided composites, in "Handbook of Advances in Braided Composite Materials", J.P. Carey (Ed.), Elsevier, UK, 2017. https://doi.org/10.1016/B978-0-08-100369-5.00001-5

[12] Cichosz JA. (2016). Experimental characterization and numerical modelling of the mechanical response for biaxial braided composites. Dissertation, Technischen Universität München.

[13] Ahn H, Kim K, Park S.Y, Huh J.E, Kim H.J, Yu W-R. 3D braid scaffolds for regeneration of articular cartilage. Journal of the Mechanical Behaviour of Biomedical Materials, 2014; 34: 37-46. https://doi.org/10.1016/j.jmbbm.2014.01.004

[14] Morey B. Molding techniques can replace methods that depend upon cutting, shaping, and autoclaving. Available from: https://advancedmanufacturing.org/advanced-technologies-supplement-processes-reduce-composite-costs/ (Accessed on: 28.02.2019).

[15] Dillow C. Return of the propeller, Scientific American, 2014; 311 (5): 17-21. https://doi.org/10.1038/scientificamerican1114-17
[16] Dawson D, Black S, Sloan J. JEC World 2016, the full report, Composites World, 2016/29/3, Available from: https://www.compositesworld.com/articles/jec-world-2016-the-full-report (Accessed on: 28.02.2019).
[17] Rajesh M, Pitchaimani J. Dynamic mechanical and free vibration behaviour of natural fibre braided fabric composite: comparison with conventional and knitted fabric composites. Polymer Composites, 2018; 39(7): 2479-2489. https://doi.org/10.1002/pc.24234
[18] Rios-Soberanis CR, Rodriguez-Laviada J, Perez-Pacheco E, Sakai T, Wakayama S. Acoustic emission technique applied in textiles mechanical characterization. Proceedings of the 3rd International Conference on Mechatronics and Mechanical Engineering (Icmme 2016), 2017. https://doi.org/10.1051/matecconf/20179507016
[19] Ma PB, Gao Z. A review on the impact tension behaviours of textile structural composites. Journal of Industrial Textiles, 2015; 44(4): 572-604. https://doi.org/10.1177/1528083713503001
[20] Ren J, Kim YK, Rice J. Comparing the fracture toughness of 3-D braided preform composites with z-fibre-reinforced laminar composites. Textile Research Journal, 2011; 81(4): 335-343. https://doi.org/10.1177/0040517510385172
[21] Goyal D, Tang X, Whitcomb JD, Kelkar AD. Effect of various parameters on effective engineering properties of 2 x 2 braided composites. Mechanics of Advanced Materials and Structures, 2005; 12(2): 113-128. https://doi.org/10.1080/15376490490493998
[22] Lomov S, Ignace V. Manufacturing and internal geometry of textiles, in "Design and Manufacture of Textile Composites", A.C. Long (Ed.), CRC Press Boca Raton, USA, 2005. https://doi.org/10.1533/9781845690823.1
[23] Sarkan K, Ertekin M, Erden S. Mechanical testing and production of a carbon/epoxy knitted composite tube. Proceedings of the II. Ulusal Ege Kompozit Malzemeler Sempozyumu (KompEGE II), İzmir, Turkey, November 2013.
[24] Harte A, Fleck N. Deformation and failure mechanisms of braided composite tubes in compression and torsion, Acta Materialia, 2000; 48:1259-1271. https://doi.org/10.1016/S1359-6454(99)00427-9
[25] Tong L, Mouritz AP, Bannister MK. 3D Fibre Reinforced Polymer Composites. Elsevier Science Ltd. Oxford, UK, 2002.

Research on Engineering Structures & Materials
journal homepage: http://jresm.org
Research Group

Research Article

An investigation on the mechanical strength, impact resistance and hardness of SiC filled natural jute fiber reinforced composites

H Ersen Balcıoğlu*,a

Department of Mechanical Engineering, Faculty of Engineering, Usak University, Usak, Turkey

Article Info

Article history:
Received 29 May 2019
Revised 18 July 2019
Accepted 24 July 2019

Keywords:

Silicon Carbide (SiC);
Natural fiber;
Jute/epoxy;
Grain size;
Mechanical properties;
Izod impact test;
Shore D hardness.

Abstract

Natural fibers are a good alternative as economically since they are readily available in fibrous form and can be extracted from plant leaves at very low costs. However, they have lower strength values than synthetic fibers due to their deficiencies in material structure. In this respect, many studies have been carried out by researchers to increase the strength of natural fibers. In this study, mechanical properties, Izod impact toughness, and Shore D hardness behavior of silicon carbide (SiC) filled natural fiber reinforced laminated composites were investigated. In this context, natural jute/epoxy laminated composites were reinforced in different ratios (3%, 6%, and 9%) with SiC powders having different grain size (4.5µ, 9.3µ and 53µ). The test results were compared with the results of unfilled jute/epoxy composites in order to better understand the effects of the fill percentage and grain size on mechanical strength. The produced laminated composites were tested under tensile, compression and impact loads. Scanning Electron Microscopy (SEM) was also performed to analyze the mechanisms of damage of the specimens. The test results showed that the SiC particle size and the percentage of reinforcement were effective on the mechanical behavior of the composite material.

1. Introduction

Composite materials are produced by combining two or more materials at the macro level in order to create new material with superior properties which have better properties than its conventional materials. Composite materials are used as the alternative materials to the conventional materials in many engineering applications due to their superior properties such as lightness, high impact strength, high corrosion resistance, and appropriate thermal properties [1,2]. Fiber reinforced composite materials are the most used composite material type in the structures. Glass, carbon, aramid, and boron fibers are the major reinforcement materials which are used in the fiber-reinforced composite materials. But, either the manufacturing cost of such unnatural fiber is expensive or waste emission into the environment during their manufacturing encourage researchers to find eco-friendlier solutions. Due to low energy cost for the manufacturing of natural fibers without carbon emissions during their manufacturing, this type of fibers is preferred. From an economic point of view, natural fibers exhibit decent price stability, being less dependent on the price of oil than other materials. Natural fibers exhibit lower mechanical properties than their synthetic counterparts as well as have a high degree of fiber to fiber mechanical variability based on growing conditions and plant varieties which lowers their mechanical performance predictability. Natural fibers; such as jute, sisal, and kenaf are the most used as reinforcing the material in polymer composites. Recently, the interest of scientists in

---

*Corresponding author: ersen.balcioglu@usak.edu.tr
a orcid.org/0000-0002-8579-5142

DOI: http://dx.doi.org/10.17515/resm2019.131me0529

natural fibers has been increasing thanks to the use of these fibers as a reinforcement constituent in composites, being eco-friendly and their sustainability. Such that, they have presented a number of studies to investigate and improve the mechanical strength of natural fiber reinforced composites.

Sarikaya et al. [3] have studied the production of epoxy resin composites reinforced by birch, palm, and eucalyptus fibers with resin transfer molding technique and molded fiber production technique combination. The results of studies showed that molded fiber production method had a very promising future for the development of natural fiber reinforced composites. Chegdani et al. [4] investigated the tribomechanical behavior of flax fiber reinforced plastic composites with consideration of the multiscale complex structure of natural fibers. Test results showed that confirm the significant effect of the geometric contact scale on the flax fibers stiffness. Shahinur and Hasan [5] have presented a review article on the comparison of natural and synthetic fiber composite, where matrix materials are polymer particularly, thermoplastic, thermosetting and bio-degradable. Test results showed that although natural composites are cheap and environmentally friendly, they lagging behind synthetic fibers in terms of mechanical strength. So, some studies in the literature aim to improve the weak mechanical strength of natural fiber reinforced composites.

The mechanical properties of natural fiber reinforced polymer composite are the result of the chemical properties of the materials that form the composite and the interface properties at the fiber surface. Structures such as cellulose and lignin on the natural fiber surface create a negative surface environment for the fiber matrix combination. The chemical treatment that applied to the fibers is one of the methods to increase the strength of natural composites. Narin et al. [6] have studied surface modification effects on the mechanical properties of woven jute fabric reinforced laminated composite plates, experimentally. Test results showed that the surface modification process and type of matrix material have dramatically affected the mechanical properties of woven jute fabric reinforced laminated composites. Yan et al. [7] have improved the mechanical properties of flax, linen and bamboo fabric reinforced epoxy composites by alkali treatment. Lui and Dai [8] have done an experimental study to enhance the performance of jute/polypropylene (PP) laminated composites by using treated jute mat with Sodium Hydroxide (NaOH) and Maleic anhydride-grafted polypropylene (MPP) emulsion. The experimental results showed that the treatment process was increased the interfacial shear stress and flexural stress of PP based composites.

Hybridization is another method that increases the strength of natural fiber reinforced composites. Rajesh and Pitchaimani [9] have aims to improve the poor mechanical strength that is associated with the natural fiber composites by reinforcing them in fabric form. Jawaid et al. [10] have improved tensile and flexural performance of natural fiber polymer composite researchers proposed hybridization of two different natural fibers such as oil palm empty fruit bunches and jute fiber. Zivkovic et al. [11] have investigated the influence of moisture absorption on the impact properties of flax, basalt, and hybrid flax/basalt fiber reinforced natural composites. Sanjay and Yogesha [12] have investigated hybridization of natural/glass fiber reinforced polymer composites to develop their applications in the field of engineering and technology. Flynn et al [13] investigated the hybridization effect of on the tensile, flexural and impact performance of carbon/flax hybrid composites. Test results suggest that hybridizing synthetic fibers with natural fibers is an effective method of improving the mechanical properties and controlling vibration damping.

Many studies aimed to improve the properties of composite materials by incorporating different micro or nanoparticles in combination with various forms of powders. The modulus and strength of filled polymers increase with increasing filler content [14]. Matykiewicz et al. [15] have studied the influence of basalt powder addition on thermomechanical properties of natural basalt fiber reinforced epoxy composites. Prasob and Sasikumar [16] have investigated the viscoelastic and mechanical behavior of reduced graphene oxide and zirconium dioxide (ZrO_2) filled jute/epoxy composites at different temperature conditions. Dhanola et al. [17] have studied mechanical, wear and water absorption behavior of luffa-fiber reinforced polyester composites with and without the addition of natural fillers of a ground nutshell, rice husk, and wood powder. Patel and Dhanola [18] have investigated the effect of addition micro filler such as Calcium carbonate ($CaCO_3$), Alumina (Al_2O_3), and Titanium dioxide (TiO_2) on the physico-mechanical properties of Luffa-fiber based polyester composites. Song et al. [19] have performed a study on the effect of carbon black morphology to the thermal conductivity of natural rubber composites. Kumar et al. [20] have investigated mechanical and tribological behavior of Polyamide 66/Polypropylene composites, which filled with nanoclay and short carbon fiber. The results indicate that addition of nanoclay/short carbon fiber in PA66/PP have significant influence on wear under varied abrading distance/loads. Suresha et al. [21] have studied mechanical, tribological and dielectric properties of glass fabric reinforced epoxy composites with and without graphite particulate filler.

The improvement in the mechanical strength of natural composite materials has had a positive effect on their use in various industrial areas. Several studies have been conducted over natural fiber composites in a variety of application areas. Verma and Goh [22] have discussed seawater effect and moisture absorption on the natural fiber reinforced composites, which are used in the marine industries. Luzi et al. [23] have investigated employability of the natural fiber biodegradable composites and nano-cellulose based materials for biomedical applications. Huda et al. [24] have searched the using of natural fiber composites in the automotive industry. Lau et al. [25] have investigated mechanical properties and the manufacturing process of natural fiber composites for structural engineering applications.

Ceramic fillers have been widely used to manufacture composite parts, they often have a low resolution and poor mechanical strength. In this study, mechanical properties, impact toughness, and hardness of jute/epoxy laminated composites, which were filled with ceramic particles, were determined under tensile, compressive, and impact loading condition. For this aim, jute/epoxy composite plates with six layers, which were filled with SiC having 4,5μ, 9,3μ, and 53μ particle size and 0%, 3%, 6%, and 9% reinforcement ratio, were manufactured. In order to better understand the effects of fill percentage and grain size on mechanical strength, the test results were compared with the results of unfilled jute/epoxy laminated composites.

2. Material and Method

2.1. Materials

The natural fiber jute plant is produced from a plant family called Corchorus, which has nearly one hundred varieties. Jute Fiber, which is an annual fiber plant that can extend up to 2-4 m in height, grows mostly in tropical regions. Its homeland is East India and China and Malaysia are the other countries that produce the most. Jute fiber used in the trade is obtained from two types of plants. One of them is Corchorus capsularis and the other is Corchorus olitorius. The capsularis jute is whitish in nature and the olitorious comes in yellow, grey, brown varieties. The jute used for this research is olitorious jute and it was grey in color. As with other cellulosic fibers, the moisture absorbency of the jute fiber is high. Its strength is lower than flax and hemp. The structure of jute fiber contains 60 - 64% cellulose, 20% lignin and 5% pectin. A large part of the jute fibers produced in the world is used for making sacks, fabrics, rope and string (Fig. 1a) [26–28]. In this study, jute woven fabrics with a weight of 300g/m^2, which were weaved by using Jute fibers of Corchorus capsularis type were used (Fig. 1b).

(a) (b)

Fig. 1. (a) Harvested jute bundles [28] and (b) woven jute fabric

The matrix material was procured from Duratek Epoxy and Polyurethane System in Turkey. It has two components as DTE 1100 epoxy and DST 1105 hardener (Fig. 2a). They were prepared by mixing 74/26 in weight, respectively.

(a) (b)

Fig. 2. (a) Epoxy matrix material and (b) SiC particles with three different grain sizes

Silicon carbide (SiC) is composed of tetrahedral of carbon and silicon atoms with strong bonds in the crystal lattice. It was originally produced by a high-temperature electrochemical reaction of sand and carbon. This produces a very hard and strong material. Silicon carbide is not attacked by any acids or alkalis or molten salts up to 800°C. In the air, SiC forms a protective silicon oxide coating at 1200°C and is able to be used up to 1600°C. Table 1 shows the physical and mechanical strength values of silicon carbide. Laminated composite having natural fiber and epoxy components were reinforced with green silicon carbide (SiC) particles from the ceramic oxide group. SiC micro-fillers were procured from Akyol Stone Industry and Trade Inc. in Turkey. SiC ceramic powders having three different grain size such as 4.5µ, 9.3µ and 53µ were used to reinforce the jute/epoxy laminated composites. (Fig. 2b). Each silicon carbide particle was added to the epoxy resin at 3%, 6%, and 9%, respectively, based on the weight of the matrix material.

Table 1. The physical and mechanical strength values of silicon carbide

Density (g/mm^3)	Bulk Modulus (GPa)	Compressive Strength (MPa)	Yield Strength (MPa)	Poisson's Ratio	Shear Modulus (GPa)	Tensile Strength (MPa)	Young's Modulus (GPa)	Melting Point (K)
4.36-4.84	100-176	1395	1245	0.35-0.37	51	240	137	1955

2.2. Manufacturing of Laminated Composite

Fabrication of composite was done by a conventional method called hand lay-up method. Hand lay-up method has been a widely explored technique of fabricating natural fiber based composites owing to its simplicity, cost-effectiveness, and flexibility. In order to manufacture natural laminated composite material, firstly woven jute fabrics were cut to 100x80cm (Fig. 3a). Secondary reinforcement material SiC ceramic powders were prepared by weighing according to the weight of the matrix material. Then, two-component matrix material and SiC powders were mixed in the same vessel along 2 minutes at 1500rpm (Fig. 3b). At this stage, the mixture of resin should not be mixed at high speed and for a long time. The heat, which generated by the friction of the molecules during the mixing, reacts the epoxy and the hardener. In this case, the pot life of the epoxy matrix is shortened. After the mixture was prepared, SiC reinforced epoxy resin was impregnated with jute woven fabric by means of a roller brush (Fig. 3c).

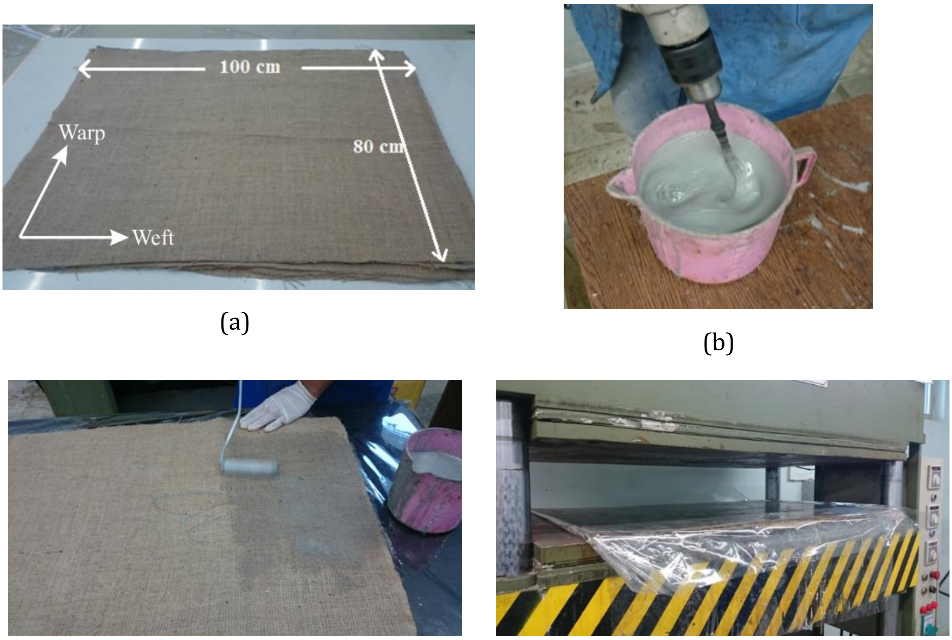

(a)

(b)

(c)

(d)

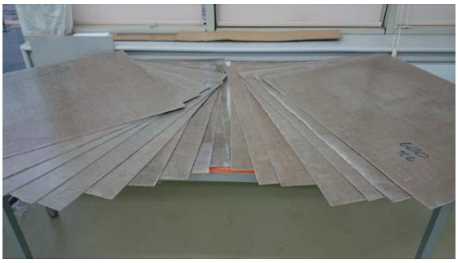

(e)

Fig. 3. Manufacturing stages of SiC powders filled jute/epoxy laminated composites

The hand lay-up process was carried out on a Teflon film which can withstand temperatures up to 250oC. This film acts as a mold release agent between the hydraulic press and the composite plate. After the impregnation process, the semi-finished composite plates were allowed to cure for 60 min at 100oC under pressure of 4MPa in the time-temperature-pressure controlled hydraulic press (Fig. 3d). After the curing process was completed, the composite plates were cooled along 24 h under the same pressure in order to avoid the warping effect. After cooling, the composite plates were separated from the mold separator Teflon film. The edges of the composite plate were cut with a circular saw and then ready for mechanical testing (Fig 3e).

2.3. Determination of Mechanical Properties

Tensile properties were determined according to the ASTM D3039-76 test standard. This test method determines the in-plane tensile properties of polymer matrix composite materials reinforced by high-modulus fibers [30]. Longitudinal Young modulus E_1 and longitudinal tensile strength T_1 were obtained by using the wrap direction of jute/epoxy laminated composite specimens. Transverse Young modulus E_2 and transverse tensile strength T_2 were also obtained by using the weft direction of composite specimens. The tensile strengths in the warp and weft directions (T_1 and T_2) were determined by dividing the failure load by the cross-sectional area of the wrap and weft specimens, respectively.

Shear properties were determined according to the ASTM D3518M-13 standard test method. This test method determines the in-plane shear response of polymer matrix composite materials. The composite material form is limited to a continuous-fiber-reinforced composite ±45° laminate capable of being tension tested in the laminate roving direction [31]. In order to define the in-plane shear modulus, G_{12}, a specimen which fiber direction is 45^o according to the woven direction was used. The in-plane shear modulus, G_{12}, was defined by using Eq. 1, where E_{45} is elasticity modulus in 45^o woven direction and ϑ_{12} is major Poisson's ratio[32]. Poisson's ratio ϑ_{12} was accepted as 0.25 according to studies in the literature [33,34].

$$G_{12} = \frac{1}{\frac{4}{E_{45}} - \frac{1}{E_1} - \frac{1}{E_2} + \frac{2\vartheta_{12}}{E_1}} \tag{1}$$

The elasticity modulus of the polymer matrix composite materials was calculated with the help of Hooke's Law, which formulated the stress-strain relationship of the material. Epsilon brand extensometer with a 50-mm gauge length was used for the unit deformation value of the material that needed in the calculation (Fig.4).

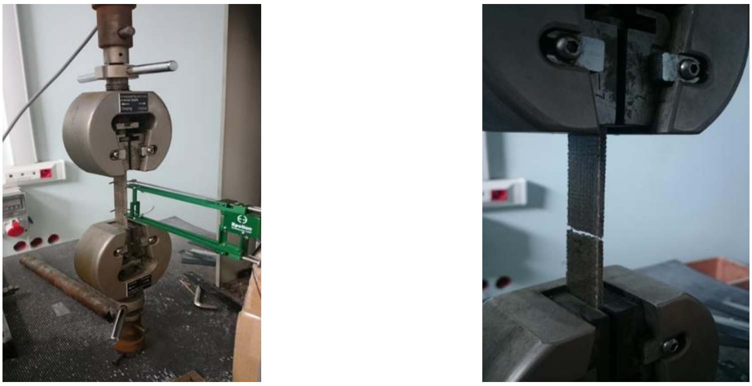
(a) (b)

Fig. 4. (a) Tensile test configuration and (b) tension damage

Compressive properties were determined according to the ASTM D3410-87 standard test method. This test method determines the in-plane compressive properties of polymer matrix composite materials reinforced by high-modulus fibers [35]. The wrap and weft compressive strength of laminated composite specimens (C_1 and C_2) were calculated by dividing the failure load to the cross-sectional area of the specimens in the longitudinal and transverse direction, respectively. The compressive test setup and the test specimen damaged by compression was shown in Fig. 5.

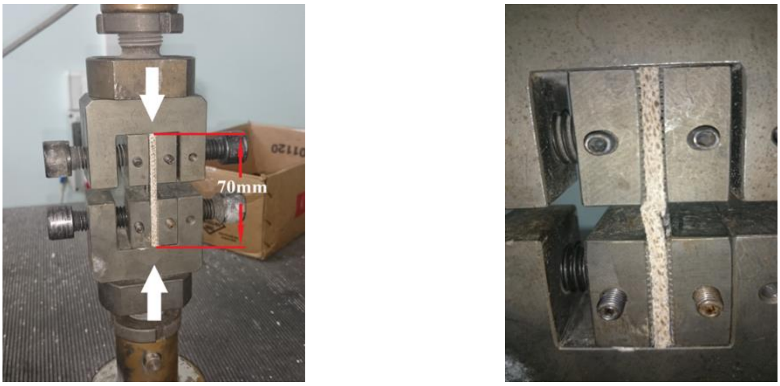

(a) (b)

Fig. 5. (a) Compression test configuration and (b) compression damage

The produced laminated composites were cut with a diamond saw and the tensile, compression and impact test samples were obtained. All mechanical strength tests were carried out in U-Test brand universal tensile-compressive test machine under room conditions. For each test parameter, five samples were tested at a crosshead deformation velocity of 1mm/min. The average of the results of these five tests was accepted as a significant strength value.

2.4. Determination of Izod Impact Strength

Impact strength is one of the properties usually included in the materials characterization programs of the composite materials manufacturers. The different methods used to determine impact strength try to simulate service conditions associated with high strain rates. Izod test is high strain rate tests that measure the energy absorbed by a material during high-speed impact. This test allows the elastic capability of reinforced and unreinforced plastics for energy absorption prior to any permanent damage (yield or microcrack) to be demonstrated. The Izod pendulum is one of the most widely used tests by the plastic industry. The results from these tests are highly dependent on specimen size, notch geometry, the amount and rate of loading, and the method of support of the specimen. Thus, they do not provide intrinsic material behavior properties, but the results can be used for relative comparisons if all test conditions are held constant.

The specimens were tested following ASTM D-256 standard for impact strength. This test estimates the energy to break standard test specimens under the influence of specimen mounting, notching and pendulum velocity at impact [36]. The geometry of the rectangular test specimen (80x10x3 mm) corresponds to the ASTM D-256 specification and the dumbbell-shaped specimen is according to the ISO 527 type 1A standard. A single edge 45° V-shaped notch (tip radius 0.25 mm, depth 2 mm) was milled in the middle of the test specimens (Fig. 6a). Izod impact test was performed with a pendulum apparatus (OTS model XB-OTS-C500) with 5J capacity using conventional V-notched specimens (Fig. 6b). Five replicate tests were conducted for each material parameters.


(a) (b)

Fig. 6. (a) Impact test sample and (b) Izod impact test machine

2.5. Shore Hardness Test

Shore hardness meter is one of the most widely used devices to determine hardness characterization of materials. The hardness is measured by the depth of indentation caused by a rigid ball under a spring load or dead load, the indentation being converted to hardness degrees on a scale ranging from 0 to 100. The hardness scale from 0 to 100 is chosen such that ‘0’ represents a rubber having an elastic modulus of zero and ‘100’ represents a rubber having infinite elastic modulus.

Hardness tests were performed by adhering to ASTM D2240 testing procedures. This test procedure describes determining of indentation hardness of substances classified as thermoplastic elastomers, vulcanized (thermoset) rubber, elastomeric materials, cellular materials, gel-like materials, and some plastics [37]. Tronic trend mark Shore D Durometer Hardness Tester was used to measure the depth of penetration of the loaded indenter into unfilled and filled jute/epoxy laminated composites respectively (Fig. 7 (a)). The hardness measurements were made in two different directions as the surface and thickness of the sample. Hardness values were obtained from eight different points at a 10 mm interval along the length of each sample (Fig 7(b).

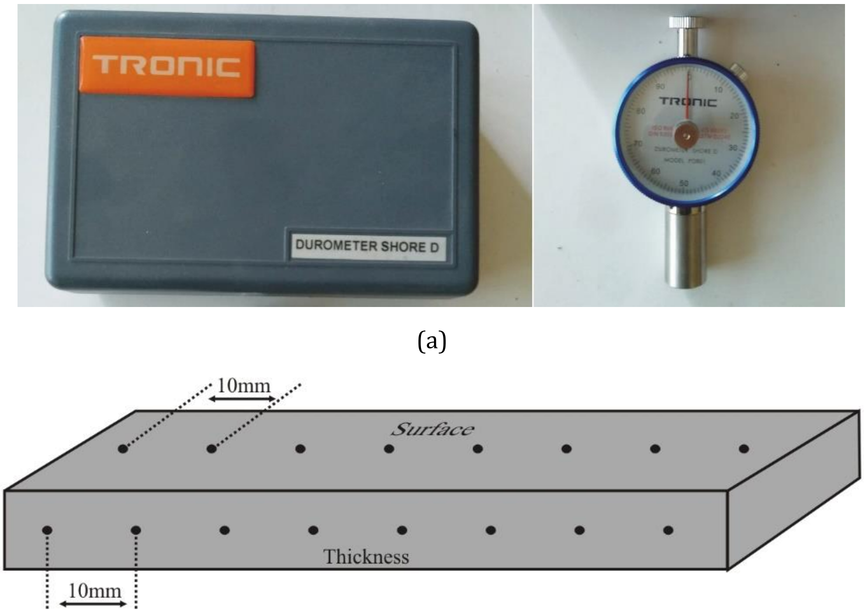

(a)

(b)

Fig. 7. (a) Shore D durometer hardness tester and (b)specimens measure points

2.6. Morphological Characterization

Studies on the morphology of the composites were carried out using scanning electron microscopy (SEM). Micrographs of the surfaces of tensile fractured specimens were taken using Phillips XL30CP. An accelerating voltage of 15 kV was used to collect the SEM images.

3. Result and Discussion

In this study, tensile, compressive and impact behaviors of jute/epoxy composites, which were filled with different percentages of silicon carbide powders, were investigated. In order to investigate the enhancement in mechanical strength, the test results were compared with the results of unfilled jute/epoxy laminated composites. The obtained results were summarized below.

3.1. Results of Tensile Tests

Tensile strengths (T) and elasticity modules (E) of the material in two different weaving directions (warp and weft) were determined. The load-displacement curves of the jute/epoxy laminated composites were obtained for each SiC filling ratio and grain size during the tests. The load-displacement behaviors of filled and unfilled jute/epoxy composites are given in Fig. 8. In order to make Fig. 8 more clear, the only result of the 6% filled composite tests were compared with the results of unfilled composites. As shown in Fig. 7, jute/epoxy composites were damaged as brittle under tensile loading.

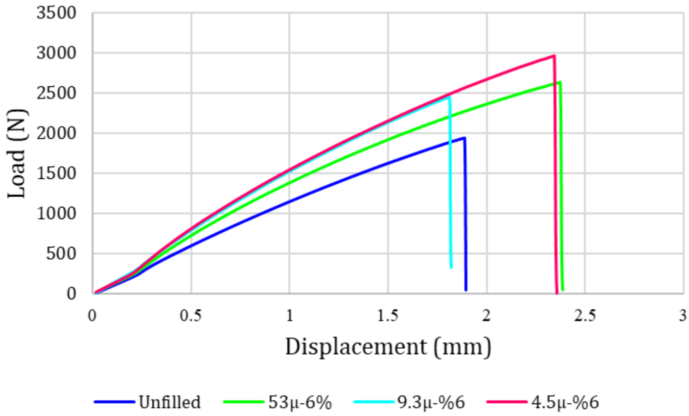

Fig. 8. The load-displacement curve of jute/epoxy with filled and unfilled composite under tensile load

The elasticity modulus of the filled and unfilled jute/epoxy laminated composites were given in Table 2 presents according to the direction of warp and weft. When Table 2 is examined, it was seen that the percentage of filling and powder grain size were effective on the modulus of elasticity of the laminated composite plates. The maximum elasticity modulus in the wrap direction (E1) was obtained as 6332.63 MPa from the samples that filled silicon carbide with 4.µ in the ratio of 6%. The minimum elasticity modulus was obtained as 5083.41MPa in the unfilled sample in the same weaving direction. The maximum and minimum elastic modulus values of Weft direction were 6378.45 MPa and 4969.66 MPa, respectively. In terms of weaving direction, it is seen that the results are close to each other. This result shows that yarns with similar physical properties in the direction of warp and weft are used in woven jute/fabric.

Table 2. Elasticity modulus values of jute/epoxy with filled and unfilled in warp and weft weaving direction

Filling Percentage	E1 (MPa)				E2 (MPa)			
	Unfilled	53µ	9.3µ	4.5µ	Unfilled	53µ	9.3µ	4.5µ
0	5083.41	-	-	-	4969.66	-	-	-
3	-	5633.56	5789.33	5847.99	-	5646.64	5799.30	6007.82
6	-	5721.57	6025.65	6332.63	-	5731.82	6168.49	6378.45
9	-	5367.16	5520.86	5768.64	-	5423.16	5434.66	5516.26

Considering the grain size and filling percentage, it was seen that the elasticity modulus of jute/epoxy composites improved up to 24% and 28%in the direction of warp and weft, respectively.

Table 3 showed the maximum tensile strength of jute/epoxy with filled and unfilled in the wrap (T1) and weft (T2) weaving directions. The maximum and minimum tensile strength in the wrap direction were 65.88 MPa and 52.12 MPa, respectively. In the weft direction, the maximum and minimum of tensile strength values were obtained 64.39 MPa and 54.55 MPa, respectively. Test results showed that the tensile strengths obtained from different weaving directions were similar. When considering the tensile strengths of unfilled jute/epoxy laminated composites, the tensile strength of filled jute/epoxy composites enhanced up to 24% in the warp direction and 18% in the direction of weft. This may be due to good particle dispersion and strong polymer/filler interface adhesion for effective stress transfer.

Table 3. Tensile strength values of jute/epoxy with filled and unfilled in warp and weft weaving direction

Filled Percentage	T1 (MPa)				T2 (MPa)			
	Unfilled	120	600	1000	Unfilled	120	600	1000
0	52.12	-	-	-	54.55	-	-	-
3	-	57.09	59.28	62.06	-	57.63	58.19	61.46
6	-	61.86	64.19	65.88	-	61.82	63.22	64.39
9	-	56.27	57.10	58.80	-	55.76	56.59	57.51

Table 4 presents the shear modules of filled and unfilled jute/epoxy laminated composites. As shown in Table 3, the maximum shear modulus (G12) is 1236.93 MPa and the minimum shear modulus is 1022.30 MPa. It has seen that powder filling process increased the shear modulus of the jute/epoxy laminated composite up to 21% depending on the granule size and the filling percentage.

Table 4. Shear modulus of jute/epoxy with filled and unfilled in warp and weft weaving direction

Filled Percentage	G12			
	Unfilled	120	600	1000
0	1022.30	-	-	-
3	-	1051.34	1073.24	1148.46
6	-	1176.70	1201.68	1236.93
9	-	1044.22	1117.01	1202.53

3.2. Results of Compression Tests

Compression tests were carried out in two different loading directions depending on the warp and weft directions of the jute fabric. Fig. 9 shows representative load-displacement curves for unfilled and %6 SiC filled jute/epoxy test specimens under a compression load in wrap direction. The load-displacement curves of all samples were not given because the compression behavior was similar for other samples and the graph was more understandable. All specimens showed an initial linear increase in the measured load, and after a bend of the curve, the compression load increased at a lower rate, indicating the first appearance of irreversible damage within the laminates. When the maximum compression load was reached, the sample slowly deformed and damaged. Unlike from tensile damage, filled and unfilled jute/epoxy composites were damaged in a ductile manner under compression load.

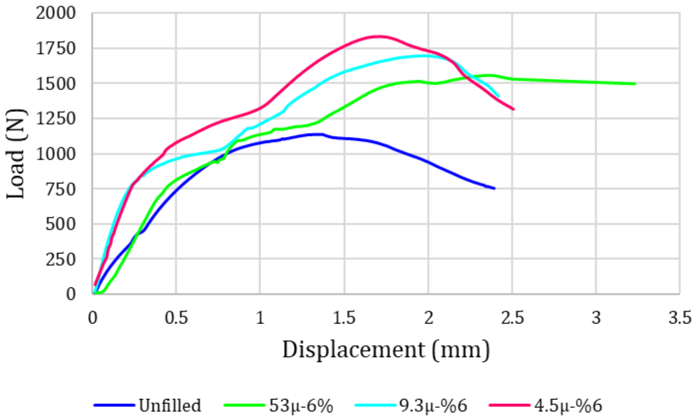

Fig. 9. The load-displacement curve of jute/epoxy with filled and unfilled composite under compression load

Table 5. Compression strength values of jute/epoxy with filled and unfilled in warp and weft weaving direction

Filling Percentage	C1 (MPa)				C2 (MPa)			
	Unfilled	53µ	9.3µ	4.5µ	Unfilled	53µ	9.3µ	4.5µ
0	45.10	-	-	-	45.19	-	-	-
3	-	51.73	54.33	55.58	-	49.60	52.26	54.13
6	-	55.37	56.88	59.02	-	53.27	56.77	58.04
9	-	47.02	48.82	51.00	-	48.03	49.09	52.29

Table 5 showed the average compressive strengths of filled and unfilled jute/epoxy laminated composites, which obtained from the wrap (C1) and weft (C2) direction. The maximum tensile strength values of C1 and C2 were 59.02 MPa and 58.04 MPa, respectively. Similarly, minimum compressive strengths for C1 and C2 were obtained as 45.10MPa and 49.19 MPa. When the compressive strengths obtained from the warp and weft weaving directions were compared, the values were close to each other. It has been seen that the powder filling process increased the compressive strength of the jute/epoxy laminated composites up to 31% in the warp direction and up to 28% in the weft direction, depending on the powder size and filling percentage. In addition, it was observed that the powder filling process increased the deformation ability of jute/epoxy composites under compression load.

3.3. Results of Izod Impact Tests

The complete set of ten different combinations of jute/epoxy composites were adopted for understanding filling percentage and granule size effect on the impact strength of the composites by the Izod impact test. The absorbed energy, i.e. the energy needed to break the specimen, provides an interesting trend of the impact strength in the considered ranges of the fillers weight contents. The impact toughness (strength) is determined by the loss of energy of the pendulum or determined by precisely measuring the loss of height in the pendulum's swing. Table 6 shows the absorbed energy and impact toughness of filled and unfilled jute/epoxy laminated composites. Test results showed that the powder filling process increased the energy absorption capacity and impact toughness of the jute/epoxy laminated composites up to 37% and 15%, respectively.

Table 6. Izod impact test results of filled and unfilled jute/epoxy composites

Filling Percentage	Absorbed Energy (J)				Impact Toughness (kJ/m^2)			
	Unfilled	120	600	1000	Unfilled	120	600	1000
0	0.176	-	-	-	6.285	-	-	-
3	-	0.193	0.210	0.239	-	6.395	6.938	6.973
6	-	0.217	0.222	0.242	-	7.083	7.108	7.230
9	-	0.203	0.218	0.225	-	6.620	6.821	6.922

The changes in absorbed energy and impact toughness for jute/epoxy laminated composites according to the filling percentage were showed in Fig. 10. The percentage of filling is effective on the impact behavior of jute/epoxy composite material. Among various filling percentage and granule size, jute/epoxy composite, which was reinforced with %6 filling percentage and 4.5µ granule size, had the highest improvement in absorbed energy and impact toughness. SiC filling into jute epoxy up to 6% increased the absorbed energy and impact toughness of the material. After 6% filled percentage, these values decreased.

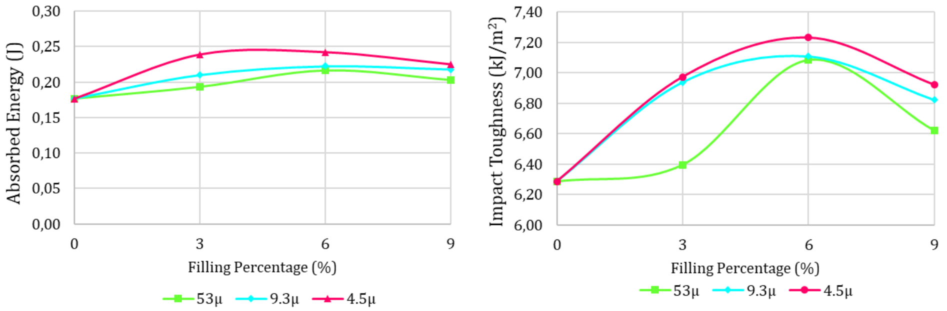

(a) (b)

Fig. 10. Change in absorbed energy and impact toughness according to filling percentage

3.4. Results of Shore Hardness Tests

Shore-D Hardness test was applied to filled and unfilled jute/epoxy composites that measured 80x15x3 mm. The average of these measured eight hardness values was accepted as the hardness of the sample. Table 7 showed the hardness values of filled and unfilled jute/epoxy composites, which were measured in the direction of surface and thickness. The maximum surface and the maximum thickness hardness values were measured as 81.88 and 81.33 respectively. The minimum hardness values were measured as 65.38 and 66.33 in surface and thickness directions, respectively. While, the maximum hardness values were measured in the specimen, which was filled SiC with 9.3µ in 6% filling ratio. On the other hand, the minimum hardness values were measured in the unfilled specimen.

Table 7. Shore D hardness test results of filled and unfilled jute/epoxy composites

Filling Percentage	Surface Hardness				Thickness Hardness			
	Unfilled	53µ	9.3µ	4.5µ	Unfilled	53µ	9.3µ	4.5µ
0	65.38	-	-	-	66.33	-	-	-
3	-	68.50	70.13	74.75	-	71.67	72.33	73.00
6	-	71.75	81.88	70.50	-	77.67	81.33	67.33
9	-	67.13	79.00	73.13	-	68.33	73.33	69.00

When the hardness values of the samples, which have different granule size and different filling percentage, were compared with the hardness values of the unfilled samples, it was seen that the hardness value in the direction of surface and thickness increased up to 24% and 22%, respectively. In order to understand the effects of the filling percentage and the granule size on the hardness, the changes in the hardness values obtained from the surface and thickness direction were illustrated in Fig. 11.

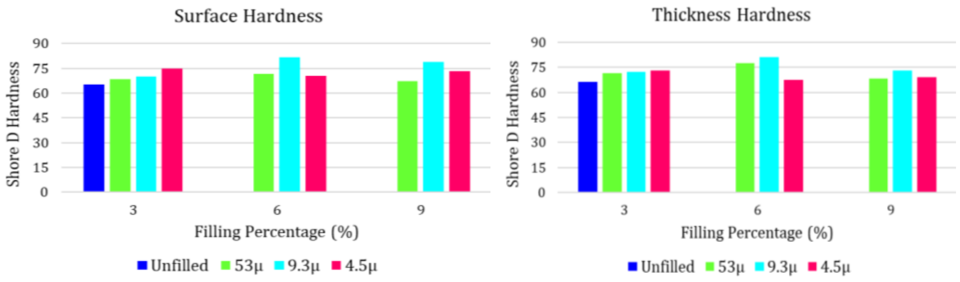

(a) (b)

Fig. 11. Changes of Shore D hardness values according to filling percentage

The hardness value increases when the granule size decreases in samples having a filling ratio of 3%. There is no linear relationship between granule size and hardness in samples with a filling ratio of 6% and 9%. In samples with a filling ratio of 6% and 9%, hardness value of specimens with 4.5µ granule is less than specimens with 9.3µ granule size. This indicates that the powder filling process should not be applied at high filling percentages for small grain sizes in order to avoid agglomeration of the powders.

3.5. Results of Morphological Characterization

The distributions of SiC ceramic powder particles in jute/epoxy were visualized by scanning electron microscopy (SEM) and they were presented in Fig. 12. The voids, which can be seen between SiC Particle and matrix, clearly indicate the poor interaction between them. Further, different sizes and irregular shapes of the SiC fillers were evident in figures. Fibers, which prevented plastic deformation of the matrix, can be seen in Fig. 12. As the adhesion of the matrix and SiC particles is poor, the matrix can deform independently until the filler particles restrict the deformation. However, as filler percentage reaches %6, the observed plastic deformation characteristic seems to have decreased as the deformability of the matrix is limited earlier. Therefore, SEM observation of jute/epoxy laminated composites provides visual evidence for the poor mechanical properties and their trends against filler percentage.

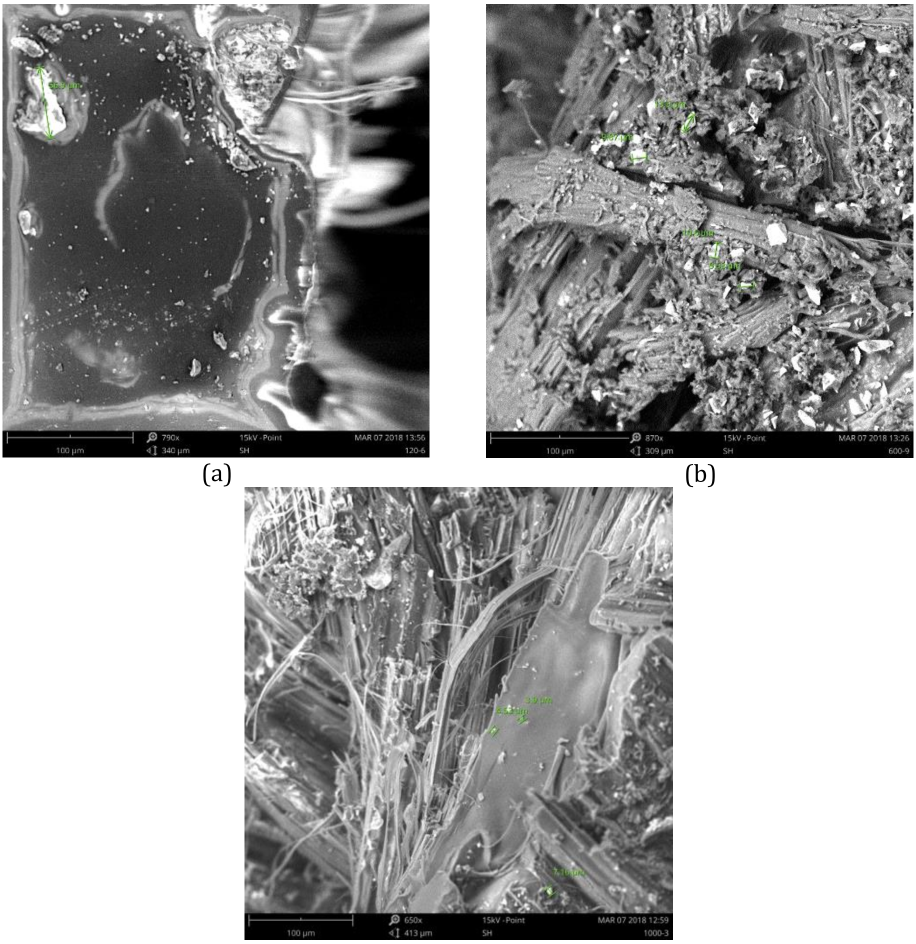

(a) (b)

(c)

Fig. 12. SEM photos of jute/epoxy laminated composites filled with (a) 53µ, (b) 9.3µ, and (c) 4.5µ SiC powders

A good dispersion was observed for jute/epoxy composite samples containing 3-6% SiC particles by weight. As the filler percentage for %9, significant filler agglomeration was indicated. This agglomeration factor contributes to the poor stress transfer from matrix to filler resulting in poor properties. Figure 13 also illustrates a state where agglomeration is observed visually. The results obtained from mechanical tests confirm this image.

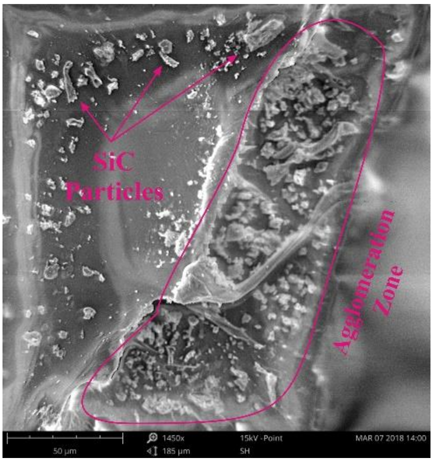

Fig. 13. Agglomeration of SiC particles with a size of 4.5µ

4. Conclusion

In this study, the effects of SiC filling process with different amounts and granule size on the mechanical, impact and hardness behaviors of natural jute fabric reinforcement laminated composites were investigated. Test results were compared with the results of unfilled jute/epoxy composite material to understand the effect of powder size and filling amount on the strength of jute/epoxy composite. Experimental findings were summarized as substances.

- The results obtained from the tensile and compression tests showed that the mechanical properties improved with the reduction of grain size. Accordingly, strength values of filled jute/epoxy laminated composites, such as elasticity modulus, shear modulus, and tensile strength, increased up to 18-28% by reduction of granule size, when compared to the unfilled jute/epoxy composite. Similarly, considering the compression values of unfilled jute epoxy composites, SiC filling provided up to 30% improvement in the compression strength of the jute/epoxy composites. It has also been seen from SEM photos where the SiC particles having small granule size were better positioned to the fiber-matrix interface voids. On the other hand, there is no linear relationship due to aggregation phenomenon between the filling percentage increasing and the mechanical strength.
- Although the tensile and compression tests were performed at the same deformation rate, the failure time of the sample in the compression test is much shorter than the tensile test. The main reason for this is that the fibers are vulnerable to compression load and that the delamination damage of the layers occurs at lower loads under compression loading.
- The jute fabric weaving direction (warp and weft) did not have a significant effect on the mechanical strength of the natural composite material. When the tensile strengths of the warp and weft directions of the samples having the same granule size and filling percentage were compared, it was seen that the tensile strengths were higher in the warp direction up to 2%. If a similar comparison was made for compressive strengths, it is seen that the strength difference due to weaving direction was around 9%.

- Izod impact tests have shown that SiC particles contribute to the impact resistance by delaying the plastic deformation of the epoxy matrix.

- Hardness strength behavior depends on the percentage of filling and SiC particle size. For a filling percentage of 3%, there is a linear relationship between grain size and fill percentage increase. For fill percentages of more than 3%, the hardness increase is affected by the grain size. This situation was due to the agglomeration, which occurred the excess amount of filling.

- According to the results obtained from tensile, compression, impact and hardness measurement tests, it can be said that SiC filling into natural jute fiber reinforced polymer composites has a positive effect on their mechanical performance. Two important parameters to be considered during the filling process are the granule size and filling percentage of the SiC granules. Test results show that small size granules are better dispersed than large size ones. In addition, SiC particles may have agglomeration or homogeneous dispersion problems if fill with more than 6% by weight of the matrix.

- Although SiC filling of a certain ratio and granule size enhance the mechanical strength of natural jute / epoxy composites, it increases the production costs too. In this context, the producer should consider the required strength / cost ratio.

References

[1] Balcıoğlu HE, Sakin R, Gün H. The design of multi-sample flexural fatigue device and fatigue behavior of glass/epoxy laminated composites. Res Eng Struct Mater 2018;4:279-96. https://doi.org/10.17515/resm2018.67me0917

[2] Kaybal HB, Ulus H, Tatar AC, Demir O, Avcı A. Influence of seawater on mechanical properties of SiO2-epoxy polymer nanocomposites. Res Eng Struct Mater 2019;5:147-54. https://doi.org/10.17515/resm2018.61is0802

[3] Sarikaya E, Çallioğlu H, Demirel H. Production of epoxy composites reinforced by different natural fibers and their mechanical properties. Compos Part B Eng 2019;167:461-6. https://doi.org/10.1016/j.compositesb.2019.03.020

[4] Chegdani F, Wang Z, El Mansori M, Bukkapatnam STS. Multiscale tribo-mechanical analysis of natural fiber composites for manufacturing applications. Tribol Int 2018;122:143-50. https://doi.org/10.1016/j.triboint.2018.02.030

[5] Shahinur S, Hasan M. Natural Fiber and Synthetic Fiber Composites: Comparison of Properties, Performance, Cost and Environmental Benefits. Elsevier Ltd.; 2019. https://doi.org/10.1016/B978-0-12-803581-8.10994-4

[6] Karabulut N, Aktaş M, Balcıoğlu HE. Surface Modification Effects on the Mechanical Properties of Woven Jute Fabric Reinforced Laminated Composites. J Nat Fibers 2018;00:1-15.

[7] Yan L, Chouw N, Yuan X. Improving the mechanical properties of natural fibre fabric reinforced epoxy composites by alkali treatment. J Reinf Plast Compos 2012;31:425-37. https://doi.org/10.1177/0731684412439494

[8] Liu XY, Dai GC. Surface modification and micromechanical properties of jute fiber mat reinforced polypropylene composites. Express Polym Lett 2007;1:299-307. https://doi.org/10.3144/expresspolymlett.2007.43

[9] Rajesh M, Pitchaimani J. Mechanical Properties of Natural Fiber Braided Yarn Woven Composite: Comparison with Conventional Yarn Woven Composite. J Bionic Eng 2017;14:141-50. https://doi.org/10.1016/S1672-6529(16)60385-2

[10] Jawaid M, Abdul Khalil HPS, Abu Bakar A. Woven hybrid composites: Tensile and flexural properties of oil palm-woven jute fibres based epoxy composites. Mater Sci Eng A 2011;528:5190-5. https://doi.org/10.1016/j.msea.2011.03.047

[11] Živković I, Fragassa C, Pavlović A, Brugo T. Influence of moisture absorption on the impact properties of flax, basalt and hybrid flax/basalt fiber reinforced green composites. Compos Part B Eng 2017;111:148-64. https://doi.org/10.1016/j.compositesb.2016.12.018

[12] Sanjay M, Yogesha B. Studies on Natural/Glass Fiber Reinforced Polymer Hybrid Composites: An Evolution. Mater Today Proc 2017;4:2739-47. https://doi.org/10.1016/j.matpr.2017.02.151

[13] Flynn J, Amiri A, Ulven C. Hybridized carbon and flax fiber composites for tailored performance. Mater Des 2016;102:21-9. https://doi.org/10.1016/j.matdes.2016.03.164

[14] Shivamurthy B, Udaya Bhat K, Anandhan S. Mechanical and sliding wear properties of multi-layered laminates from glass fabric/graphite/epoxy composites. Mater Des 2013;44:136-43. https://doi.org/10.1016/j.matdes.2012.07.059

[15] Matykiewicz D, Barczewski M, Knapski D, Skórczewska K. Hybrid effects of basalt fibers and basalt powder on thermomechanical properties of epoxy composites. Compos Part B Eng 2017;125:157-64. https://doi.org/10.1016/j.compositesb.2017.05.060

[16] PA P, M S. Viscoelastic and mechanical behaviour of reduced graphene oxide and zirconium dioxide filled jute/epoxy composites at different temperature conditions. Mater Today Commun 2019;19:252-61. https://doi.org/10.1016/j.mtcomm.2019.02.005

[17] Dhanola A, Bisht AS, Kumar A, Kumar A. Influence of natural fillers on physico-mechanical properties of luffa cylindrica/ polyester composites. Mater Today Proc 2018;5:17021-9. https://doi.org/10.1016/j.matpr.2018.04.107

[18] Patel VK, Dhanola A. Influence of CaCO3, Al2O3, and TiO2 microfillers on physico-mechanical properties of Luffa cylindrica/polyester composites. Eng Sci Technol an Int J 2016;19:676-83. https://doi.org/10.1016/j.jestch.2015.10.005

[19] Song J ping, Tian K yan, Ma L xiang, Li W, Yao S chune. The effect of carbon black morphology to the thermal conductivity of natural rubber composites. Int J Heat Mass Transf 2019;137:184-91. https://doi.org/10.1016/j.ijheatmasstransfer.2019.03.078

[20] Ravi Kumar BN, Suresha B, Venkataramareddy M. Effect of particulate fillers on mechanical and abrasive wear behaviour of polyamide 66/polypropylene nanocomposites. Mater Des 2009;30:3852-8. https://doi.org/10.1016/j.matdes.2009.01.034

[21] Suresha B, Gope PC, Renukappa NM, Siddaramaiah. Mechanical and Tribological Properties of Glass-Epoxy Composites with and Without Graphite Particulate Filler. J Appl Polym Sci 2006;103:2472-80. https://doi.org/10.1002/app.25413

[22] Verma D, Senal I. Natural fiber-reinforced polymer composites. Elsevier Ltd; 2019. doi:10.1016/b978-0-08-102426-3.00006-0. https://doi.org/10.1016/B978-0-08-102426-3.00006-0

[23] Luzi F, Puglia D, Torre L. Natural fiber biodegradable composites and nanocomposites. Elsevier Ltd; 2019. doi:10.1016/b978-0-08-102426-3.00010-2. https://doi.org/10.1016/B978-0-08-102426-3.00010-2

[24] Huda MS, Drzal LT, Ray D, Mohanty AK, Mishra M. Natural-fiber composites in the automotive sector. Prop Perform Nat Compos 2008:221-68. https://doi.org/10.1533/9781845694593.2.221

[25] Lau K tak, Hung P yan, Zhu MH, Hui D. Properties of natural fibre composites for structural engineering applications. Compos Part B Eng 2018;136:222-33. https://doi.org/10.1016/j.compositesb.2017.10.038

[26] Faruk O, Bledzki AK, Fink HP, Sain M. Biocomposites reinforced with natural fibers: 2000-2010. Prog Polym Sci 2012;37:1552-96. https://doi.org/10.1016/j.progpolymsci.2012.04.003
[27] Balcıoğlu HE. Flexural Behaviors of Sandwich Composites Produced Using Recycled and Natural Material. Mugla J Sci Technol 2018:64-73. https://doi.org/10.22531/muglajsci.421813
[28] Balcıoğlu E, Sakin R. Determination of Mechanical Properties of Natural Sandwich Composites Produced by Using Waste Material. Sak Univ J Sci 2019;23:569-82. https://doi.org/10.16984/saufenbilder.486846
[29] ASTM International. Designation: D 3039/D 3039M - 00 Standard Test Method for Tensile Properties of Polymer Matrix Composite Materials 1 2002;15. doi:10.1520/D3039_D3039M-08. https://doi.org/10.1520/D3039_D3039M-08
[30] ASTM International. Designation: D 3518/D 3518M - 94 Standard Test Method for In-Plane Shear Response of Polymer Matrix Composite Materials by Tensile Test of a ±45° Laminate 2001;5:1-7.
[31] Balcioğlu HE, Aktaş M. An investigation on lateral buckling of laminated composites with delamination. Indian J Eng Mater Sci 2013;20:367-75.
[32] Pozzi A, Sepe R. Mechanical properties of woven natural fiber reinforced composites. Proceeding ECCM-15 Conf Italy 2012:1-11.
[33] Mir A, Aribi C, Bezzazi B. Study of the Green Composite Jute / Epoxy. Int J Mater Metall Eng 2014;8:182-6.
[34] ASTM International. ASTM-D3410 Standard Test Method for Compressive Properties of Polymer Matrix Composite Materials with Unsupported Gage Section by Shear Loading. Annu B ASTM Stand 2003;15.03:1-16.
[35] ASTM. ASTM D256, Determining the Izod Pendulum Impact Resistance of Plastics 2004.
[36] ASTM. D2240 Rubber Property-Durometer Hardness 2015:1-13.

Research on Engineering Structures & Materials
journal homepage: http://jresm.org
MIM Research Group

Research Article

Carbon black reinforced natural rubber/butadiene rubber and natural rubber/butadiene rubber/styrene-butadiene rubber composites: Part I: Rheological, mechanical and thermomechanical properties

Engin Burgaz*[1,2,a], Okan Gencoglu[2,b], Mert Goksuzoglu[2,3,c]

[1]*Department of Metallurgical and Materials Engineering, Ondokuz Mayis University, Samsun TURKEY*
[2]*Department of Nanoscience and Nanotechnology, Ondokuz Mayis University, Samsun TURKEY*
[3]*SAMPA Automotive R&D Center, Tekkekoy, 55300 Samsun, Turkey*

Article Info

Article history:
Received 23 Nov 2018
Revised 12 Mar 2019
Accepted 18 Mar 2019

Keywords:

Natural rubber; Butadiene rubber; Styrene-butadiene rubber; Carbon black reinforced rubber composite; Thermomechanical properties; Rheological properties

Abstract

Carbon black reinforced natural rubber (NR)/butadiene rubber (BR), NR/styrene-butadiene rubber (SBR) and NR/BR/SBR composites were prepared by using two types of BR with highly linear (higher viscosity and molecular weight) and branched chain structures. In NR/BR composite with a higher viscosity BR, the presence of both polysulphidic and monosulphidic types of crosslinking was confirmed based on FT-IR data. NR/BR composite consisting of BR with higher viscosity has the lowest Payne effect and compression set values. NR/BR/SBR composites have much lower Payne effect values compared to NR/SBR system. Also, the addition of BR to NR decreases the tan δ value and leads to lowest values of tan δ in NR/BR composites. Tensile strength and elongation at break values in NR/BR/SBR composites are improved with the addition of BR with a lower viscosity. In comparison with NR/SBR, NR/BR/SBR composites exhibit much less compression set and stress relaxation values because NR/SBR composite exhibits more permanent deformation due to its more rigid styrene content. Here, these results clearly show that blending carbon black reinforced NR or NR/SBR composites with BR having different degrees of viscosity is quite favorable in terms of using these NR composites as anti-vibrational rubber bushings in automotive applications.

1. Introduction

The rheological, mechanical and thermomechanical properties of carbon black filled rubber composites are very important in terms of predicting the service life of final products in automotive industry. Especially, some parts of the framework in trucks cannot be changed easily in periodic maintenance, and it means high maintenance costs. Also, highly improved mechanical and thermomechanical properties of rubber products can provide better driving dynamics, safety and reliability. Many reasons can affect the rheological, mechanical and thermomechanical properties of carbon black filled rubber composites such as the types and amounts of fillers, main polymer, anti-degradation chemicals, other special chemicals and environmental conditions [1-4].

Natural rubber has exceptionally remarkable properties such as outstanding tensile and tear strength and good abrasion resistance which are eligible for production of O-rings, tires, conveyor belts, fluid transfer systems, body sealing systems, transmission systems,

---

*Corresponding author: eburgaz@omu.edu.tr
[a] orcid.org/0000-0002-3953-6131; [b] orcid.org/0000-0002-7168-9461; [c] orcid.org/0000-0002-4590-0905
DOI: http://dx.doi.org/10.17515/resm2019.74ma1123

automotive antivibration, sealants, adhesives & coatings, molded parts, body parts, spare parts, etc [5,6]. The strain-induced crystallization in NR increases mechanical properties especially under high amplitudes of strain. So, this behavior makes the natural rubber a unique elastomer in rubber industry [7-11].

Styrene-butadiene rubber has been used in NR blends since it has better abrasion resistance, crack initiation resistance, high filler-loading capacity and lower heat-build up behavior [5,6,12,13]. SBR is generally used in wear applications. SBR is usually blended with NR to improve its tensile and tear properties [5,6,13]. Thus, SBR has been used in a wide range of products such as side walls of tires, belts, hoses, foot wears, foamed products, etc [5,6]. Mechanical, thermomechanical, and rheological properties of NR/SBR composites have been studied by several researchers [5,6,12,13]. It was previously shown that tensile strength, elastic modulus, elongation at break, hardness and wear resistance of NR/SBR composites increase with increasing NR content and prevulcanization time [5,13].

It is well-known that unfilled or unreinforced rubber has a low modulus, poor abrasion resistance and fatigue behavior [3,4,14]. Carbon blacks (CBs) are generally used to improve the mechanical behavior of rubber. However, this reinforcing method is not adequate by itself especially in the fabrication of heavy industrial rubber products. Rubber composites that have close elastic modulus exhibit similar mechanical properties. BR increases chain flexibility at lower temperatures, filler loading capacity, and decreases heat-build up and energy consumption during mastication [1,3,4]. Thus, blending different types of natural rubber composite with BR is a typical method to improve mechanical properties [3,4,15,16]. It was previously shown that the abrasion resistance, rebound resilience and hardness of natural rubber increases, however its glass transition temperature decreases with the addition of butadiene rubber [15]. Furthermore, better mechanical properties in NR/BR composites were obtained by using carbon blacks that can be well dispersed in the rubber matrix [15]. Recently, the effects of using pyrolytic carbon black (CBp) and pyrolytic oil (Op) which were obtained from used tires on the rheological, mechanical and dynamic mechanical properties of NR/SBR blends were investigated and compared with a control sample that was prepared with N550 and commercial process oil [17]. It was shown that the curing and processing properties in CBp filled NR/SBR blends are similar with those of N550 filled system. In addition, the tensile strength, tear strength and modulus at 100% elongation of the NR/SBR vulcanizates decreased significantly with increasing amount of CBp [17]. Previously, the nanocrystalline cellulose (NCC) was used as a green alternative for carbon black in NR/BR/SBR blends, and the morphology, dynamic viscoelastic behavior, apparent crosslink density, mechanical and dynamic mechanical properties of NR/BR/SBR/NCC blends were discussed in detail [18]. Based on the results, it was shown that NCC was uniformly dispersed in composites and it exhibited comparable reinforcing effect with carbon black. In addition, mechanical tests revealed that the replacement of CB by NCC in NR/BR/SBR blends did not worsen mechanical properties of composites [18].

In addition to a few number of carbon black containing NR/BR composite studies in the literature, recent works in this area have been focused on the use of nano and micron-sized fillers in NR/carbon black and NR/BR/carbon black composites. Among nano-sized filler containing NR/BR/carbon black composite studies in the literature, the use of carbon nanotubes (CNTs) [19,20], halloysite nanotube [21], nanoclay [21,22] and nano zinc oxide [23] in NR/BR/carbon black composite matrix can be given as examples. In addition, micron-sized silica [16,23], and organomodified kaolin [16,24] were used in NR/BR/carbon black composites to enhance the curing characteristics, fatigue resistance, mechanical and dynamic mechanical properties. The mechanical properties of NR/BR and SBR/BR composites were improved with the addition of suitable amounts of ultrafine full-vulcanized styrene-butadiene powdered rubber [25]. Previously, the effect of a partial replacement of CB by silane-treated nanoclays and halloysite nanotubes on the properties of NR/BR blends was investigated [21]. Based on the results, it was concluded that the replacement of a small quantity of CB with silicates or nanotubes results in improved dispersion of the fillers and better dynamic properties due to the decrease of viscosity. However, the mechanical properties of NR/BR blends consisting of either silane treated silicates or halloysite nanotubes exhibited no improvement [21].

Previously, carbon black and carbon nanotube filled NR composites were prepared through an ultrasonic assisted latex mixing process, and their mechanical, rheological and dynamic mechanical properties were compared with NR composites that were prepared with the conventional mixing methods [26]. It was shown that the ultrasonic assisted latex mixing process leads to more homogenously distribution of CNTs in the matrix compared to the conventional mixing methods. Thus, the well dispersed CNTs and CB exhibited a synergistic reinforcing effect such that the elastic modulus at room temperature, storage modulus and complex viscosity increased whereas the maximum loss tangent and shear thinning index decreased with increasing CNT contents [26]. The influence of two types of CB filler N330 and N990 with primary particle sizes of 46 nm and 230 nm, respectively on acrylonitrile-butadiene rubber (NBR) elastomeric composites have been investigated [27]. Based on mechanical, rheological and thermal stability results, it was shown that N330 type carbon black reduces activation energy and increases overall curing rate, crosslinking density more than N990 type CB. N330 CB containing NBR elastomer composites exhibited more thermal stability than those consisting of N990 type CB due to the organic functional groups of carbon black surface which form strong interfacial adhesion forces between CB and the rubber matrix [27]. Previously, NR/BR blends in which the carbon black was replaced partially by multi-walled carbon nanotubes (MWCNTs) was prepared by blending of internal mixer and the two-roll mill [17]. Due to the synergistic effect of CNTs and CB, NR/BR elastomer composites consisting of both MWCNTs and CB exhibited higher values of abrasion resistance, modulus, crosslinking density, tear strength and thermal conductivity compared to those elastomers without any CNTs [17]. Recently, the effects of using 15 pphr sludge palm oil (SPO) as processing oil and various amounts of carbon black from 20 to 50 pphr as the reinforcing filler on the curing characteristics and mechanical properties of NR/SBR elastomeric composites were investigated [28]. The results showed that scorch and cure times, the tensile strength, modulus at 300% strain and tear strength of NR/SBR composites increase with the increasing carbon black loading [28]. Previously, halloysite nanotubes which were surface-modified by plasma polymerization were used as fillers in CB filled NR/BR composites [29]. Based on the results, it was shown that a thiophene modification of HNTs led to improved mechanical properties due to the formation of special type of clusters with carbon black particles and resulted in lower values of Payne effect indicating better filler–polymer interactions [29].

In this paper, carbon black reinforced NR/BR, NR/SBR and NR/BR/SBR composites were prepared by using two types of BR with highly linear (higher molecular weight and viscosity) and branched chain structures. The composition of rubber matrices was varied while the proportions of other components (carbon black and small chemicals) were held constant. The purpose of this work is to investigate and compare the curing behavior, mechanical and thermomechanical properties of NR/BR, NR/SBR and NR/BR/SBR blends. The focus of this work is to show that carbon black reinforced NR/BR and NR/BR/SBR composites containing two types of BR with different chain structures and viscosities display significant property improvements in terms of curing behavior, mechanical and thermomechanical properties compared to carbon black reinforced NR and NR/SBR composites, respectively. Previous studies of carbon black filled NR/BR and NR/BR/SBR composites and NR/BR/carbon black composites consisting of nano and micron-sized fillers have been investigated by several researchers in the literature. However, to the best of our knowledge, no systematic work has been reported about the effect of using two types of BR with different molecular weights and viscosities on the curing behavior, mechanical and thermomechanical properties of carbon black reinforced NR/BR and NR/BR/SBR composites.

2. Experimental

2.1 Materials

Natural rubber that was used in this study is standard Vietnam rubber constant viscosity 60 (SVR CV60) since this grade can maintain its viscosity during and after mastication. For butadiene rubber, cis-Polybutadiene Nd Catalyst was preferred which is widely used in rubber industry. There are two different BR grades in terms of Mooney viscosity in the market which belongs to LANXESS, and they are named as Buna CB 22 (BR1) and CB 24 (BR2). They have 63 and 44 Mooney viscosity, respectively. BR1 has a relatively higher linear chain structure, molecular weight and viscosity compared to BR2. For styrene butadiene rubber, SBR 1502 which has high filler capacity, low heat-build up character and 55±3 Mooney viscosity was used in NR composites. The glass transition temperatures of NR, SBR, butadiene rubber (both BR1 and BR2) are -70, -58 and -92°C, respectively. The composition of NR composites is given in Table 1.

Table 1 The composition of NR composites (BR1: Buna CB22, BR2: Buna CB24)

Sample Composition	NR (phr)	SBR (phr)	BR1 (phr)	BR2 (phr)
NR	100	-	-	-
NR/SBR	50	50	-	-
NR/BR1	50	-	50	-
NR/BR1/SBR	50	30	20	-
NR/BR2	50	-	-	50
NR/BR2/SBR	50	30	-	20

Table 2 The chemical composition of the reference composite (NR)

Constituent	Amount (phr)
SVR CV 60 (NR)	100
Carbon Black N330 (Filler)	50
Zinc Oxide (ZnO)	5
Stearic Acid (StA)	1.5
Aromatic Oil	3
Protective Agents	4
Sulphur (S-80)	3
Total	**166.5**

N330 (High Abrasion Furnace) carbon black was used as a filler material in the same amount in all NR composites. In NR composites, the composition of rubber matrices was varied while the proportions of other components (carbon black and small chemicals) were held constant. The chemical composition of the reference sample NR composite is given in Table 2.

2.2 Fabrication of carbon black filled rubber composites

All samples were mixed in an open laboratory mill that has two rolls. Firstly, carbon black, and then small chemicals were added to the rubber matrix. All samples were mixed in the lab mill at about the same time. During the mastication process, the temperature of rolls was controlled periodically to prevent any uncontrolled temperature increase. Dispersion qualities of NR samples were analyzed with Alpha disperGRADER™ according to ASTM 7723 standard.

Table 3 The dispersion levels and dynamic viscosities of uncured master batches of NR composites

Sample Composition	NR	NR/ SBR	NR/ BR1	NR/BR1/ SBR	NR/ BR2	NR/BR2/ SBR
Mean Agglomerate Size (μm)	10.4	7.8	7.9	8.5	8.8	9.4
n* @ 0.1 Hz (Pa.s)	79980	83752	120385	94211	105812	122660

The dispersion results are given in Table 3. These results show that dispersion levels in all the samples are very close to each other. Master batches were rested for 24 hours after the mastication process. Then, the viscosity of master batches was characterized *via* rheometer at 0.1 Hz under constant strain to verify whether NR composites were over-masticated or not. The rheometer results showed that dynamic viscosities of NR composites are in the range of acceptable tolerances. Afterward, vulcanization agents were added to NR composites. Samples of NR composites were molded by using the compression molding at 180°C within the appropriate cure time. The optimal curing for each NR composite was achieved according to t90 values that were obtained from rheometer results.

2.3 Physical/Chemical Characterization

2.3.1. Attenuated total reflectance Fourier transform infrared (ATR FT-IR) spectroscopy

The Attenuated total reflectance Fourier transform infrared (ATR FT-IR) analysis was performed using a Perkin Elmer branded Spectrum two FT-IR spectrometer, with a germanium crystal having a 9300:1 SNR. The sample surface was scanned in the 4000–600cm^{-1} range, at 45° angle. The ATR-FT-IR spectra were recorded at room temperature. The background subtraction and baseline correction were done.

2.3.2. Rheological analysis

Rheometer tests were performed by using Alpha rubber process analyzer 2000 (RPA) to characterize the curing dynamics of NR composites. Curing parameters such as ts2, t90, G', G'', mL, mH, Payne effect were analyzed as a function of time by RPA at 180°C. The Payne effect values of NR composites were calculated by subtracting G' at angle 25% from G' at angle 1%. Results are given in Table 4. For each RPA test, the sample weight is 8 g.

2.3.3. Hardness

Shore A hardness of rubber samples was measured by using a Bareiss Digitest II type hardness testing machine. The diameter and thickness of the samples are 40 and 6 mm, respectively. Hardness values were recorded after 5 seconds of loading.

2.3.4. Tensile testing

For tensile tests, dumbbell shaped samples of NR composites with 33 mm gauge length were molded by compression molding at 180°C. Tensile tests were performed by using a Zwick 2.5 kN Z2.5/TN1P universal testing machine in accordance with the DIN 53504 standard. The cross head tensile speed was 200 mm/min at room temperature. Five samples were tested for each NR composite, and they were averaged to determine the tensile strength.

2.3.5. Stress relaxation and compression testing

The compression set and stress relaxation in compression tests were analyzed by using Elastocon EB 20 HT and Elastocon EB 17 HT instruments, respectively. The cylindrical sample dimensions for the compression set experiments have a diameter of 12 mm and a thickness of 6.30 mm. The ASTM Standards D395-16 and D6147-97 were used for the compression set and stress relaxation experiments, respectively. All tests were performed at 70°C for 72 hours in Elastocon ovens.

3. Results and Discussion

FT-IR results of NR composites are given in Fig.1(a). The vibration that belongs to the isoprene functional group is located at 840 cm^{-1} [30]. The vibration peaks that are located between 3000-2800 cm^{-1} correspond to asymmetric and symmetric stretchings of C=CH, CH_2, CH_3 groups in NR [30]. The vibration peaks at 1447 and 1377 cm^{-1} correspond to asymmetric deformation vibrations of CH_2 and CH_3 groups in NR [30]. The characteristic in-plane bending of C=C–H is generally observed at 1288 cm^{-1} [30]. However, in Fig.1(a), this peak appears at 1265 cm^{-1} due to different degrees of interactions between isoprene chains and added small chemicals.

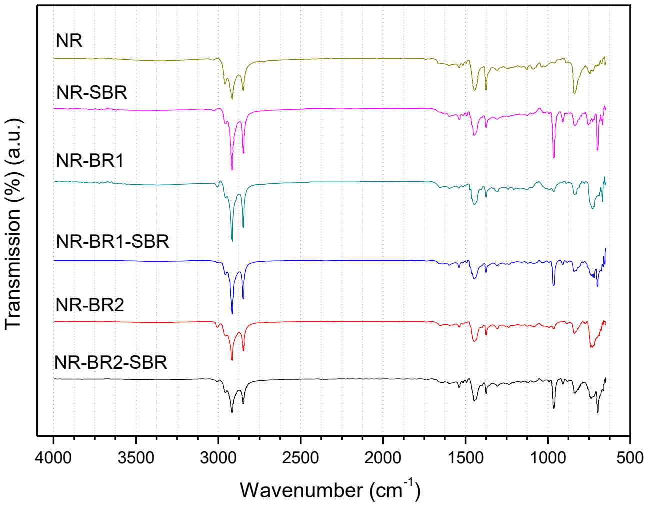

Fig. 1(a) ATR FT-IR of NR, NR/BR, NR/SBR and NR/BR/SBR composites in the region of 4000-600 cm^{-1}

In analogous with NR composite, vibration bands at 3000-2800 cm^{-1} correspond to asymmetric and symmetric stretchings of C=CH, CH_2, CH_3 groups in NR/SBR composite. The vibrations at 1493 and 1451 cm^{-1} correspond to stretchings of carbon atoms in the aromatic ring. Stretching vibrations at 1074 and 1029 cm^{-1} correspond to styrene and *cis*-Polybutadiene units, respectively [31]. The vibration peaks that are located at 759 and 699 cm^{-1} correspond to deformation and out-of-plane bending of CH groups in the aromatic ring, respectively [30]. In NR/BR composites, the characteristics peak at 3024 cm^{-1} corresponds to stretching vibration of the CH_2 groups in butadiene units. The peaks that are located at 1666 and 1400 cm^{-1} are strong proofs for the existence of C=C bonds and deformation vibration of (=CH) units that exist in butadiene units, respectively [30,31].

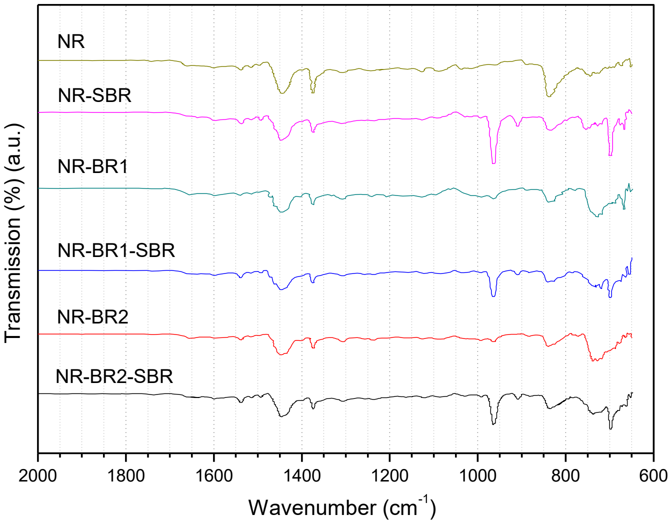

Fig. 1(b) ATR FT-IR of NR, NR/BR, NR/SBR and NR/BR/SBR composites in the region of 2000-600 cm^{-1}

As observed in Fig. 1(b), typical peaks in the range 700-600 cm^{-1} are due to C–S–C, C–S and S–S bonds, respectively. The C–S vibration appears at a frequency higher than S–S vibration since C–S bond stability is higher than S–S [32,33]. Monosulphide linkages occur at higher frequencies that are close to 700 whereas polysulphide vibration bands usually appear around 661 and 600 cm^{-1} [32,33]. In NR-BR1, two vibration bands that are located at 667 and 691 cm^{-1} are associated with polysulphide and monosulphide bonds, respectively. The vibration band at 667 cm^{-1} is much stronger compared to the peak at 691 cm^{-1}. This result confirms that polysulphide type of crosslinking is dominant in NR/BR1. In NR/SBR, in the range 700-600 cm^{-1}, two vibration peaks that are located at 698 and 666 cm^{-1} are clearly visible. Here, the vibration band at 698 cm^{-1} is much stronger compared to the peak at 666 cm^{-1}. This result confirms that monosulphide type of crosslinking is dominant in NR/SBR.

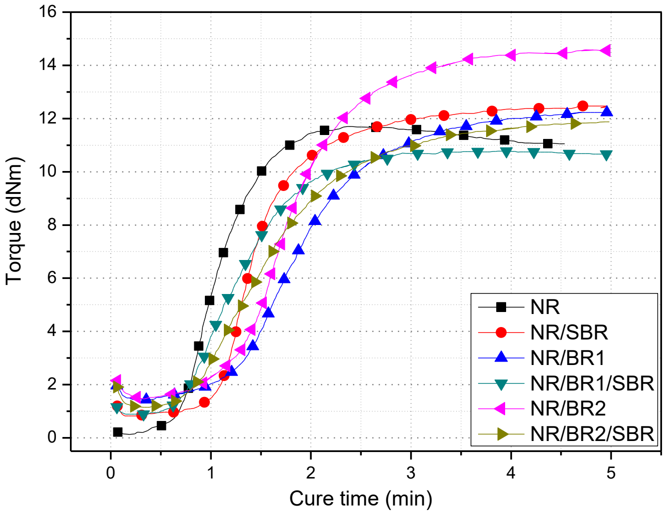

Fig. 2 Cure characteristics of carbon black filled NR, NR/BR, NR/SBR and NR/BR/SBR composites

The rheometer results of NR composites at 180°C are shown in Fig. 2. The cure rates of NR composites were calculated and given in Table 4. In addition, rheometer results of similar NR vulcanizates from literature are also given in Table 5 for comparison.

Table 4 Rheometer results of NR vulcanizates

Sample Composition	NR	NR/ SBR	NR/ BR1	NR/BR1/ SBR	NR/ BR2	NR/BR2/ SBR
ts2 (min)	0.80	1.17	1.42	0.90	1.33	1.04
t90 (min)	1.63	2.32	3.05	2.06	2.76	2.81
mL (dNm)	0.15	0.80	1.43	0.84	1.49	1.17
mH (dNm)	11.67	12.47	12.32	10.75	14.58	11.78
mH-mL (dNm)	11.52	11.67	10.89	9.91	13.09	10.61
Cure Rate (dNm/min)	13.88	10.15	6.68	8.54	9.15	5.99
G’ (kPa) (angle 1%)	1575	1590	1247	1310	1428	1266
G’ (kPa) (angle 25%)	695	892	900	791	980	900
G’ (kPa) (angle 100%)	439	555	596	514	680	617
Payne Effect (kPa)	880	698	347	519	448	366
Tan δ	0.139	0.124	0.082	0.129	0.077	0.155

Table 5 Rheometer results of similar NR vulcanizates from literature

Sample Composition	NR(100phr) (ref15)	NR(50phr)/ SBR(50phr) (ref12)	NR(85phr)/ BR(15phr) (ref15)	NR(70phr)/ SBR(30phr) (ref12)
ts2 (min)	3.23	5.54	3.58	5.05
t90 (min)	9.47	11.40	8.65	10.23
mL (dNm)	2.65	0.65	2.70	0.53
mH (dNm)	15.66	6.72	15.25	6.09
mH-mL (dNm)	13.01	6.07	12.55	5.56
Cure Rate Index (min^{-1})	16.02	17.06	19.72	19.30

Based on rheometer results, the smallest and highest cure rate values were obtained for samples NR/BR2/SBR and NR, respectively. The most optimized cure rate was achieved in NR/BR1/SBR composite. In application, the crosslink density of rubber vulcanizates can be evaluated by help of difference between mH-mL terms. All NR composites have optimal crosslink densities that can be observed from their mH-mL values. The crosslink density increases the fatigue life of rubber composites since it depends on how many polymer chains are linked to each other. Once crosslinking reaction occurs, these chemical links cannot be broken easily. Also, the vulcanization system directly affects the fatigue resistance and compression set since it determines sulfur bridges with mono or poly structures. Monosulphidic bridges (–S–) induce strong and short crosslinking distances but they have no ability to make bonding again when they are broken in contrast to polysulphidic bridges (–S–S–S–) [34]. All rubber composites almost have the same modulus since their G' (angle %25) values are close to each other. In Table 4, NR/BR1 has the lowest Payne effect value since the mean agglomerate size of carbon black in NR/BR1 was measured as one of the lowest in Table 3. This result shows that the addition of BR to NR improves the quality of filler dispersion due to favorable interactions between carbon black and polymer chains. Also, in Table 4, based on the tan δ, the addition of BR to NR decreases the tan δ value. Especially, NR/BR1 and NR/BR2 rubber composite samples have the lowest values of tan δ. So, the addition of BR to carbon black filled NR composite decreases the viscous property and increases the elastic property.

In comparison with NR/SBR composite, NR/BR1/SBR and NR/BR2/SBR composites exhibit much lower S curves in terms of their mH values. In addition, rheometer curves of NR/BR1/SBR and NR/BR2/SBR composites are very similar to each other. In this respect, 20 phr butadiene addition to NR/SBR composite does not improve the curing behavior in these composites. Furthermore, compared to NR/SBR composite, NR/BR1/SBR and NR/BR2/SBR soften or their max torque (mH) values decrease since the total SBR amount decreases with the addition of 20 phr of BR.

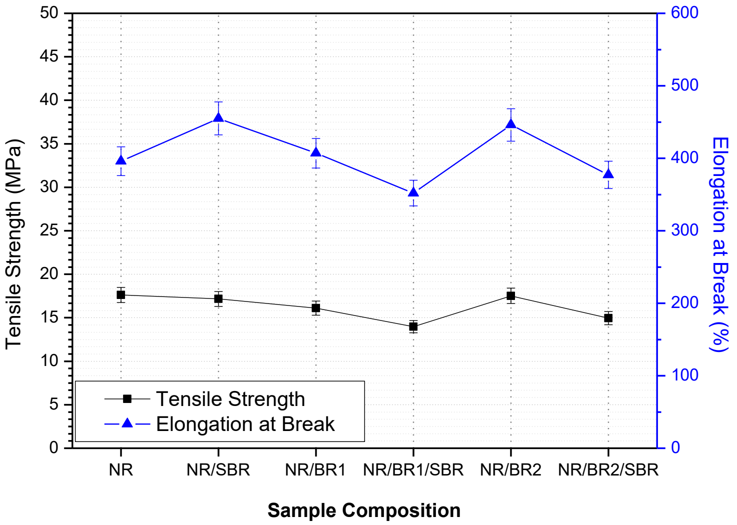

Fig. 3 Tensile testing results of NR, NR/BR, NR/SBR and NR/BR/SBR composites.

The results of tensile tests are given in Fig.3. Here, the tensile strength does not really change, but the elongation at break of pure NR increases with the addition of BR2 which has a highly branched chain structure. This result can be explained such that polymer-filler interactions increase with the well-mixing of carbon black due to the lower viscosity and molecular weight of BR2. Thus, the increase in polymer-filler interactions leads to increase both in terms of tensile strength and elongation at break. In comparison with NR/SBR composite, the tensile strength of NR/BR1/SBR decreases since the phr value of SBR decreases more in this composite. Furthermore, the tensile strength of NR/BR1/SBR is lower than that of NR/SBR because SBR is more rigid than BR1 due to its 23% styrene content. Also, the tensile strength of NR/BR2/SBR composite is lower than that of NR/SBR.

Table 6 Tensile and compression testing results of similar NR vulcanizates from literature

Sample Composition	NR(100phr) (ref35)	NR(50phr)/ SBR(50phr) (ref17)	NR(80phr)/ BR(20phr) (ref29)	NR(60phr)/ SBR(40phr) (ref28)
Tensile strength (MPa)	30	27	20.6	18
Elongation at break(%)	490	325	443	750
Modulus at 100 %(MPa)	3.1	1.68	2.5	-
Modulus at 300 %(MPa)	-	4.62	12.1	5
Compression set (%)	-	31	-	-

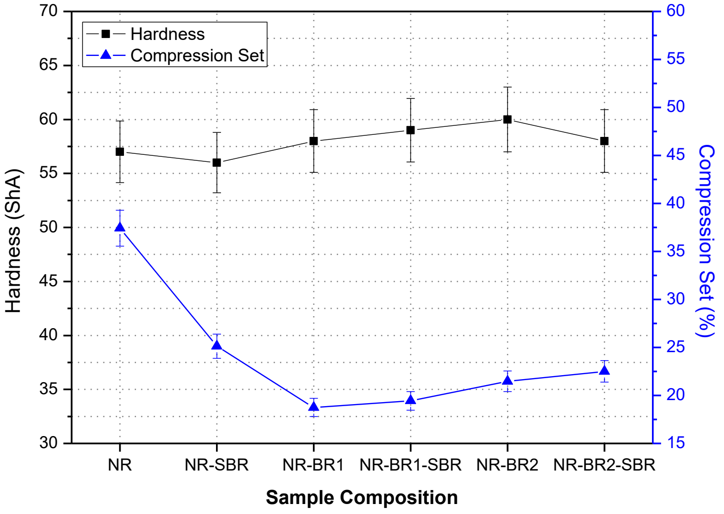

Fig. 4 Compression set and hardness results of NR, NR/BR, NR/SBR and NR/BR/SBR composites.

The results for compression set behavior and hardness measurements are given in Fig. 4. The compression set behavior is also used to determine how elastic a rubber composite behaves under static load. If the chemical bonds are strong enough, compression set results show less permanent deformation. As can be seen from Fig.4, NR/BR1 composite has the lowest compression set behavior. Therefore, based on the compression set data, NR/BR1 composite can be evaluated as the most elastic blend. Hardness values of all NR composites are very similar to each other. Hardness values of all NR composites are very similar to each other. This result mainly shows that changing the composition of NR, BR and SBR in the rubber composites does not affect the hardness values that much. The hardness values of rubber composites is mainly dictated by the amount of carbon black that is used in these samples. In all the samples, carbon black amount is fixed as 50 phr. So, for this reason, it is very logical that the hardness values of rubber composites does not exhibit any big change. The compression set is directly related to Payne effect, viscosity of the polymer and vulcanization system. In comparison with NR/SBR, NR/BR1/SBR and NR/BR2/SBR composites exhibit much less compression set values because NR/SBR composite exhibits more permanent deformation due to its relatively higher rigid styrene content.

Stress relaxation behavior is given in Fig. 5. Stress relaxation is directly related with the elastic characteristics of sulphur bonds which are located between polymer chains [34,36,37]. Single bridges of sulphur (monosulphidic bridges) are known as more elastic and reliable in terms of chemical bonding [34,37]. Monosulphidic bridges propagate relatively more less in comparison with polysulphidic bridges, and this behavior leads to optimal thermomechanical properties (less relaxation in stress and less compression set) [34,37]. In addition, broken monosulphidic bonds have less possibility in terms of bonding again spontaneously in contrast to polysulphidic bonds [34,37]. However, the vulcanization system that was used in the NR/BR1 composite consists of both mono and polysulphidic bonds. So, for this reason, this vulcanization system provides more elasticity and superior thermomechanical properties at the same time.

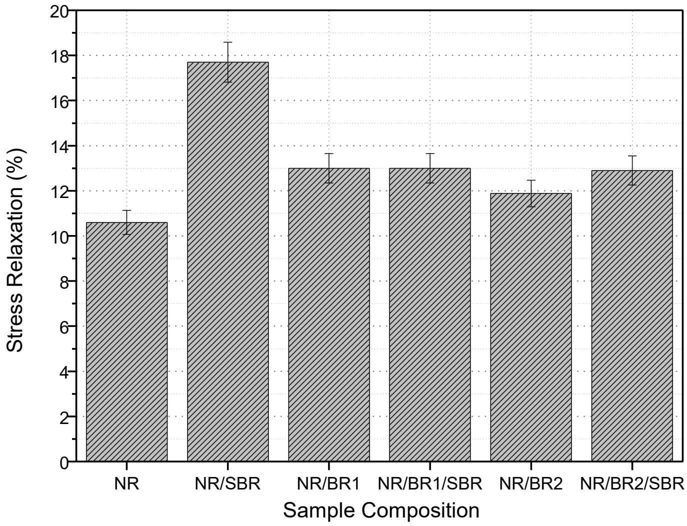

Fig. 5 Stress relaxation results of NR, NR/BR, NR/SBR and NR/BR/SBR composites.

NR/SBR composite displays a much more higher stress relaxation value in comparison with other rubber composites since it experiences a much higher force loss due to its higher rigidity. In comparison with NR/SBR, NR/BR1/SBR and NR/BR2/SBR composites exhibit much lower stress relaxation values. Unlike expectations, in Fig. 5, stress relaxation values of NR/BR1/SBR and NR/BR2/SBR composites are almost equal to each other. It is expected that the ternary blend consisting of BR1 should experience a much more force loss due to its higher viscosity. However, this difference in terms of viscosity does not reflect on the stress relaxation behavior since the vulcanization system has a much more dominant effect on the compression set and stress relaxation at higher temperatures.

4. Conclusion

In summary, carbon black reinforced NR/BR, NR/SBR and NR/BR/SBR composites were prepared by using two types of BR with highly linear (higher viscosity and molecular weight) and branched chain structures. Rheological, mechanical and thermomechanical properties of carbon black filled NR/BR, NR/SBR and NR/BR/SBR composites were systematically compared with each other. Based on rheometer results, the most optimized cure rate was achieved in NR/BR1/SBR composite. NR/BR1 composite has the lowest Payne effect value since the mean agglomerate size of carbon black in NR/BR1 was measured as one of the lowest based on dispersion results. Thus, the addition of BR to NR improves the quality of filler dispersion due to favorable interactions between carbon black and polymer chains. Also, the addition of BR to NR decreases the tan δ value and leads to lowest values of tan δ in NR/BR composites. In comparison with NR/SBR composite, the tensile strength of NR/BR1/SBR decreases since the phr value of SBR decreases more in this composite. Furthermore, the tensile strength of NR/BR1/SBR composite is lower than that of NR/SBR because SBR is more rigid than BR due to its 23% styrene content. Based on the compression set data, NR/BR1 composite has the lowest compression set behavior with an optimal crosslink type and density. In comparison with NR/SBR, NR/BR1/SBR and NR/BR2/SBR composites exhibit much less compression set values because NR/SBR composite exhibits more permanent deformation due to its more rigid styrene content. In comparison with NR/SBR composite, NR/BR1/SBR and NR/BR2/SBR exhibit much lower stress relaxation values. In agreement with compression set values from compression testing data and tan δ values from rheometer data, the elastic character increases and the viscous property decreases in carbon black filled NR/BR composites with the addition of BR. Here, these results clearly show that blending carbon black reinforced NR or NR/SBR composites with BR having different degrees of viscosity is quite favorable in terms of using these NR composites as anti-vibrational rubber bushings in automotive applications.

Acknowledgments

Use of facilities at Ondokuz Mayis University Black Sea Advanced Technology Research and Application Center (KITAM) and SAMPA Automotive R&D Center is acknowledged.

References

[1] Legorju-jago K, Bathias C. Fatigue initiation and propagation in natural and synthetic rubbers. Int J Fatigue. 2002;24:85-92. https://doi.org/10.1016/S0142-1123(01)00062-7

[2] Creton C, Ciccotti M. Fracture and adhesion of soft materials: a review. Rep Prog Phys. 2016;79:046601. https://doi.org/10.1088/0034-4885/79/4/046601

[3] Mars WV, Fatemi A. Factors that affect the fatigue life of rubber: A literature survey. Rubber Chem Technol. 2004;77:391-412. https://doi.org/10.5254/1.3547831

[4] Tee YL, Loo MS, Andriyana A. Recent advances on fatigue of rubber after the literature survey by Mars and Fatemi in 2002 and 2004. Int J Fatigue. 2018;110:115-129. https://doi.org/10.1016/j.ijfatigue.2018.01.007

[5] Findik F, Yilmaz R, Koksal T. Investigation of mechanical and physical properties of several industrial rubbers. Mater Design. 2004;25:269-276. https://doi.org/10.1016/j.matdes.2003.11.003

[6] Tangudom P, Thongsang S, Sombatsompop N. Cure and mechanical properties and abrasive wear behavior of natural rubber, styrene-butadiene rubber and their blends reinforced with silica hybrid fillers. Mater Design. 2014;53:856-864. https://doi.org/10.1016/j.matdes.2013.07.024

[7] Poompradub S, Tosaka M, Kohjiya S, Ikeda Y, Toki S, Sics I, et al. Mechanism of strain-induced crystallization in filled and unfilled natural rubber vulcanizates. J Appl Phys. 2005;97:103529. https://doi.org/10.1063/1.1900927

[8] Toki S, Fujimaki T, Okuyama M. Strain-induced crystallization of natural rubber as detected real-time by wide-angle X-ray diffraction technique. Polymer. 2000;41:5423-5429. https://doi.org/10.1016/S0032-3861(99)00724-7

[9] Huneau B. Strain-Induced Crystallization of Natural Rubber: A Review of X-Ray Diffraction Investigations. Rubber Chem Technol. 2011;84:425-452. https://doi.org/10.5254/1.3601131

[10] Le Cam JB, Toussaint E. The Mechanism of Fatigue Crack Growth in Rubbers under Severe Loading: The Effect of Stress-Induced Crystallization. Macromolecules. 2010;43:4708-4714. https://doi.org/10.1021/ma100042n

[11] Mars WV, Fatemi A. Multiaxial stress effects on fatigue behavior of filled natural rubber. Int J Fatigue. 2006;28:521-529. https://doi.org/10.1016/j.ijfatigue.2005.07.040

[12] George SC, Ninan KN, Groeninickx G, Thomas S. Styrene-butadiene rubber/natural rubber blends: Morphology, transport behavior, and dynamic mechanical and mechanical properties. J Appl Polym Sci. 2000;78:1280-1303. https://doi.org/10.1002/1097-4628(20001107)78:6<1280::AID-APP150>3.0.CO;2-

[13] Varkey JT, Augustine S, Groeninckx G, Bhagawan SS, Rao SS, Thomas S. Morphology and mechanical and viscoelastic properties of natural rubber and styrene butadiene rubber latex blends. J Polym Sci Pol Phys. 2000;38:2189-2211.

https://doi.org/10.1002/1099-0488(20000815)38:16<2189::AID-POLB120>3.0.CO;2-E

[14] Dong B, Zhang LQ, Wu YP. Influences of different dimensional carbon-based nanofillers on fracture and fatigue resistance of natural rubber composites. Polym Test. 2017;63:281-288. https://doi.org/10.1016/j.polymertesting.2017.08.035

[15] Wisojodharmo LA, Fidyaningsih R, Fitriani DA, Arti DK, Indriasari, Susanto H. The influence of natural rubber-butadiene rubber and carbon black type on the mechanical properties of tread compound. IOP Conf Series Mater Sci Eng. 2017;223:012013. https://doi.org/10.1088/1757-899X/223/1/012013

[16] Sreelekshmi RV, Sudha JD, Menon ARR. Novel organomodified kaolin/silica hybrid fillers in natural rubber and its blend with polybutadiene rubber. Polym Bull. 2017;74:783-801. https://doi.org/10.1007/s00289-016-1745-

[17] Karabork F, Tipirdamaz ST. Influence of pyrolytic carbon black and pyrolytic oil madefrom used tires on the curing and (dynamic) mechanical properties of natural rubber (NR)/styrene-butadiene rubber (SBR) blends. eXPRESS Polym Lett. 2016;10:72-82. https://doi.org/10.3144/expresspolymlett.2016.8

[18] Chen WJ, Gu J, Xu SH. Exploring nanocrystalline cellulose as a green alternative ofcarbon black in natural rubber/butadiene rubber/styrene-butadiene rubber blends. eXPRESS Polym Lett. 2014;8:659-668. https://doi.org/10.3144/expresspolymlett.2014.69

[19] Gao J, He Y, Gong X, Xu J. The role of carbon nanotubes in promoting the properties of carbon black-filled natural rubber/butadiene rubber composites. Results in Physics. 2017;7:4352-4358. https://doi.org/10.1016/j.rinp.2017.09.044

[20] Poikelispää M, Das A, Dierkes W, Vuorinen J. The effect of partial replacement of carbon black by carbon nanotubes on the properties of natural rubber/butadiene rubber compound. J Appl Polym Sci. 2013;130:3153-3160. https://doi.org/10.1002/app.39543

[21] Poikelispää M, Das A, Dierkes W, Vuorinen J. The effect of coupling agents on silicate-based nanofillers/carbon black dual filler systems on the properties of a natural rubber/butadiene rubber compound. J Elast Plast. 2015;47:738-752. https://doi.org/10.1177/0095244314538436

[22] Abdollahi M, Khanli HH., Aalaie, J, Yousefi M.R. Structure and properties of natural rubber/butadiene rubber (NR/BR) blend/sodium-montmorillonite nanocomposites prepared via a combined latex/melt intercalation method. Polymer Science Series A. 2011;53:1175-1181. https://doi.org/10.1134/S0965545X11120091

[23] Kim IJ, Kim WS, Lee DH, Kim W, Bae JW. Effect of nano zinc oxide on the cure characteristics and mechanical properties of the silica-filled natural rubber/butadiene rubber compounds. J Appl Polym Sci. 2010;117:1535-1543. https://doi.org/10.1002/app.31996

[24] Raji VV, Ramakrishnan S, Sukumar R, Brahmakumar M, Menon AR. Kaolin modified with sodium salt of rubber seed oil as a reinforcing filler for blends of natural rubber, polybutadiene rubber and acrylonitrile–butadiene rubber. Polymer International. 2015;64:1585-1593. https://doi.org/10.1002/pi.4956

[25] Liu XB, Gao Y, Bian L, Wang Z Influence of ultrafine full-vulcanized styrene-butadiene powdered rubber on dynamic mechanical properties of natural rubber/butadiene rubber and styrene-butadiene rubber/butadiene rubber blends. Polym Bull. 2015;72:2001-2017. https://doi.org/10.1007/s00289-015-1385-5

[26] Zhan YH, Liu GQ, Xia HS, Yan N Natural rubber/carbon black/carbon nanotubes composites prepared through ultrasonic assisted latex mixing process. Plastics, Rubber and Composites. 2011;40:32-39. https://doi.org/10.1179/174328911X12940139029284

[27] Samarzˇija-Jovanovic´ S, Jovanovic´ V, Markovic´ G, Marinovic´-Cincovic M The effect of different types of carbon blacks on the rheological and thermal properties

ofacrylonitrile butadiene rubber J Therm Anal Calorim. 2009;98:275–283. https://doi.org/10.1007/s10973-009-0131-3

[28] Mohamed R, Nurazzi NM, Huzaifah M Effect of carbon black composition with sludge palm oil on the curing characteristic and mechanical properties of natural rubber/styrene butadiene rubber compound IOP Conf. Ser.: Mater. Sci. Eng. 2017; 223:012008.

[29] Poikelispää M, Das A, Dierkes W, Vuorinen J. Synergistic Effect of Plasma-Modified Halloysite Nanotubes and Carbon Black in Natural Rubber—Butadiene Rubber Blend. J Appl Polym Sci. 2013;127:4688-4696. https://doi.org/10.1002/app.38080

[30] Rolere S, Liengprayoon S, Vaysse L, Sainte-Beuve J, Bonfils F. Investigating natural rubber composition with Fourier Transform Infrared (FT-IR) spectroscopy: A rapid and non-destructive method to determine both protein and lipid contents simultaneously. Polym Test. 2015;43:83-93. https://doi.org/10.1016/j.polymertesting.2015.02.011

[31] Munteanu SB, Vasile C. Spectral and thermal characterization of styrene-butadiene copolymers with different architectures. J Optoelectron Adv M. 2005;7:3135-3148.

[32] Mahapatra M, Karmakar M, Mondal B, Singha NR. Role of ZDC/S ratio for pervaporative separation of organic liquids through modified EPDM membranes: Rational mechanistic study of vulcanization. RSC Advances. 2016;6:69387-69403. https://doi.org/10.1039/C6RA10104F

[33] Basak GC, Bandyopadhyay A, Bharadwaj YK, Sabharwal S, Bhowmick AK.. Characterization of EPDM vulcanizates modified with gamma irradiation and trichloroisocyanuric acid and their adhesion behavior with natural rubber. The Journal of Adhesion. 2010;86:306-334. https://doi.org/10.1080/00218460903479305

[34] Joseph AM, George B, Madhusoodanan KN, Alex R. Effect of Devulcanization on Crosslink Density and Crosslink Distribution of Carbon Black Filled Natural Rubber Vulcanizates. Rubber Chem Technol. 2016;89:653-670. https://doi.org/10.5254/rct.16.84819

[35] Rattanasom N, Saowapark T, Deeprasertkul C. Reinforcement of natural rubber with silica/carbon black hybrid filler. Polym Test. 2007;26:369-377. https://doi.org/10.1016/j.polymertesting.2006.12.003

[36] South JT, Case SW, Reifsnider KL. Effects of thermal aging on the mechanical properties of natural rubber. Rubber Chem Technol. 2003;76:785-802. https://doi.org/10.5254/1.3547772

[37] Nasir M, Teh GK The Effects of Various Types of Crosslinks on the Physical-Properties of Natural-Rubber. Eur Polym J. 1988;24:733-736. https://doi.org/10.1016/0014-3057(88)90007-9

Research on Engineering Structures & Materials
journal homepage: http://jresm.org
MIM Research Group

Research Article

Carbon black reinforced natural rubber/butadiene rubber and natural rubber/butadiene rubber/styrene-butadiene rubber composites: Part II. Dynamic mechanical properties and fatigue behavior

Engin Burgaz*[1,2,a], Okan Gencoglu[2,b], Mert Goksuzoglu[2,3,c]

[1]Department of Metallurgical and Materials Engineering, Ondokuz Mayis University, Samsun TURKEY
[2]Department of Nanoscience and Nanotechnology, Ondokuz Mayis University, Samsun TURKEY
[3]SAMPA Automotive R&D Center, Tekkekoy, 55300 Samsun, Turkey

Article Info

Article history:
Received 24 Nov 2018
Revised 14 Mar 2019
Accepted 17 Mar 2019

Keywords:

Natural rubber; Butadiene rubber; Styrene-butadiene rubber; Carbon black reinforced rubber composite; Dynamic mechanical properties; Fatigue strength

Abstract

Carbon black reinforced natural rubber (NR)/butadiene rubber (BR), NR/styrene-butadiene rubber (SBR) and NR/BR/SBR composites were prepared by using two types of BR with highly linear chain structure (higher viscosity and molecular weight) and branched chain structure (lower viscosity and molecular weight). NR/BR composite consisting of BR with higher viscosity has the highest fatigue strength. Damping factors of NR, NR/SBR and NR/BR/SBR composites as a function of frequency were systematically compared at constant temperatures of -40, 0, 25 and 60°C. Based on dynamic mechanical analysis (DMA) results, the elasticity of NR/carbon black composite improves, its heat buildup character and tan δ decreases with the addition of BR. The addition of 20 phr BR to NR/SBR composites provides 4-5 times better fatigue strength due to the decrease of tan δ. Lastly, using a higher viscosity BR in carbon black filled NR or NR/SBR is quite favorable in terms of using these composites as anti-vibrational rubber bushings in automotive applications where high fatigue resistance and lower damping factor are important criteria.

1. Introduction

The dynamic mechanical properties and fatigue behavior of rubber composites have important roles in predicting the service life of final products in automotive industry. Especially, some parts of the framework in trucks cannot be changed easily in periodic maintenance, and it means high maintenance costs. Also, the long fatigue life and better damping properties of rubber products can provide better driving dynamics, safety and reliability. Many reasons can affect dynamic mechanical properties and fatigue life of rubber composites such as the types and amounts of fillers, main polymer, anti-degradation chemicals, other special chemicals and environmental conditions [1-4].

Natural rubber has exceptionally remarkable properties such as outstanding tensile and tear strength and good abrasion resistance which are eligible for production of O-rings, tires, conveyor belts, fluid transfer systems, body sealing systems, transmission systems, automotive antivibration, sealants, adhesives & coatings, molded parts, body parts, spare

---

*Corresponding author: eburgaz@omu.edu.tr
[a] orcid.org/0000-0002-3953-6131; [b] orcid.org/0000-0002-7168-9461; [c] orcid.org/0000-0002-4590-0905
DOI: http://dx.doi.org/10.17515/resm2109.75ma1124

parts etc. [5,6]. NR has a great strength in terms of fatigue behavior when it is compared with other rubbers. The strain-induced crystallization in NR increases mechanical properties especially under high amplitudes of strain. In addition, this property provides a longer fatigue life to NR in comparison with other rubbers. So, this behavior makes the natural rubber a unique elastomer in rubber industry [7-11]. The mechanism of fatigue behavior such as the nucleation and growth of defects or cracks in NR has been investigated by several researchers [1-4,10-19]. Mars *et al.* investigated the multiaxial stress effects on fatigue crack nucleation and growth in filled NR systems. The initial and additional softenings in the system were believed to be conclusions of irreversible breakage of various bonds and network chain breakage by the effect of fillers, respectively [11]. The cavitation as a result of decohesion between zinc oxides and rubber matrix was found out to be the crucial fatigue damage, and the crack tip consists of stretched elliptical regions that are surrounded by highly stretched and crystallized ligaments [13]. The cracks initiate from rigid inclusions such as SiO_2 or $CaCO_3$ particles, and large carbon black agglomerates with an average size of 200 μm that are present in natural rubber. In addition, the crack orientation is dependent on the type and maximum level of loading [14].

Styrene-butadiene rubber has been used in NR blends since it has better abrasion resistance, crack initiation resistance, high filler-loading capacity and lower heat-build up behavior [5,6,20,21]. SBR is generally used in wear applications. SBR is usually blended with NR in order to improve its tensile and tear properties [5,6,21]. Thus, SBR has been used in a wide range of products such as side walls of tires, belts, hoses, foot wears, foamed products, etc. [5,6]. Mechanical, thermomechanical, fatigue and rheological properties of NR/SBR composites have been studied by several researchers [5,6,20,21]. Based on dynamic mechanical and mechanical results of NR/SBR composites, it was revealed that the storage modulus decreases and loss modulus and tan δ increase with increasing temperature and NR concentration [20]. Based on DMA results, it was previously shown that SBR/NR blends are incompatible due to their two distinct glass-transition temperatures [20,21].

It is well-known that unfilled or unreinforced rubber has a low modulus, poor abrasion resistance and fatigue behavior [3,4,22]. Carbon blacks are generally used to improve the mechanical behavior of rubber. However, this reinforcing method is not sufficient by itself especially in the fabrication of heavy industrial rubber products. Rubber composites that have close elastic modulus exhibit similar mechanical properties. But in terms of fatigue behavior and service life, changes in the types of polymers lead to quite different fatigue resistance [3,4]. A longer fatigue life can be achieved in rubber composites by using butadiene rubber in the matrix [3,4,23]. BR increases chain flexibility at lower temperatures, filler loading capacity, and decreases heat-build up and energy consumption during mastication [1,3,4,24]. Thus, blending different types of natural rubber composite with BR is a typical method to improve the fatigue life [3,4,23,24]. It was previously shown that the abrasion resistance, rebound resilience and hardness of natural rubber increases, however its glass transition temperature decreases with the addition of butadiene rubber [23]. Furthermore, better mechanical properties in NR/BR composites were obtained by using carbon blacks that can be well dispersed in the rubber matrix [23]. In addition to a few number of carbon black containing NR/BR composite studies in the literature, recent works in this area have been focused on the use of nano and micron-sized fillers in NR/BR/carbon black composites.

Among nano-sized filler containing NR/BR/carbon black composite studies in the literature, the use of carbon nanotubes [25,26], halloysite nanotube [27], nanoclay [27,28] and nano zinc oxide [29] in NR/BR/carbon black composite matrix can be given as examples. In addition, micron-sized silica [24,29], and organomodified kaolin [24,30] were used in NR/BR/carbon black composites to enhance the curing characteristics, fatigue resistance, mechanical and dynamic mechanical properties.

The dynamic mechanical properties of NR/BR and SBR/BR composites were improved with the addition of suitable amounts of ultrafine full-vulcanized styrene-butadiene powdered rubber [31]. Tension and compression tests of SBR/BR/NR composites revealed that changes in frequency, strain rate and load do not significantly influence the fatigue life. However, if the values of frequency and maxiumum strain are higher, the values of sample temperature and thermal load are higher due to the hysteresis of rubber composites [16].

In this paper, carbon black reinforced NR/BR, NR/SBR and NR/BR/SBR composites were prepared by using two types of BR with highly linear chain structure (higher molecular weight and viscosity) and branched chain structure (lower viscosity and molecular weight). The composition of rubber matrices was varied while the proportions of other components (carbon black and small chemicals) were held constant. The purpose of this work is to investigate and compare dynamic mechanical properties and fatigue life of carbon black filled NR/BR, NR/SBR and NR/BR/SBR composites. The focus of this work is to show that carbon black reinforced NR/BR and NR/BR/SBR composites containing two types of BR with different chain structures, viscosities and molecular weights display significant property improvements in terms of fatigue life and dynamic mechanical properties compared to carbon black reinforced NR and NR/SBR composites, respectively. Previous studies of carbon black filled NR/BR and NR/BR/SBR composites and NR/BR/carbon black composites consisting of nano and micron-sized fillers have been investigated by several researchers in the literature. However, to the best of our knowledge, no systematic work has been reported about the effect of using two types of BR with different molecular weights and viscosities on the fatigue life and dynamic mechanical properties of carbon black reinforced NR/BR and NR/BR/SBR composites.

2. Experimental

2.1 Materials

Natural rubber that was used in this study is standard Vietnam rubber constant viscosity 60 (SVR CV60) since this grade can maintain its viscosity during and after mastication. For butadiene rubber, cis-Polybutadiene Nd Catalyst was preferred which is widely used in rubber industry. There are two different BR grades in terms of Mooney viscosity in the market which belongs to LANXESS, and they are named as Buna CB 22 (BR1) and CB 24 (BR2). They have 63 and 44 Mooney viscosity, respectively. BR1 has a relatively higher linear chain structure, molecular weight and viscosity compared to BR2. For styrene butadiene rubber, SBR 1502 which has high filler capacity, low heat-build up character and 55±3 Mooney viscosity was used in NR composites. The glass transition temperatures of NR, SBR, butadiene rubber (both BR1 and BR2) are -70°C, -58°C and -92°C, respectively. The composition of NR composites is given in Table 1.

N330 (High Abrasion Furnace) carbon black was used as a filler material in the same amount in all NR composites. In NR composites, the composition of rubber matrices was varied while the proportions of other components (carbon black and small chemicals) were held constant. The chemical composition of the reference sample NR composite is given in Table 2.

Table 1 The composition of NR composites (BR1: Buna CB22, BR2: Buna CB24)

Sample Composition	NR (phr)	SBR (phr)	BR1 (phr)	BR2 (phr)
NR	100	-	-	-
NR/SBR	50	50	-	-
NR/BR1	50	-	50	-
NR/BR1/SBR	50	30	20	-
NR/BR2	50	-	-	50
NR/BR2/SBR	50	30	-	20

Table 2 The chemical composition of the reference composite (NR)

Constituent	Amount (phr)
SVR CV 60 (NR)	100
Carbon Black N330 (Filler)	50
Zinc Oxide (ZnO)	5
Stearic Acid (StA)	1.5
Aromatic Oil	3
Protective Agents	4
Sulphur (S-80)	3
Total	166.5

2.2 Fabrication of carbon black filled rubber composites

All samples were mixed in an open laboratory mill that has two rolls. The masterbatch, sulphur powder and final batch are shown in Fig.1. Firstly, carbon black, and then small chemicals were added to the rubber matrix. All samples were mixed in the lab mill at about the same time. During the mastication process, the temperature of rolls was controlled periodically to prevent any uncontrolled temperature increase. The final batch before and during mixing with sulphur powder and accelerators on a two-roll mill are shown in Figs. 2(a) and (b), respectively.

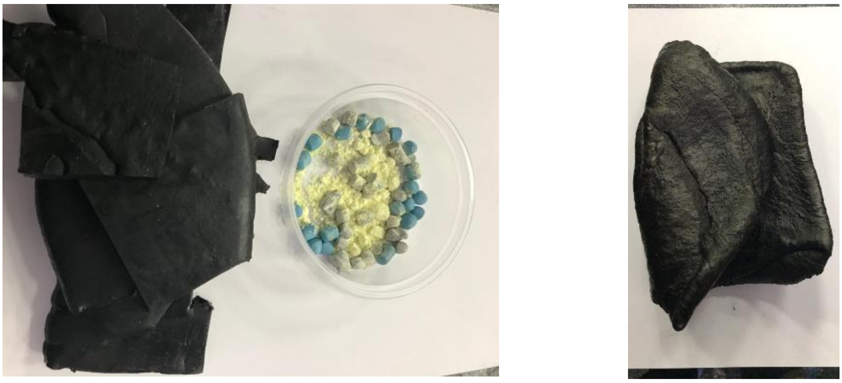

(a)

(b)

Fig. 1(a) The masterbatch, sulphur powder and accelerators (b) The final batch

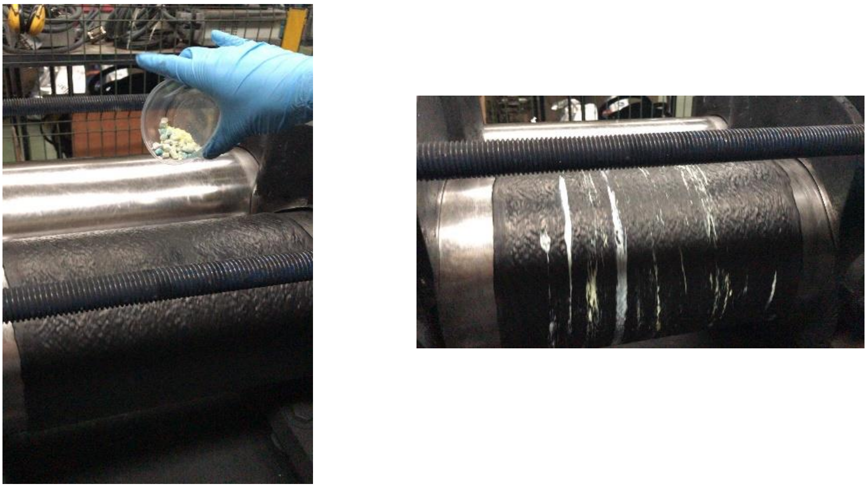
(a) (b)

Fig. 2(a) The final batch before mixing with sulphur powder and accelerators on a two-roll mill and (b) the final batch during mixing with with sulphur powder and accelerators on a two-roll mill

2.3 Physical/Chemical Characterization

2.3.1. Dynamic mechanical analysis (DMA)

The damping behavior of NR composites was analyzed by using a MetraVib +1000 dynamic mechanical analysis (DMA) instrument. DMA tests of cylindrical NR vulcanizates were carried out by using the compression mode with frequency sweep from 1 Hz to 200 Hz at constant temperature. The temperatures were chosen as −40°C, 0°C, 25°C and 60°C. Cold temperatures were achieved by pumping liquid nitrogen to the sample compartment from liquid nitrogen tank that is attached to the DMA instrument. Also, hot temperatures were obtained by using the heater inside DMA. The DMA compression mode samples which were prepared from the compression set mold have a diameter of 12 mm and a thickness of 6.30 mm. There is no specific standard for sample dimensions in the compression mode of DMA. All the samples have the same dimensions to obtain good consistent data. In addition, the experimental procedure for the DMA compression tests were also executed in the same manner for all the samples. For each sample, three repetitions were made to obtain consistent data. The parameters such as storage and loss moduli and tan δ were automatically obtained or calculated by the software that is running the DMA instrument.

2.3.2. Fatigue analysis

The fatigue behavior of NR composites was determined by using Alpha Fatigue to Failure Tester (FTFT) with only one constant 1.78 extension ratio, 1.67 Hz and tensile load according to ASTM D4482. All the samples were subjected to same experimental conditions. In FTFT experiment, 1.78 extension ratio corresponds to % 78 strain value in a typical static stress-strain experiment. And this value is about %322 lower compared to the maximum elongation of NR sample in this study. For each sample, maximum strain was %78 and minimum strain was %0 during each cycle. For each NR vulcanizate, six samples were tested and averaged to determine the fatigue behavior. In the FTFT test, the criteria of fatigue damage is defined as complete rupture of test specimen according to ASTM D4482. So, the number of cycles to failure (fatigue life) was recorded up to the complete material breakage for each sample. The dumbbell shaped specimens have a gauge length of 25 mm, a thickness of 2 mm and a width of 4 mm. The pictures of a fatigue sample and FTFT are given in Fig.3.

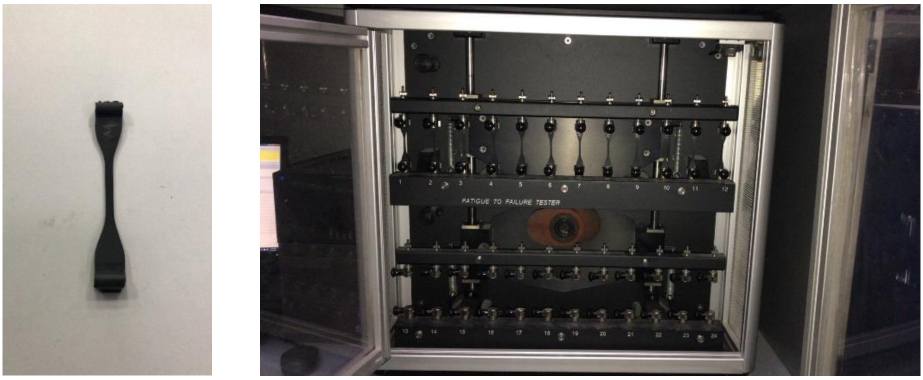

(a) (b)

Fig. 3(a) The FTFT test sample and (b) the Alpha Fatigue to Failure Tester (FTFT)

2.3.3. Scanning electron microscopy (SEM)

SEM experiments were performed by using a JEOL JSM 7001F. The SE detector, HV mode, 15.00 and 10.00 kV accelerating voltages were used during the experiments. Samples were coated with 5-6 nm Au-Pd to induce electrical conductivity. The SEM images were taken from sample surfaces which were fractured after the samples were subjected to static stress-strain tests. NR sample was ruptured at a tensile stress of 18 MPa and a maximum elongation of % 400. In addition, NR/BR1 sample was ruptured at a tensile stress of 16 MPa and a maximum elongation of % 410.

3. Results and Discussion

DMA results of NR composites at -40°C, 0°C, 25°C and 60°C are given in Figs.4-7, respectively. At all temperatures, the elasticity of NR matrix improves since carbon black particles are relatively well-dispersed with the addition of butadiene rubber. Thus, tan δ decreases, and the heat buildup character or loss modulus of NR/BR composite system also diminishes. As can be seen from Figs.4-7, the butadiene rubber gives more chain flexibility to the composite especially at lower temperatures due to the highly linear chain structure and relatively lower T_g of BR.

In Fig.4, at -40°C, NR/SBR has the highest tan δ since it is the most rigid composite because of its 23% styrene content. In Fig.4, at -40°C, NR/BR2 composite exhibits a higher tan δ compared to NR/BR1 since the storage modulus of NR/BR1 composite is relatively much higher compared to NR/BR2 due to the higher viscosity of BR1. Also, in agreement with previous Payne effect and dispergrader results [32], the loss modulus of NR/BR2 composite is much higher compared to that of NR/BR1 since filler-filler interactions are much higher in NR/BR2 compared to NR/BR1 composite. In Fig.4, NR/BR1/SBR composite displays a higher tan δ compared to NR/BR2/SBR since filler-filler interactions increase due to the higher viscosity of BR1. The increase of filler-filler interactions in NR/BR1/SBR composite compared to NR/BR2/SBR is also confirmed by Payne effect results from our previous work [32]. Thus, this behavior leads to higher loss modulus and tan δ in NR/BR1/SBR in comparison with that of NR/BR2/SBR composite.

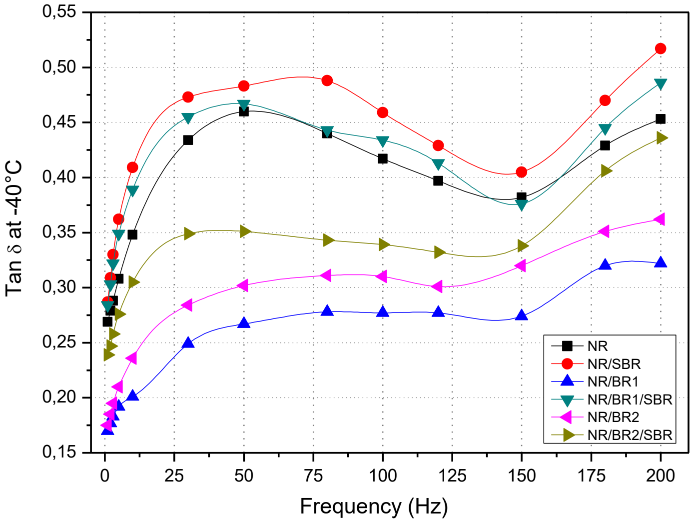

Fig. 4. DMA results of NR, NR/BR, NR/SBR and NR/BR/SBR composites at -40°C.

In Fig.5, at 0°C, due to the increase of temperature, tan δ of NR/SBR decreases slightly at all frequencies compared to that at -40°C, and its profile almost becomes equal to that of NR composite. As the temperature increases from -40°C to 0°C, tan δ of NR/BR2 decreases more than that of NR/BR1, and tan δ profiles of NR/BR1 and NR/BR2 almost become equal at all frequencies. In Fig.5, NR/BR1/SBR composite displays a higher tan δ compared to NR/BR2/SBR since filler-filler interactions increase due to the higher viscosity of BR1.

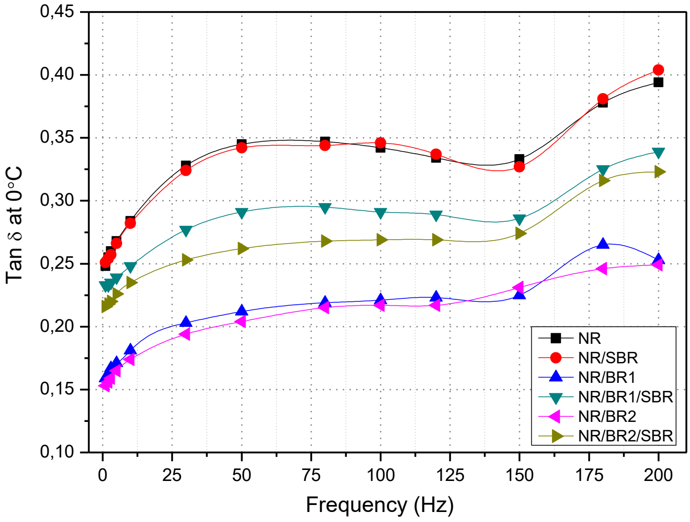

Fig. 5. DMA results of NR, NR/BR, NR/SBR and NR/BR/SBR composites at 0°C.

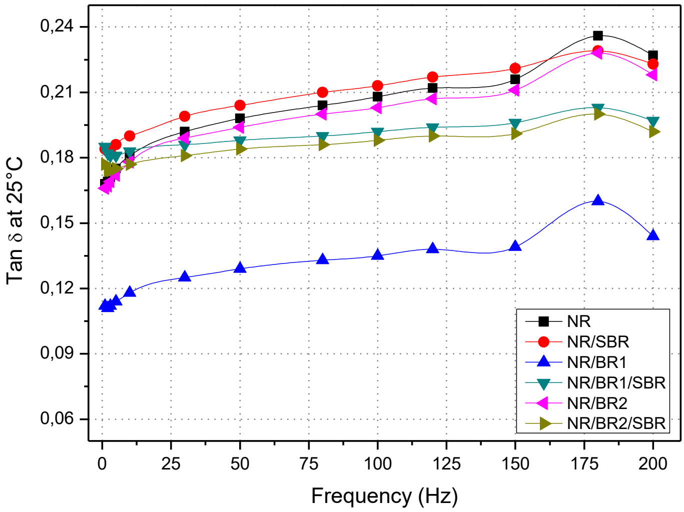

Fig. 6. DMA results of NR, NR/BR, NR/SBR and NR/BR/SBR composites at 25°C.

In Fig.6, at 25°C, due to the increase of temperature from 0 to 25°C, tan δ profiles of NR/SBR and NR decrease slightly at all frequencies compared to those at 0°C, and their tan δ values profiles are almost equal to each other. As the temperature increases from 0°C to 25°C, tan δ of NR/BR1 decreases more than that of NR/BR2, and tan δ profile of NR/BR2 becomes much higher than that of NR/BR1 at 25°C. At this temperature, storage and loss modulus values of both NR/BR1 and NR/BR2 decrease compared to the case at 0°C. But, the decrease in storage modulus in NR/BR2 is more pronounced compared to NR/BR1 due to the higher viscosity of BR1. Thus, the storage modulus of NR/BR1 is much higher and its tan δ is much lower compared to NR/BR2 at all frequencies. In Fig.6, at 25°C, NR/BR1/SBR composite displays a higher tan δ compared to NR/BR2/SBR since filler-filler interactions increase due to the higher viscosity of BR1. The increase of filler-filler interactions in NR/BR1/SBR composite compared to NR/BR2/SBR is also confirmed by Payne effect results from our previous work [32]. Thus, this behavior leads to higher loss modulus and tan δ in NR/BR1/SBR in comparison with that of NR/BR2/SBR composite.

In Fig.7, at 60°C, tan δ of NR/SBR composite is much lower compared to NR due to the higher T_g and high filler loading capacity of SBR. As the temperature increases from 25°C to 60°C, tan δ of NR/BR2 decreases more than that of NR/BR1, and tan δ profile of NR/BR1 becomes much higher than that of NR/BR2 at 60°C. In Fig.7, at 60°C, NR/BR1/SBR composite displays a higher tan δ compared to NR/BR2/SBR since filler-filler interactions increase due to the higher viscosity of BR1. As the temperature increases from 25°C to 60°C, tan δ of NR/BR2/SBR decreases, and tan δ profile of NR/BR2/SBR becomes much lower than that of NR/BR1/SBR. Storage and loss modulus values of NR/BR2/SBR decrease compared to the case at 25°C. But, the decrease of loss modulus in NR/BR2/SBR is more pronounced than the decrease of storage modulus. In the case of NR/BR1/SBR composite, as the temperature increases from 25°C to 60°C, tan δ of NR/BR1/SBR does not change that much at all frequencies.

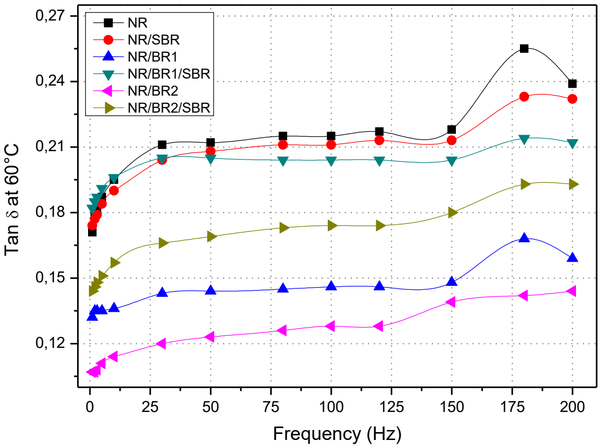

Fig. 7. DMA results of NR, NR/BR, NR/SBR and NR/BR/SBR composites at 60°C.

Fatigue results are given in Fig. 8. As can be seen from FTFT results, the most durable composite is NR/BR1, and it has 1.5 million of cycles in terms of fatigue failure. This is because the presence of BR component which has a higher linear chain structure, molecular weight and viscosity improves elasticity and storage modulus. Fatigue behavior is directly related with the elastic characteristics of sulphur bonds which are located between polymer chains [33-35]. Single bridges of sulphur (monosulphidic bridges) are known as more elastic and reliable in terms of chemical bonding [33,35]. Monosulphidic bridges propagate relatively more less in comparison with polysulphidic bridges, and this behavior leads to optimal thermomechanical properties (less relaxation in stress and less compression set) but lower fatigue resistance [33,35]. In addition, broken monosulphidic bonds have less possibility in terms of bonding again spontaneously in contrast to polysulphidic bonds [33,35]. However, the vulcanization system that was used in the NR/BR1 composite consists of both mono and polysulphidic bonds. So, for this reason, this vulcanization system provides more elasticity, superior thermomechanical properties [32] and higher fatigue resistance at the same time.

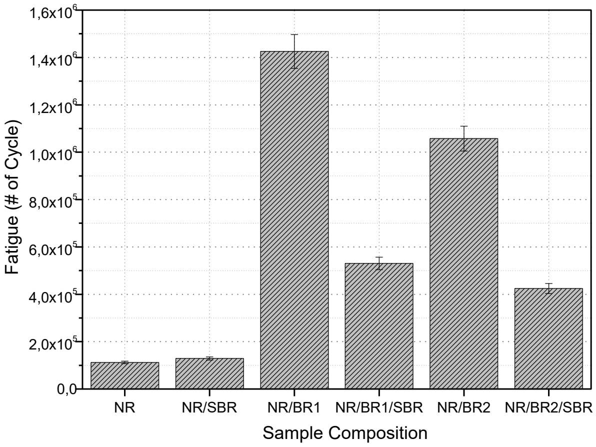

Fig. 8. Fatigue results of NR, NR/BR, NR/SBR and NR/BR/SBR composites.

Fatigue behavior deteriorates with increasing tan δ of NR composites. For instance, in comparison with NR/BR1, the fatigue resistance of NR/BR1/SBR composite is much lower due to the addition of 30 phr addition of SBR instead of BR1. In comparison with NR/SBR composite, fatigue strengths of NR/BR1/SBR and NR/BR2/SBR composites exhibit higher values. Here, the composition of NR/SBR composite is 50/50 phr. Thus, compared to NR/SBR, in NR/BR/SBR composites, taking out 20 phr SBR and adding 20 phr BR provide 4-5 times better fatigue strength values due to the decrease of tan δ.

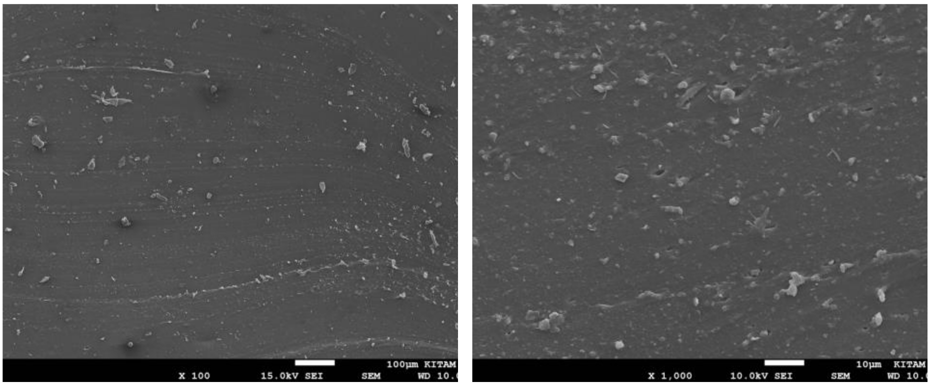

Fig. 9. SEM micrographs of NR composite.

SEM images of fracture surfaces that belong to carbon black reinforced NR and NR/BR1 composites are shown in Figures 9 and 10, respectively. In Fig.9, it is clearly seen that carbon black reinforced NR composite that does not contain any BR component has a relatively sharp and brittle fracture surface. In NR composite, filler-filler interactions were observed to be higher due to the absence of BR based on damping, fatigue and previously observed Payne effect results [32].

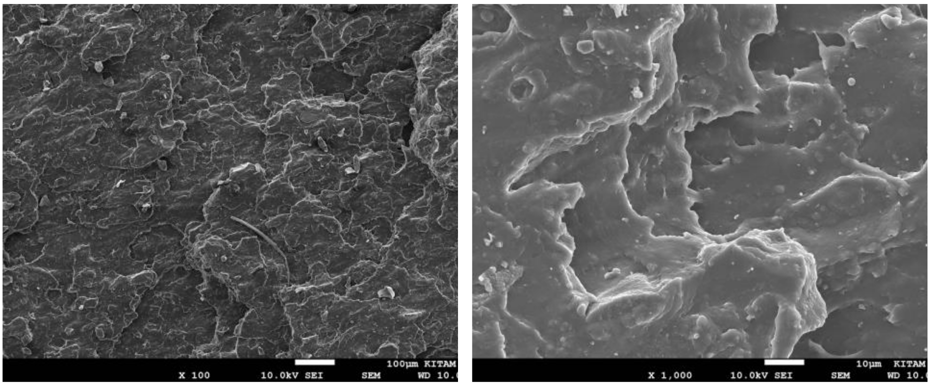

Fig. 10. SEM micrographs of NR/BR1 composite

In Fig.10, in NR/BR1 composite, since BR gives more elasticity to NR blends, the fracture process appears more ductile, and the crack propagation becomes more difficult compared to NR composite. Thus, for this reason, the fatigue life of NR/BR1 is much higher compared to NR composite since a crack needs more energy to propagate in a softer matrix with a higher ductile property.

4. Conclusion

In summary, carbon black reinforced NR/BR, NR/SBR and NR/BR/SBR composites were prepared by using two types of BR with highly linear chain structure (higher viscosity and molecular weight) and branched chain structure (lower viscosity and molecular weight). Dynamic mechanical properties and fatigue life of carbon black filled NR/BR, NR/SBR and NR/BR/SBR composites were systematically compared with each other. Based on DMA results, at all temperatures, the elasticity of NR matrix improves since carbon black particles are relatively well-dispersed with the addition of butadiene rubber. Thus, tan δ decreases, and the heat buildup character of NR/BR composite system also diminishes. Especially at lower temperatures, the butadiene rubber gives more chain flexibility to the rubber composite due to the linear chain structure and relatively lower T_g of BR. In addition, at all temperatures, NR/BR1/SBR composite displays a higher tan δ compared to NR/BR2/SBR since filler-filler interactions increase due to the higher viscosity of BR1 compared to BR2. Fatigue results clearly show that the most durable composite is NR/BR1, and it has 1.5 million of cycles in terms of fatigue failure. This is because the presence of BR component with a higher molecular weight and viscosity in NR improves elasticity and storage modulus. Fatigue behavior deteriorates with increasing tan δ of blends. For instance, in comparison with NR/BR1 composite, the fatigue resistance of NR/BR1/SBR is much lower due to the addition of 30 phr addition of SBR instead of BR1. The addition of 20 phr BR to NR/SBR/carbon black composites provide 4-5 times better fatigue strength due to the decrease of tan δ. SEM results also confirm fatigue results such that NR/carbon black composite has a relatively sharp and brittle fracture surface in comparison with NR/BR1/carbon black composite. Since BR gives more elasticity to NR/BR1 composite, the fracture process appears more ductile, and the crack propagation becomes more difficult than pure NR composite. Here, these results clearly show that blending carbon black reinforced NR or NR/SBR composites with BR which has different degrees of viscosity is quite favorable in terms of using these NR composites as anti-vibrational rubber bushings in automotive applications where high fatigue resistance and lower damping factor are important criteria.

Acknowledgments

Use of facilities at Ondokuz Mayis University Black Sea Advanced Technology Research and Application Center (KITAM) and SAMPA Automotive R&D Center is acknowledged.

References

[1] Legorju-jago K, Bathias C. Fatigue initiation and propagation in natural and synthetic rubbers. Int J Fatigue. 2002;24:85-92. https://doi.org/10.1016/S0142-1123(01)00062-7

[2] Creton C, Ciccotti M. Fracture and adhesion of soft materials: a review. Rep Prog Phys. 2016;79:046601. https://doi.org/10.1088/0034-4885/79/4/046601

[3] Mars WV, Fatemi A. Factors that affect the fatigue life of rubber: A literature survey. Rubber Chem Technol. 2004;77:391-412. https://doi.org/10.5254/1.354783

[4] Tee YL, Loo MS, Andriyana A. Recent advances on fatigue of rubber after the literature survey by Mars and Fatemi in 2002 and 2004. Int J Fatigue. 2018;110:115-129. https://doi.org/10.1016/j.ijfatigue.2018.01.00

[5] Findik F, Yilmaz R, Koksal T. Investigation of mechanical and physical properties of several industrial rubbers. Mater Design. 2004;25:269-276. https://doi.org/10.1016/j.matdes.2003.11.00

[6] Tangudom P, Thongsang S, Sombatsompop N. Cure and mechanical properties and abrasive wear behavior of natural rubber, styrene-butadiene rubber and their blends

reinforced with silica hybrid fillers. Mater Design. 2014;53:856-864. https://doi.org/10.1016/j.matdes.2013.07.024

[7] Poompradub S, Tosaka M, Kohjiya S, Ikeda Y, Toki S, Sics I, et al. Mechanism of strain-induced crystallization in filled and unfilled natural rubber vulcanizates. J Appl Phys. 2005;97:103529. https://doi.org/10.1063/1.1900927

[8] Toki S, Fujimaki T, Okuyama M. Strain-induced crystallization of natural rubber as detected real-time by wide-angle X-ray diffraction technique. Polymer. 2000;41:5423-5429. https://doi.org/10.1016/S0032-3861(99)00724-7

[9] Huneau B. Strain-Induced Crystallization of Natural Rubber: A Review of X-Ray Diffraction Investigations. Rubber Chem Technol. 2011;84:425-452.

[10] Le Cam JB, Toussaint E. The Mechanism of Fatigue Crack Growth in Rubbers under Severe Loading: The Effect of Stress-Induced Crystallization. Macromolecules. 2010;43:4708-4714. https://doi.org/10.1021/ma100042n

[11] Mars WV, Fatemi A. Multiaxial stress effects on fatigue behavior of filled natural rubber. Int J Fatigue. 2006;28:521-529. https://doi.org/10.1016/j.ijfatigue.2005.07.040

[12] Mars WV, Fatemi A. Fatigue crack nucleation and growth in filled natural rubber. Fatigue Fract Eng M. 2003;26:779-789. https://doi.org/10.1046/j.1460-2695.2003.00678.x

[13] Le Cam JB, Huneau B, Verron E, Gornet L. Mechanism of fatigue crack growth in carbon black filled natural rubber. Macromolecules. 2004;37:5011-5017. https://doi.org/10.1021/ma0495386

[14] Saintier N, Cailletaud G, Piques R. Crack initiation and propagation under multiaxial fatigue in a natural rubber. Int J Fatigue. 2006;28:61-72. https://doi.org/10.1016/j.ijfatigue.2005.03.006

[15] Beurrot S, Huneau B, Verron E. In Situ SEM Study of Fatigue Crack Growth Mechanism in Carbon Black-Filled Natural Rubber. J Appl Polym Sci. 2010;117:1260-1269.

[16] Seichter S, Archodoulaki VM, Koch T, Holzner A, Wondracek A. Investigation of different influences on the fatigue behaviour of industrial rubbers. Polym Test. 2017;59:99-106. https://doi.org/10.1016/j.polymertesting.2017.01.018

[17] Saintier N, Cailletaud G, Piques R. Multiaxial fatigue life prediction for a natural rubber. Int J Fatigue. 2006;28:530-539. https://doi.org/10.1016/j.ijfatigue.2005.05.011

[18] Marco Y, Huneau B, Masquelier I, Le Saux V, Charrier P. Prediction of fatigue properties of natural rubber based on the descriptions of the cracks population and of the dissipated energy. Polym Test. 2017;59:67-74. https://doi.org/10.1016/j.polymertesting.2017.01.015

[19] Mars WV, Fatemi A A literature survey on fatigue analysis approaches for rubber. Int J Fatigue. 2002;24:949-961. https://doi.org/10.1016/S0142-1123(02)00008-

[20] George SC, Ninan KN, Groeninickx G, Thomas S. Styrene-butadiene rubber/natural rubber blends: Morphology, transport behavior, and dynamic mechanical and mechanical properties. J Appl Polym Sci. 2000;78:1280-1303. https://doi.org/10.1002/1097-4628(20001107)78:6<1280::AID-APP150>3.0.CO;2-S

[21] Varkey JT, Augustine S, Groeninckx G, Bhagawan SS, Rao SS, Thomas S. Morphology and mechanical and viscoelastic properties of natural rubber and styrene butadiene rubber latex blends. J Polym Sci Pol Phys. 2000;38:2189-2211. https://doi.org/10.1002/1099-0488(20000815)38:16<2189::AID-POLB120>3.0.CO;2-E

[22] Dong B, Zhang LQ, Wu YP. Influences of different dimensional carbon-based nanofillers on fracture and fatigue resistance of natural rubber composites. Polym Test. 2017;63:281-288. https://doi.org/10.1016/j.polymertesting.2017.08.035

[23] Wisojodharmo LA, Fidyaningsih R, Fitriani DA, Arti DK, Indriasari SH. The influence of natural rubber-butadiene rubber and carbon black type on the mechanical properties

of tread compound. IOP Conf Series Mater Sci Eng. 2017;223:012013. https://doi.org/10.1088/1757-899X/223/1/012013

[24] Sreelekshmi RV, Sudha JD, Menon ARR. Novel organomodified kaolin/silica hybrid fillers in natural rubber and its blend with polybutadiene rubber. Polym Bull. 2017;74:783-801. https://doi.org/10.1007/s00289-016-1745-9

[25] Gao J, He Y, Gong X, Xu J. The role of carbon nanotubes in promoting the properties of carbon black-filled natural rubber/butadiene rubber composites. Results in Physics. 2017;7:4352-4358. https://doi.org/10.1016/j.rinp.2017.09.044

[26] Poikelispää M, Das A, Dierkes W, Vuorinen J. The effect of partial replacement of carbon black by carbon nanotubes on the properties of natural rubber/butadiene rubber compound. J Appl Polym Sci. 2013;130:3153-3160. https://doi.org/10.1002/app.39543

[27] Poikelispää M, Das A, Dierkes W, Vuorinen J. The effect of coupling agents on silicate-based nanofillers/carbon black dual filler systems on the properties of a natural rubber/butadiene rubber compound. J Elast Plast. 2015;47:738-752. https://doi.org/10.1177/0095244314538436

[28] Abdollahi M, Khanli HH., Aalaie, J, Yousefi M.R. Structure and properties of natural rubber/butadiene rubber (NR/BR) blend/sodium-montmorillonite nanocomposites prepared via a combined latex/melt intercalation method. Polymer Science Series A. 2011;53:1175-1181. https://doi.org/10.1134/S0965545X11120091

[29] Kim IJ, Kim WS, Lee DH, Kim W, Bae JW. Effect of nano zinc oxide on the cure characteristics and mechanical properties of the silica-filled natural rubber/butadiene rubber compounds. J Appl Polym Sci. 2010;117:1535-1543. https://doi.org/10.1002/app.31996

[30] Raji VV, Ramakrishnan S, Sukumar R, Brahmakumar M, Menon AR. Kaolin modified with sodium salt of rubber seed oil as a reinforcing filler for blends of natural rubber, polybutadiene rubber and acrylonitrile–butadiene rubber. Polymer International. 2015;64:1585-1593. https://doi.org/10.1002/pi.4956

[31] Liu XB, Gao Y, Bian L, Wang Z Influence of ultrafine full-vulcanized styrene-butadiene powdered rubber on dynamic mechanical properties of natural rubber/butadiene rubber and styrene-butadiene rubber/butadiene rubber blends. Polym Bull. 2015;72:2001-2017. https://doi.org/10.1007/s00289-015-1385-5

[32] Burgaz E, Gencoglu O, Goksuzoglu M. Rheological, mechanical and thermomechanical properties of carbon black reinforced natural rubber/butadiene rubber and natural rubber/butadiene rubber/styrene-butadiene rubber composites. Submitted to Research on Engineering Structures and Materials (RESM).

[33] Joseph AM, George B, Madhusoodanan KN, Alex R. Effect of Devulcanization on Crosslink Density and Crosslink Distribution of Carbon Black Filled Natural Rubber Vulcanizates. Rubber Chem Technol. 2016;89:653-670. https://doi.org/10.5254/rct.16.84819

[34] South JT, Case SW, Reifsnider KL. Effects of thermal aging on the mechanical properties of natural rubber. Rubber Chem Technol. 2003;76:785-802. https://doi.org/10.5254/1.3547772

[35] Nasir M, Teh GK The Effects of Various Types of Crosslinks on the Physical-Properties of Natural-Rubber. Eur Polym J. 1988;24:733-736. https://doi.org/10.1016/0014-3057(88)90007-9

Research on Engineering Structures & Materials
journal homepage: http://jresm.org
Research Group

Research Article

Evaluation of the effect of boron waste sludge and clay on the diffusion of plasticizer to different environments from PVC composite films

A. Pınar Tüzüm Demir *[a]

Department of Chemical Engineering, Usak University, Faculty of Engineering, Turkey

Article Info

Article history:
Received 24 Jan 2019
Revised 17 Apr 2019
Accepted 22 Apr 2019

Keywords:

PVC;
Plasticizer;
Diffusion;
Boron;
Clay;
Oxidation index

Abstract

Poly (vinyl chloride) (PVC) is a rigid polymer that can also be used in flexible applications by the addition of plasticizers. When plasticized PVC (p-PVC) film is heated, plasticizer evaporates from the surface of the film and it degrades by the loss of hydrogen chloride (HCl) gas. Plasticizers are not chemically bound to the polymers, easily diffuse to the contact media during its life-time and contaminate the environments which are in contact. The aim of this study is to reduce the diffusion of plasticizer by means of boron waste sludge (BWS) and clay filler (CF, kaolinite) to assess the effects of BWS and CF on the diffusion of plasticizer.
Plastisols were prepared by mixing of plasticizer, heat stabilizer, BWS and CF into PVC resin and were cured in plastigel films. Thus obtained plastigel films were subjected to heat treatment in an oven at 100, 130 and 150°C. During heat treatment diffusion of plasticizers from p-PVC films into air was studied. In addition, migration of plasticizers into hexane was compared with the migration of plasticizers into air during the heat treatment. For this purpose, the effects of BWS and CF on the migration of the plasticizer to different environments were examined. Diffusion coefficient of plasticizer was evaluated according to the Fick's law and to determine related activation energies according to the Arrhenius relation. Oxidation index (OI) values were determined by using FTIR spectroscopy. The addition of boron waste was reduced the diffusion of the plasticizer into air and increased the activation energy value. Its determined that, the mass loss of the films decreased with increasing amount of BWS and CF

1. Introduction

Among the polymers PVC has a wide application area, due to its high versatility and low production costs and excellent properties [1-4]. However, oxygen, UV radiation, temperature and humidity in the atmosphere are the main factors causing the polymer to age [5]. Additives are added to PVC to achieve the desired material properties [6].

In order to decrease the processing temperature and to obtain desirable properties such as processability, flexibility or extensibility, plasticizer needs to be added into PVC [7, 8]. Among these commercial plasticizers, phthalate esters especially bis(2-ethylhexyl) phthalate (DEHP) known as di-octyl phthalate, (DOP, as well) play an important role owing to their excellent performance, its unique properties [2, 4, 7, 9]. Nowadays, phthalates based plasticizers are criticized. Because they are not chemically bonded to polymers and allowing them to easily migrated from materials and diffuse to the surrounding media, resulting in adverse effects of human exposure through inhalation, ingestion, and skin contact as a potential carcinogenic agents and detrimental environmental problems [1, 2,

---

*Corresponding author: pinar.demir@usak.edu.tr
[a] orcid.org/0000-0002-0822-5728
DOI: http://dx.doi.org/10.17515/resm2019.94ma0124

8]. Among the group of new general purpose plasticizers are also terephthalates, especially dioctyl terephthalate (DOTP), also known as di- (2-ethylhexyl) terephthalate (DEHTP), has the same molecular weight as DEHP. However, the linear structure of DOTP provides better compatibility with PVC, resulting in low migration than that of DEHP [1]. In addition, DOTP has no carcinogenic, genotoxic or developmental effects [1, 10]. There are several studies in literature about migration of plastic products from PVC products to the environments where they are in contact. Royaux et al. 2018, investigated the degradation kinetics of ancient and model plasticized PVC films containing phthalate to emphasize the role of contact material in aging of plasticized PVC. They reported that silk paper reduces the migration of plasticizers and PVC degradation rate and had a protective effect during the storage of PVC objects [11]. Münch et al. 2018, reported that phospholipids used as anti-coagulation increased the migration of plasticizers from PVC tubing into blood [12].

Plastisols are prepared by mixing plasticizer, heat stabilizer and other additives in PVC resin and then heated up to 180-200oC to obtain plastigel forms [1, 13]. When a plasticized PVC (p-PVC) film is heated, plasticizer evaporates from the surface of the film and PVC degrades by the loss of hydrogen chloride (HCl) gas (dehydrochlorination). PVC could be stabilized with heat stabilizers to prevent dehydrochlorination. Hydrotalcite (HT) is a non-toxic, environmentally friendly compound and is a layered double hydroxide (LDH) inorganic complex having HCl absorption capacity to be used as PVC thermal stabilizers [14, 15]. Boron is rarely found in nature. It can be combined with oxygen and other elements, called borates. [16]. Borates and their products are important issues of industrial development in the world. However, their wastes are the most abundant inorganic waste in Turkey that has 67% of the world's boron reserves are in Turkey. Therefore, the evaluation of such wastes is very important [17, 18].

In literature, Alva et al., 2018, reported that the composite with boron nitride showed the best improvement in thermal conductivity of polyvinyl butyral [19]. Fang et al, 2013, investigated the thermal decomposition and fire retardancy of wood-flour (WF) and zinc borate (ZB)–polyvinyl chloride composites. The results showed that the addition of WF and ZB significantly influenced the thermal degradation behavior of PVC and PVC composite [20]. Cui et al., 2015, reported the effect of boron nitride with graphene nanosheets on the improvement of thermal properties of polymeric composites [21]. However, in the literature, there is no study examining the effect of boron waste sludge to reduce the migration of plasticizers from flexible PVC products.

Kaoline is one of the abundant minerals found naturally in the earth's crust and has a layered silicate structure (LDH) [22]. It is widely used to production of polymeric composites [23]. Kaolin refers to a family of kaolinitic clays that consist of a 1:1-type clay mineral with one tetrahedral sheet and one octahedral sheet, depending on the geological and weathering conditions [23]. It is used in the ceramic industry, paper, plastics, paints, production of portland cement as filler [22]. The recent increase in research on polymer-clay composites is due to the fact that they offer more fire, mechanical and thermal properties than polymer composites containing conventional fillers [24]. Kaolin has smaller spacings of layers compared to montmorillonite, due to strong internal hydrogen bonds between layers. PVC-LDH composite has better thermal stability than PVC because the hydroxides can absorb the HCl as it is evolved [24].

Two main processes are considered in the migration of plasticizers. The first is the diffusion through the polymer matrix to the surface of the material and the second is to the surrounding environment through the polymer boundary. Both processes should be considered when analyzing the migration rate [25]. The migration rate is determined by the diffusion coefficient. The activation energy is the kinetic component of the temperature dependence of permeation and is mainly determined by penetrant size and shape of a polymer. Generally, it can be defined as the energy required to separate the polymer chains for a diffusional splash [26]. Diffusion coefficient of the plasticizers can be calculated from the corresponding mass loss data when the other evaporating or decomposing components are negligible [1].

The process of diffusion of additives to the surface from the bulk of polymer is described by Fick's law of diffusion. Crank has shown that, the solution of Fick's law for the layer geometry is as given in Eq. (1) [25].

$$\frac{M_t}{M_\infty} = (4/l) \times (D\ t/\pi)^{0.5} \qquad (1)$$

Where; D is the diffusion coefficient, Mt and M∞ are the mass of diffusing substance from a distance of l at time t, and, at equilibrium of sorption attained theoretically after infinite time, respectively. Hence; D can be calculated from the slope of initial portion of Mt /M∞ versus square root of time plots.

Activation energy of plasticizers for diffusion is expected to be inversely proportional to the diffusivity values. Diffusion coefficient can be expressed in the Arrhenius form in Eq. (2)

$$D_e = D_o \times e^{\frac{-E_A}{RT}} \qquad (2)$$

Where; De is the effective diffusion coefficient (m^2s^{-1}), D_o is a constant defined as preexponential factor which is the theoritically maximum diffusion coefficient at infinitely high temperature, E_A ($Jmol^{-1}$) is the activation energy for diffusion, R is the universal gas constant and T is the temperature studied. The activation energy values can be calculated from the slope of Arrhenius plots of the present data as ln D_e versus T^{-1}. The universal gas constant R is taken as 8.314 $Jmol^{-1}K^{-1}$.

IR spectroscopy is useful for the characterization of additives in polymer. It is also a useful tool to monitor polymer degradation. Plasticizer migration, oxidative degradation during processing and oven aging are determined using IR spectroscopy. During the degradation oxygen diffuses into the polymer, reacts with free radicals inside and causes more oxidation. This process results in thickening of the oxidized surface layer and higher Oxidation Index (OI) as the degradation increases [1]. Absorption bands appeared in the IR spectra at around 1720 cm^{-1}, can be attributed to carbonyl (C=O) groups between two methylene groups (-CH2COCH2-). The formation of oxidative substances are associated with α and β chloro carboxylic acids (1716 cm^{-1}) and α and β chloroketones (1730–1770 cm^{-1}) [27]. OI is calculated considering the absorbance of carbonyl band and the absorbance of a reference group of -CH2- at 1363 cm^{-1}, 1420 cm^{-1} or 2920 cm^{-1} band [1] as shown in Eq. (3).

$$OI = \frac{A_{C=0}}{A_{ref}} = \frac{A_{[1722.cm^{-1}]}}{A_{[2920.cm^{-1}]}} x100 \qquad (3)$$

The present study compares the effect of a BWS and CF additives on the diffusivity of the plasticizers migrated to different contact media (air and hexane) from the p-PVC films. The plastisols were prepared mixing of plasticizer (di-octyl tere ftalat) (DOTP), secondary stabilizer (epoxidized soy bean oil) (ESBO), heat stabilizer (hydrotalcite) (HT), BWS and CF into 100 parts of PVC resin. Films in 150 µm thickness on glass plates were cured for 15 minutes at 160°C. The p-PVC films were subjected to heat treatment to follow the mass loss to find out diffusivity of and to determine activation energies.

2. Materials and Methods

2.1. Materials

A typical commercial emulsion PVC resin (paste type, <63µm, K# 71-75; Mw 97300-110643 gmol^{-1}, Petkim Co, Turkey), was used throughout the study. Dioctyl terephthalate (DOTP) is used as plasticizer, while epoxidized soy bean oil (ESBO) and hydrotalcite (HT) are used as heat stabilizers, BWS and kaolinitic type clay mineral (CF) are used as auxilary materials as filler.

The plasticizer (DOTP; ≥99.5 % purity, CAS: 117-81-7) and the heat stabilizers (epoxidized soybean oil (ESBO) and HT (SC-491880) were supplied by the producer, Sigma Aldrich. Boron waste sludge was supplied by ETİ Maden, Turkey. CF with about 46% SiO_2 content having average particle diameter of 6 µm was provided from Uşak shelves, Turkey.

2.1. Methods

2.1.1 Plastisol Preparation

The plastisols were prepared mixing with 60 phr (per hundred resin) of DOTP, 5 phr of ESBO and 3 phr of HT, 0, 1, 3 phr of BWS and 0, 1, 3 phr of CF into PVC resin, on the mass basis. A homogeneous mixture was obtained mixing dried PVC resin with firstly solid and then liquid ingredients by using a steel mixer (8011 EB, SS 610).

2.2.2. Preparation of Plastigel Films

Plastisols were applied on a glass plate as 150µ thick films with the help of a four sided film applicator (Sheen Ins., UK; 1107/60/2). The films after curing (gelling to produce plastigel) for 15 minutes in oven at 160°C were cooled down to room temperature and stripped off the glass plates. The codes of p-PVC films and their filler contents were given in Table 1.

Table 1 The codes of p-PVC films and their filler contents

Film Codes	**Filler, phr**	
	BWS	**CF**
B0C0	-	-
B1	1	-
B3	3	-
C1	-	1
C3	-	3

2.2.3 Kinetic Study of Plasticizer Diffusion in Air

The films were cut into small pieces about 10x20mm and placed in the oven set at 100, 130 and 150°C. The films were weighed from the beginning up to 420 minutes during the heat treatment at certain time intervals, by using a digital balance (Denver Instrument; SI:234, max:230 g, d:0,1 mg).

2.2.4. Kinetic Study of Plasticizer Diffusion in Hexane

The films cut into small pieces about 10x20mm were put in hexane. The films were weighed from the beginning up to 420 minutes at certain time intervals during the immersion in hexane.

2.2.5. Spectroscopic study on p-PVC films

FTIR spectroscopy was used as a complementary technique to follow of functional groups and to determine the oxidation after degradation.

Fourier transform infrared (FTIR) spectra of untreated, heat treated and hexane treated films were obtained on a Perkin Elmer (Spectra 100) FTIR spectrometer, at a resolution of 4 cm^{-1}. The FTIR spectra were recorded in transmittance units within the 4000–400-cm^{-1} range. The intensity of the carbonyl bands (1500–2000 cm^{-1}) was used to estimate degradation.

3. Results and Discussion

3.1 Determination of Mass Loss

The nature and amount of the plasticizer, heat stabilizer and other additives, surrounding media, environmental conditions effect the migration of plasticizer [1, 26, 28]. When the plasticized PVC film is exposed to heat treatment, mass loss occurs by evaporating the plasticizer from the surface. The mass loss of p-PVC films into air containing BWS and CF during the heat treatment at 100, 130 and 150^{o}C are given in Figure 1 (a), (b) and (c) respectively.

Since the stabilizers used herein have very high molar mass (603.973 g/mole and 975.5 g/mole for HT and ESBO, respectively), they hardly evaporate and their contributions at the applied temperature to mass loss is considered negligible [20].

The mass loss of the films increased with temperature and thermal processing time. While the mass loss for B0C0, B1, B3, C1, C3 having films at 420 minutes at 100^{o}C are 0.1, 0.7, 0.6, 0.21, 0.16 x 10^{-2} %, those at 150^{o}C are 0.87, 0.46, 0.24, 0.85, 0.46 x10^{-2} % respectively.

BWS and CF (filler)-free film showed the highest mass loss compared to other films whereas the films having boron waste sludge were lower mass loss. In general, the mass loss of the films decreased with increasing amount of boron.

The mass loss of p-PVC films containing BWS and CF into hexane at ambient temperature are given in Figure 2. The mass loss in CF films exposed to the hexane medium was higher than that of BWS films.

In the filler free film, the mass loss after hexane immersion was about 220-times higher than in the 100^{o}C heat treatment, which was approximately 25-times higher than in the 150^{o}C heat treatment. In the film containing 1 part of boron, the mass loss observed in the hexane medium was observed to be about 110 and 22 times higher than that of 100 and 150^{o}C heat treatment, respectively. However, in the film containing 1 part of CF, the mass loss observed in the hexane medium was observed to be about 240 and 67 times higher than that of 100 and 150^{o}C heat treatment, respectively.

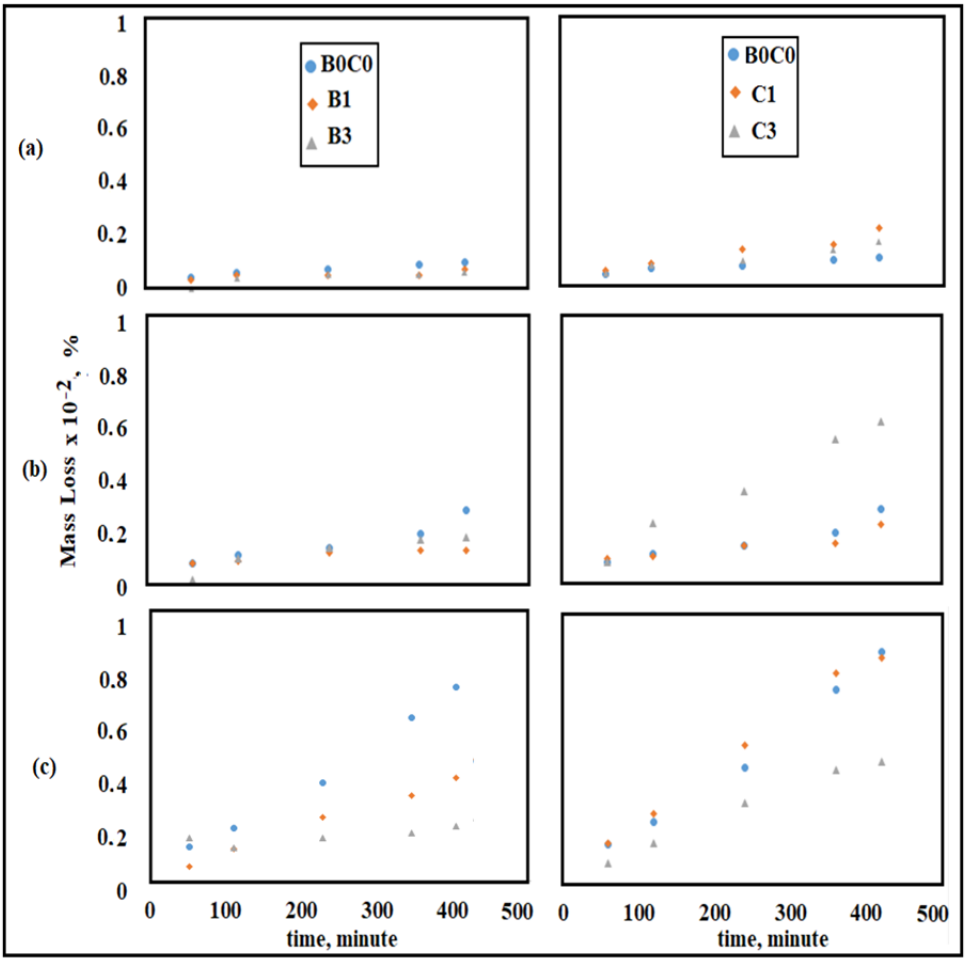

Fig. 1 Mass loss of p-PVC films containing BWS and CF after heat treatment in air at (a) 100ºC (b) 130ºC (c) 150ºC

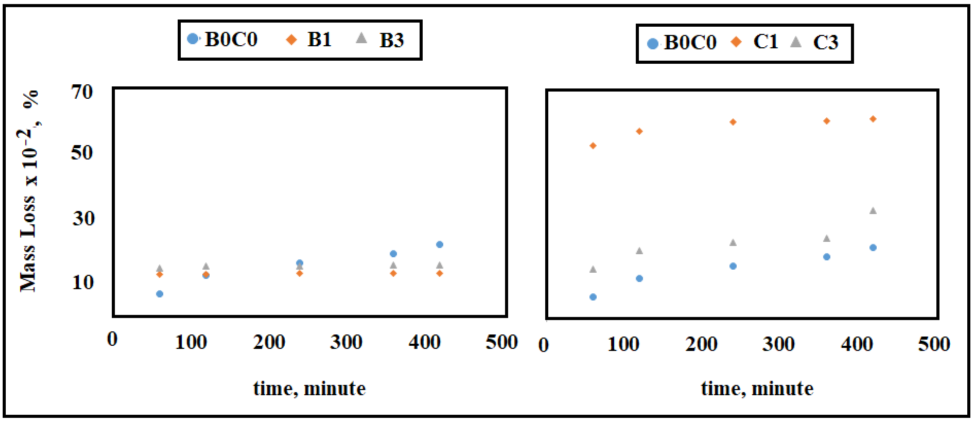

Fig. 2 Mass loss of p-PVC films in the course of hexane immersion

Since BWS addition reduces plasticizer migration out of such plastic objects to the environment in which it contacts, BSW utiliziation in such an application has two way benefit: Decreasing environmental contamination in terms of plasticizer migration and piles of BSW.

3.2 Calculation of Diffusion Coefficient for Determination of Plasticizer Migration

Diffusion coefficient of the migrating molecule out of a polymer film was estimated from the slope of the linear portion of the graph of fractional loss versus $t^{0.5}$ by using Eq. (1). The data as the mass loss of the films during the heat treatment were evaluated to calculate fractional loss (M_t/M_∞). The M_∞ is the mass at equilibrium, which is considered herein as the maximum amount of evaporable plasticizer and corresponds in this study to 0.357 g plasticizer/g film, for filler free film. The linearity of M_t/M_∞ versus $t^{0.5}$ plots in the region of $M_t/M_\infty < 0.5$ confirms that the model is valid (Figure 3). Fractional mass losses of BWS and CF films into hexane are given in Figure 4.

The plots revealed a good fit to the Fickian diffusion kinetics which is confirmed by the correlation coefficient for diffusion, R^2, as reported in Table 2 together with the diffusion coefficients, D, for the migration of plasticizers out of p-PVC films into air and hexane. The diffusion coefficients of films increased with temperature as expected. The addition of boron waste sludge has reduced the diffusion of the plasticizer from the films into air.

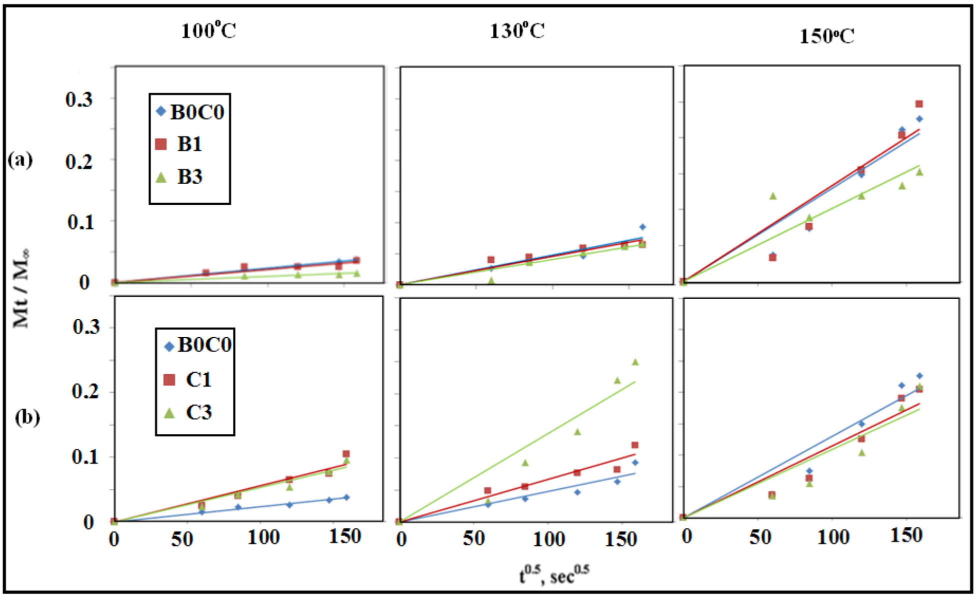

Fig. 3 Uptake ratio of p-PVC films during heat treatment in air for films containing (a) BWS (b) CF

In our previous study [1], the diffusion coefficient of DOTP from films into air was found to be be 7.1 x 10^{-15} m^2/sec at 160°C heat treatment. In this study, for boron waste sludge and CF free film, this value was found to be so close as 7.5 x 10^{-15} m^2/sec into air at 150°C heat treatment. This value was decreased approximately 41% by 3 phr boron waste sludge addition. The addition of boron waste sludge is more effective than that of CF.

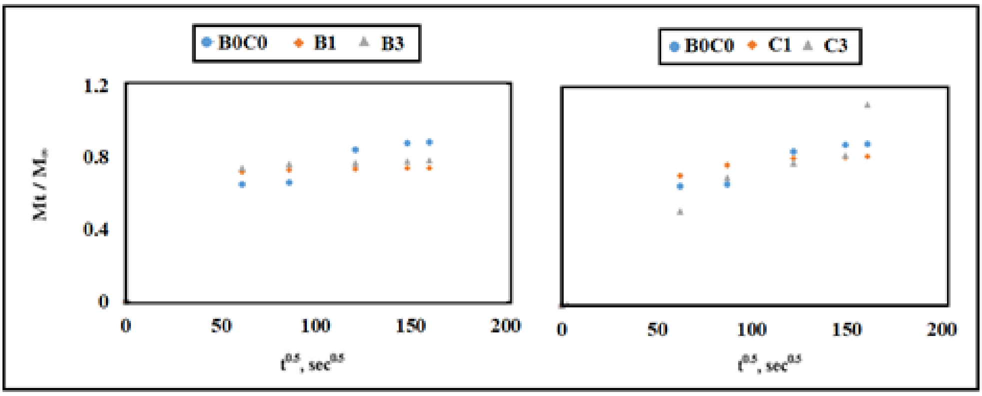

Fig. 4 Uptake ratio of p-PVC films after treatment in hexane

The diffusion coefficient of the plasticizers into the hexane was found to be 37 to 104% times higher than that of into air at 150°C heat treatment, as expected.

Table 2 Diffusion coefficients (Dx**10^{16} m^2/sec**) of plasticizer from the p-PVC films into air and into hexane

	into air						into hexane	
Temperature, °C	**100**		**130**		**150**			
P-PVC Films and Codes	**D*10^{16}, m^2sec^{-1}**	**R^2**	**D*10^{16}, m^2sec^{-1}**	**R^2**	**D*10^{16}, m^2sec^{-1}**	**R^2**	**D*10^{16}, m^2sec^{-1}**	**R^2**
B0C0	2.44	0.99	11.0	0.93	74.7	0.91	3500	0.92
B1	1.97	0.87	9.15	0.91	78.3	0.90	4240	0.92
B3	0.43	0.95	7.07	0.92	44.2	0.74	4600	0.93
C1	13.8	0.94	19.4	0.93	58.5	0.90	4510	0.95
C3	12.4	0.95	83.5	0.90	53.5	0.87	1990	0.92

3.3 Temperature Effect on Diffusion Related Activation Energies

Product lifetime is controlled mainly by the plasticizer migration. Since the activation energy is necessary to separate the plasticizers from the polymer chains, activation energy of plasticizers for diffusion is expected to be inversely proportional to the diffusivity values [1]. The relations of diffusion coefficients with temperature were associated with the Arrhenius equation (Eq. (2)). Activation energies for the diffusion of plasticizers were calculated for the p-PVC films heat treated at 100, 130 and 150°C up to 420 minutes. While the activation energy is 40.62 kJ/mol for the film without BWS and CF, these values are found to be 41.26, 52.28, 36.35 and 41.01 kJ/mol B1, B3, C1 and C3 respectively. Activation energies for the diffusion of plasticizers from p-PVC films into air were given in Table 3.

Table 3 Activation energies for the diffusion of plasticizers from p-PVC films into air

P-PVC FILMS	B0C0	B1	B3	C1	C3
D_o x 10^{10}	3.36	7.10	214	1.62	4.92
E_A, KJmol^{-1}	40.62	41.26	52.28	36.35	41.01

3.4 Determination of Oxidation Index (OI) and Functional Group Changes by using FTIR Spectroscopy

Information concerning the functional group changes of p-PVC films is obtained by means of spectroscopic methods. IR study was used herein to characterise the migration of plasticizer and the oxidation following the carbonyl group formation in the films upon heat treatment in air and upon hexane treatment. IR spectra of p-PVC present some characteristic bands at around 2950 and 1720 cm^{-1} correspond to ester bands which come from plasticizer.

Thermal decompositon can also be observed on the 1720 cm-1 band attributed to the C=O vibrations, becoming deeper because of the carboxylic acids forming by the evolved HCl out of PVC [29]. The peaks in the region of 1444-1414 cm-1 are attributed to the C-H bonds of PVC and, peaks at 1464 cm-1 are attributed to the methyl (-CH3) groups of the plasticizer [30]. The peak at 2920 cm-1 corresponds to –CH2– and –CH– stretching groups [29]. The higher the applied temperature of heat treatment is, the higher the amount of carboxylic acids and hydroperoxydes are, as implied by the band intensities on IR spectra [30]. Since the plasticizers are easy evaporating species, mainly the early stage of oxidation overlaps with the plasticizer migration.

As the heat treatment gets severer in terms of temperature 1720 cm^{-1} peak, which is the ester peak, gets shorter due to the plasticizer migration (Figure5). The highest change of 1720 cm^{-1} peak i.e., the highest plasticizer migration was observed in filler free films. As the boron amount increased, the reduction in the peak height was less. As seen in the Figure5, the peak height decreased with increasing heat treatment time for filler free film. OI evaluation gives better results than those obtained from 1720cm^{-1} peak evaluation since it is expressed as the peak height ratio in the formulation and thus the change in sample thickness during the heat treatment is eliminated.

During the aging and degradation oxygen diffuses into the polymer, reacts with free radicals trapped inside and eventually causes more oxidation. This process results in thickening of the oxidized surface layer and higher oxidation index (OI) as the ageing time gets longer. The oxidation suffered by the p-PVC films during the degradation was monitored by the evaluation of the oxidation index (OI) by means of FTIR spectroscopy. The OI values were obtained by using the absorbances of carbonyl band (C=O) around 1720 cm^{-1} and of a reference group of -CH2- at 2920 cm^{-1} band (Eq.(3)). Changes of OI values for each film in the experiments were given in Figure6. P-PVC does not show important oxidation within these temperature range, as deduced from Figure7. The highest value obtained is about the same for all. Even with small increaments in OI values, it can be said that the oxidation rate gets higher with increasing temperature. Oxidation index values of each film generally increased with longer treatment time and increasing temperature. The lowest OI values were observed on the films having boron waste sludge.

OI method has a weakness to distinguish between plasticizer migration and oxidation due to degradation in case of the presence of ester peaks in the same band.

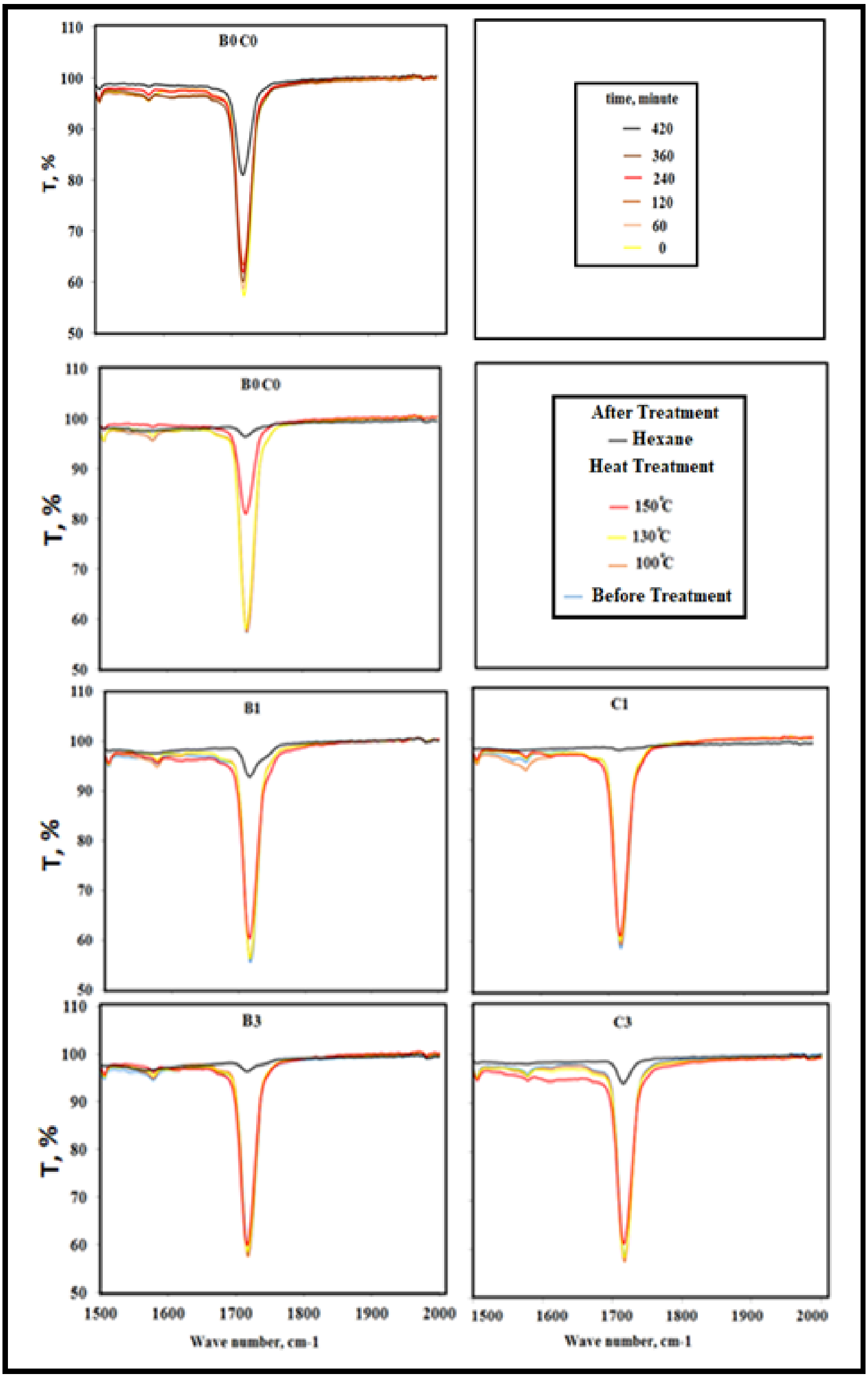

Fig. 5 FTIR spectra of the p-PVC films at 1720 cm-1 (rankings; from top to bottom)

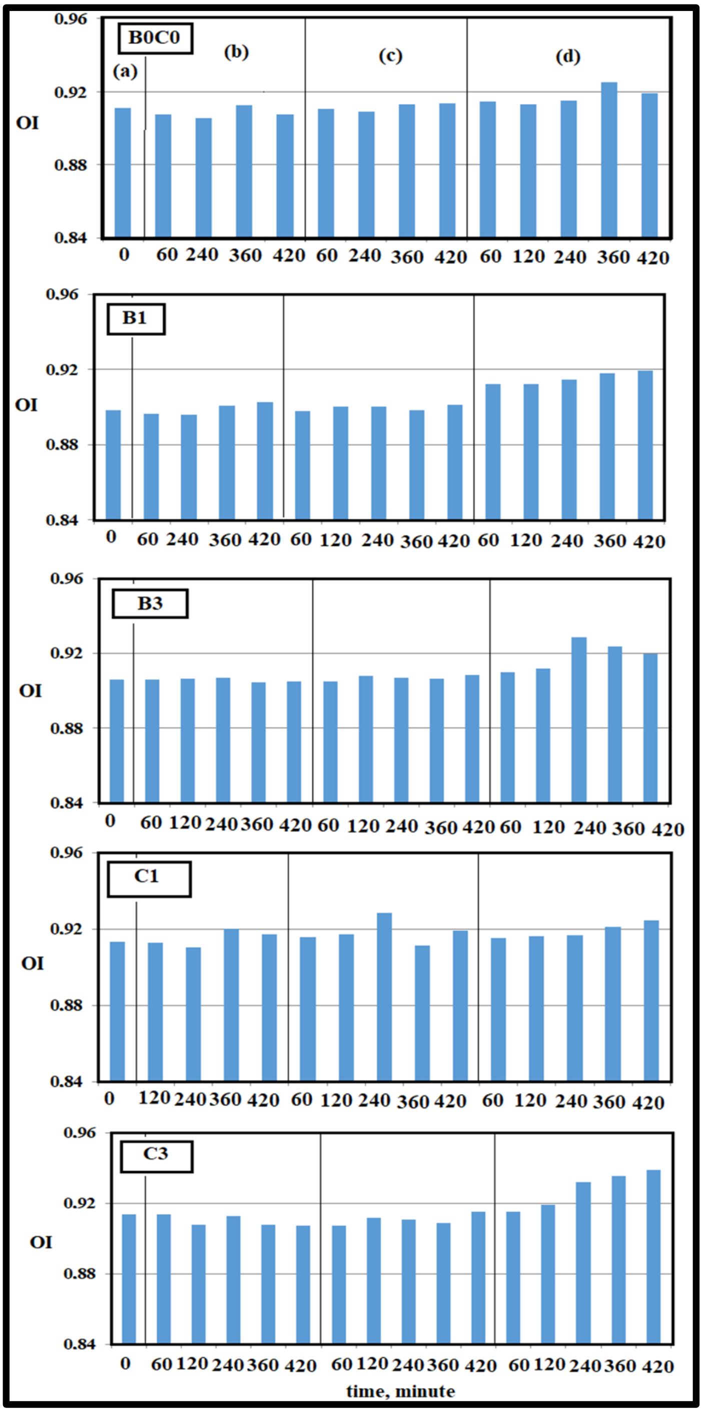

Fig. 6 Change of oxidation index values for p-PVC films according to the time and temperature (before heat treatment (a), after heat treatment (b) 100°C, (c) 130°C and (d) 150°C)

3.5 Discoloration of The Films upon The Treatments

PVC has low thermal stability and the HCl is released as a result of degradation, which is followed by the coloration of the resin [31]. Effect of environmental conditions on the colors of the films were evaluated with bare eyes. The photographs of the films with respect to heat treatment period, temperature and different environment have been depicted in Figure 7. discoloration was observed only when the heat treatment period was long enough thanks to the used efficient stabilizer system. Yellowing of the films proves that dehydrochlorination occurs through conjugated double bond formation [32]. The colors of the films prepared by using CF became the darkest at the long heat treatment period. After consumption of stabilizers, the formation of polyenes reinitiated in turn unzipping process to yield free HCl. The translucent films were still translucent or light yellow at 130°C. This suggests that the stabilization system utilized was not consumed up during processing and therefore, these films can be used under these conditions, without degradation. It was observed that the color of boron waste sludge containing films had less yellowing. It can be said that polyene formation was less in these films. Supporting this result by UV spectroscopic analysis will be the subject of a future study. The amount of additive has shown only a slight difference.

4. Conclusion

Filler-free film showed the highest mass loss compared to other films whereas the films having BWS were lower mass loss. The mass loss in CF films exposed to the hexane medium was higher than that of BWS films. As a result, the BWS added to the films reduces plasticizer migration to the environment in which it contacts. The diffusion coefficients of films increased with temperature as expected. The addition of BWS has reduced the diffusion of the plasticizer from the films into air.

The highest change of 1720 cm^{-1} peak i.e., the highest plasticizer migration was observed in filler free films. As the boron amount increased, the reduction in the peak height was less. The peak height decreased with increasing heat treatment time for filler free film. Oxidation index values of each film generally increased with longer treatment time and increasing temperature. The lowest OI values were observed on the films having BWS.

The colors of the films prepared by using CF became the darkest at the long heat treatment period. It was observed that the color of BWS containing films had less yellowing. It can be said that polyene formation was less in these films.

The addition of boron waste sludge has reduced the diffusion of the plasticizer from the films into air. The addition of boron waste sludge and the increase in the amount of boron waste slurry increased the activation energy value for diffusion of plasticizer. In general, the mass loss of the films decreased with increasing amount of BWS and CF. As a result, the boron waste sludge added to the films contributes to the economy of the country by using waste sludge and reduces the hazard effects by decreasing to plasticizer migration to the environment in which it contacts.

For PVC based films, it can be said that the plasticizers in the films quickly migrated to the oil-like hexane. Therefore, for the films used in food packaging, especially in contact with fatty foods, precautions should be taken or their use should be restricted.

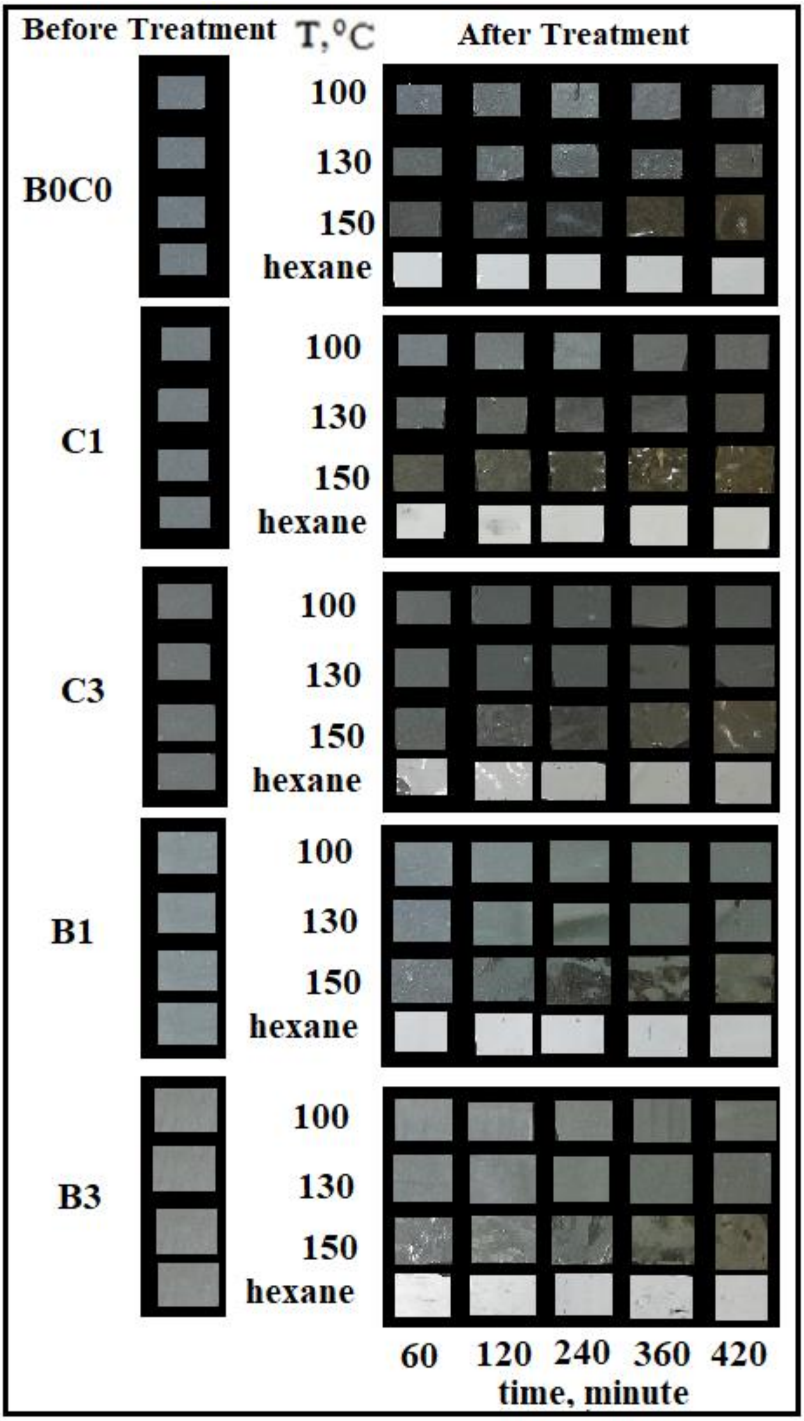

Fig. 7 The color images of the p-PVC films in the course of treatments

Acknowledgements

The financial support of Usak University Research Fund (Project No: 2016/MF002) is gratefully acknowledged. I would like to thank ETI Mineral Institution that supplied BWS. I would like to thank Usak Seramik Co. that supplied CF.

References

[1] Tüzüm-Demir AP, Ulutan S. Migration of phthalate and non-phthalate plasticizers out of plasticized PVC films into air. Journal of Applied Polymer Science. 2013;128: 1948. https://doi.org/10.1002/app.38291

[2] Omrani I, Ahmadi A, Farhadian A, Shendi HK, Babanejad N, Nabid MR. Synthesis of a bio-based plasticizer from oleic acid and its evaluation in PVC formulations. Polymer Testing. 2016;56:237-244. https://doi.org/10.1016/j.polymertesting.2016.10.027

[3] Marcilla A, Garcia S, Garcia-Quesada JC. Migrability of PVC plasticizers. Polymer Testing. 2008;27:221. https://doi.org/10.1016/j.polymertesting.2007.10.007

[4] Jia P, Hub L, Zhang M, Feng G, Zhou Y. Phosphorus containing castor oil based derivatives: Potential non-migratory flame retardant plasticizer. European Polymer Journal. 2017;87:209–220. https://doi.org/10.1016/j.eurpolymj.2016.12.023

[5] Brebu M, Vasile C, Rovana Antonie S, Chiriac M, Precup M, Yang J, Roy C. Study of the natural ageing of PVC insulation for electrical cables. Polymer Degradation and Stability. 2000;67:209. https://doi.org/10.1016/S0141-3910(99)00114-7

[6] Wensing M, Uhde E, Salthammera T. Plastics additives in the indoor environment—flame retardants and plasticizers. Science of the Total Environment. 2005;339:19– 40. https://doi.org/10.1016/j.scitotenv.2004.10.028

[7] Yang Y, Huanga J, Zhanga R, Zhua J. Designing bio-based plasticizers: Effect of alkyl chain length on plasticization properties of isosorbide diesters in PVC blends. Materials & Design, 2017;126:29–36. https://doi.org/10.1016/j.matdes.2017.04.005

[8] Pyeon HB, Park JE, Suh DH. Non-phthalate plasticizer from camphor for flexible PVC with a wide range of available temperature. Polymer Testing, 2017;63:375-381. https://doi.org/10.1016/j.polymertesting.2017.08.029

[9] Jia P, Feng G, Bo C, Hua L, Yanga X, Zhang L, Zhang M, Zhou YA. Composition of phosphaphenanthrene groups-containing castor-oil-based phosphate plasticizer for PVC: Synthesis, characterization and property. Journal of Industrial and Engineering Chemistry, 2018; 60: 192-205. https://doi.org/10.1016/j.jiec.2017.11.006.

[10] Nagorka R, Conrad A, Scheller C, Su¨benbach B, JornMoriske H. Diisononyl 1,2-cyclohexanedicarboxylic acid (DINCH) and Di(2-ethylhexyl) terephthalate (DEHT) in indoor dust samples: Concentration and analytical problems. International Journal of Hygiene and Environmental Health. 2011;214:26-35. https://doi.org/10.1016/j.ijheh.2010.08.005

[11] Royaux A, Fabre-Francke I, Balcar N, Barabant G, Bollard C, Lavedrine B, Cantin S. Long-term effect of silk paper used for wrapping of plasticized PVC objects: Comparison between ancient and model PVC. Polymer Degradation and Stability, 2018;155:183-193. https://doi.org/10.1016/j.polymdegradstab.2018.07.016

[12] Münch F, Hollerer C, Klapproth A, Eckert E, Rüffer A, Cesnjevar R, Goen T. Effect of phospholipid coating on the migration of plasticizers from PVC tubes. Chemosphere, 2018;202:742-749. https://doi.org/10.1016/j.chemosphere.2018.03.136

[13] Egbuchunam TO, Balköse D, Okieimen FE. Effect of zinc soaps of rubber seed oil (RSO) and/or epoxidised rubber seed oil (ERSO) on the thermal stability of PVC plastigels. Polymer Degradation and Stability. 2007;92:1572-1582. https://doi.org/10.1016/j.polymdegradstab.2007.05.002

[14] Liang GG,. Cook WD, Sautereau HJ, Tcharkhtchi A. Diallyl orthophthalate as a reactive plasticizer for improving PVC processibility, Part II: Rheology during cure. Polymer, 2009;50:2655–2663. https://doi.org/10.1016/j.polymer.2009.04.001

[15] Kosuda T, Okada T, Nozaka S, Matsuzawa Y, Shimizu T, Hamanaka S, Mishima S. Characteristics and mechanism of low temperature dehydrochlorination of poly (vinyl chloride) in the presence of zinc(II) oxide. Polymer Degradation and Stability. 2012;97:584-591. https://doi.org/10.1016/j.polymdegradstab.2012.01.009

[16] Helvacı C. Borate deposits: An overview and future forecast with regard to mineral deposits. Boron. 2017;2: 59 – 70.

[17] Başpınar MS, Kartal A, Evcin A, Anasız S. Utilisation of granite sawing mud and borax tailings as a ceramic material. 18, International Mining Congress and Exhibition of Turkey IMCET 2003, ISBN 975-395-605-3, 2003,

[18] Oruç F, Sabah E, Erkan ZE. Evaluation Strategies of Boron Tailings according to Sector II. International Boron Symposium, Eskişehir, Turkey, 385-392, 2004.

[19] Alva G, Lin Y, Fang G. Thermal and electrical characterization of polymer/ceramic composites with polyvinyl butyral matrix. Materials Chemistry and Physics. 2018;205:401 415. https://doi.org/10.1016/j.matchemphys.2017.11.046

[20] Fang Y, Wang Q, Guo C, Song Y, Paul A. Effect of zinc borate and wood flour on thermal degradation and fire retardancy of Polyvinyl chloride (PVC) composites. Cooper Journal of Analytical and Applied Pyrolysis. 2013;100:230-236. https://doi.org/10.1016/j.jaap.2012.12.028

[21] Cui X, Ding P, Zhuang N, Shi L, Song N, Tang S. Thermal Conductive and Mechanical Properties of Polymeric Composites Based on Solution-Exfoliated Boron Nitride and Graphene Nanosheets: A Morphology-Promoted Synergistic Effect; ACS Applied Materials and Interfaces, 2015;7:19068–19075. https://doi.org/10.1021/acsami.5b04444

[22] Liu H, Dong L, Xie H, Xiong C. Novel-Modified Kaolin for Enhancing the Mechanical and Thermal Properties of Poly (vinyl chloride). Polymer Engineering and Science. 2012. https://doi.org/10.1002/pen.23161

[23]. Zhang ZH, Zhu HJ, Zhoua CH, Wang H. Geopolymer from kaolin in China: An overview. Applied Clay Science, Applied Clay Science 2016;119:31-41. https://doi.org/10.1016/j.clay.2015.04.023

[24] Awad WH, Beyer G, Benderly D, Ijdo WL, Songtipya P, Jimenez-Gasco MM, Manias E, Wilkie CA. Material properties of nanoclay PVC composites. Polymer, 2009;50:1857–1867. https://doi.org/10.1016/j.polymer.2009.02.007

[25] Kovacic T, Mrklic Z. The kinetic parameters for the evaporation of plasticizers from plasticized poly (vinyl chloride). Thermochimica Acta. 2002;381:49-60. https://doi.org/10.1016/S0040-6031(01)00643-8

[26] Ismail AF, Lorna W. Penetrant-induced plasticization phenomenon in glassy polymers for gas separation membrane. Seperation and Purification Technology. 2002;27:173-194. https://doi.org/10.1016/S1383-5866(01)00211-8

[27] Shi W, Zhang J, Shi XM, Jiang GD. Different Photodegradation Processes of PVC with Different Average Degrees of Polymerization. College of Materials Science and Engineering, 2006, DOI 10.1002/app.25389. https://doi.org/10.1002/app.25389

[28] Zoller A, Marcilla A. Soft PVC foams: Study of the gelation, fusion, and foaming processes. I. Phthalate ester plasticizers. J Appl Polym Sci., 2011; 121: 1495–1505. https://doi.org/10.1002/app.33671

[29] Atakul Savrık S, Balköse D, Ulutan S, Ü lkü S. Characterization of poly(vinyl chloride) powder produced by emulsion polymerization. Journal of Thermal Analysis and Calorimetry. 2010;101:801. https://doi.org/10.1007/s10973-010-0942-2

[30] Tüzüm Demir AP. Low Migration Plasticizers for PVC Applications, PhD. Thesis, Natural and Applied Sciences Institute, Ege University, Izmir, Turkey, 2011.

[31] Benavides R, Castillo BM, Castañeda AO, López GM, Arias G. Different thermooxidative degradation routes in poly (vinyl chloride), Polymer Degradation and Stability. 2001;73:417-423. https://doi.org/10.1016/S0141-3910(01)00122-7

[32] Tüzüm-Demir AP, Ulutan S. Assessment of degradation of plasticized poly(vinyl chloride) films through polyene formation under isothermal conditions. Journal of Applied Polymer Science. 2018. https://doi.org/10.1002/app.46092

Research on Engineering Structures & Materials
journal homepage: http://jresm.org
Research Group

Research Article

Adsorption kinetics, equilibrium and thermodynamics of gas-phase toluene onto char produced from almond shells

Sinan Kutluay*[,a], Orhan Baytar[b], Ömer Şahin[c]

Department of Chemical Engineering, Siirt University, Siirt, Turkey

Article Info

Article history:
Received 22 Nov 2018
Revised 14 Mar 2019
Accepted 28 Mar 2019

Keywords:

Adsorption;
Char;
Isotherms;
Kinetics;
Thermodynamics;
Toluene

Abstract

Toluene is the primary material in chemical process industries and is often used as a raw material in the production of many chemicals and as a solvent in many engineering processes. In this study, the material of char, which is used as an adsorbent, was produced from almond shells. The adsorption process of gas-phase toluene onto char was investigated using a laboratory-scale fixed-bed reactor under atmospheric pressure. The structure of the char was characterized by BET and FTIR. The influences of adsorption parameters such as nitrogen (N_2) flow rate as the gas-phase toluene carrier, char amount, gas-phase toluene concentration at the inlet and the adsorption temperature on both the adsorption capacity and adsorption efficiency were examined. It was found that the adsorption of the gas-phase toluene onto char could be well represented by the pseudo-second-order kinetic model. Equilibrium isotherm data were analyzed by the Langmuir and Freundlich isotherm models and the results indicated that the adsorption process was described well by the Langmuir isotherm model. The maximum monolayer adsorption capacity (q_{max}) of the char was determined as 15.42 mg g^{-1} for 303 K. Thermodynamic parameters such as $\Delta G°$ = -7.93 kJ mol^{-1}, $\Delta H°$= -17.18 kJ mol^{-1}, $\Delta S°$= -0.013 kJ mol^{-1} K^{-1} showed that the adsorption process was spontaneous, exothermic and physical. The results showed that the material of char produced from almond shells could be used as a biosorbent to remove the material of gas-phase toluene from various industrial and natural sources through the adsorption method.

1. Introduction

Volatile organic compounds (VOCs) are important air pollutant components which are found in the atmosphere and originate from all municipal and industrial areas [1]. VOCs are pollutants that are emitted to the environment from chemicals, petrochemicals and many other industries. There are numerous sources of VOCs including the evaporation of chemicals such as solvents, thinners, scrubbers and lubricants, flue gas emissions from the burning of fossil fuels for industrial and urban activities and the incineration of wastes resulting from urban life, oil refineries and stations, etc. [2-5]. VOCs are not removed before being released to the environment and have serious detrimental effects on the environment and thus on living things [6]. VOCs, which can readily mix into the air with direct evaporation, can lead to fatalities when inhaled. Various VOCs can cause persistent health problems due to their negative properties. VOCs accumulate on the leaves and refined crops which, in turn, affects photosynthesis. Other VOCs, which are carcinogenic, can lead to death by intoxication [3]. The most common VOCs are benzene, toluene, ethylbenzene and xylene, collectively known as BTEX. These VOCs are particularly notable due to their health risks. Toluene is within the group of components that do not carry

---

*Corresponding author: kutluays2012@gmail.com, sinankutluay@siirt.edu.tr
[a] orcid.org/0000-0002-6340-0752; [b] orcid.org/0000-0002-2915-202X; [c] orcid.org/0000-0003-4575-3762
DOI: http://dx.doi.org/10.17515/resm2019.73en1122

cancer risk. The most important health risk of toluene is its acute and chronic effects on the central nervous system. Toluene is a VOC that is abundantly found in the environment as it is the primary material in chemical process industries and often used as a raw material in the production of many chemicals and as a solvent in many engineering processes [7]. Toluene has been reported to cause indoor and outdoor pollution even at low concentrations in its gas-phase [8].

There are many processes used in the removal of VOCs such as thermal and catalytic combustion, biofiltration absorption, condensation, thermal oxidation, catalytic oxidation and adsorption. Among VOC removal and recovery techniques, the nondestructive adsorption process which has many advantages in terms of process conditions and applicability is one of the most appropriate and preferred methods for removing VOCs [3, 9, 10]. The adsorption process is a useful technology for the separatin and removal of VOCs because it can be developed with relatively low cost in addition to providing flexibility and simplicity in process design, operations and maintenance [11, 12]. Furthermore, the adsorption process is a renewable process that is the least harmful [13, 14]. This technique of adsorbing the VOCs provides high efficiency in the removal of solvents and VOCs both at low and high concentrations [14]. Adsorption is usually carried out on a fixed-bed filled with adsorbents. There are many studies on fixed bed modeling in the literature [15, 16]. Allen et al. [17] developed theoretical mathematical equations for the adsorbed in the adsorbent particles given by injection to a gas stream. The equations in their study were solved using parameters such as different gas flow rate and adsorbent feed rate and the results were analyzed. In other studies, theoretical and experimental results were evaluated together [18, 19]. Various solid materials used as adsorbents in the adsorption process have a porous structure and the inner surface areas are larger than the outer surface areas. The adsorption on the inner surface of the layer does not occur as easily as it does on the outer surface. This is because gas molecules interact with atoms, molecules or ions when entering the surfaces. When this occurs, condensation takes place in the inner surface which is called capillary condensation. Adsorption can take place in the form of physical adsorption, otherwise known as van der Waals adsorption, or chemical adsorption, otherwise known as chemisorption [13, 14, 20].

Almond shells, which are abundant and low-cost residues, are suitable for being used as raw materials for the preparation of char. Material for char is produced by heating biomass in the total or partial absence of oxygen. Pyrolysis is the most common technology employed to produce char and also occurs in the early stages of the combustion and gasification processes.

In the literature, there are no studies conducted on the adsorption of gas-phase toluene onto char produced from almond shells in a dynamic system. For this reason, within the context of the main purpose of this study, the effects of adsorption parameters such as the flow rate of nitrogen (N_2) as the gas-phase toluene carrier, char amount, gas-phase toluene concentration at the inlet and the adsorption temperature, which are important in the adsorption process, were examined and the results were optimized using gas chromatography method. In addition, adsorption kinetics, isotherms and thermodynamics of the gas-phase toluene onto char were investigated at different temperatures.

2. Materials and Method

2.1. Materials

The almond shells used in this study were obtained from the province of Siirt which is located in the South-East of Turkey. The almond shells were ground in a mortar and sieved to a particle size of -500+125 μm. The obtained samples were stored in closed containers to be used in char production. The adsorbate used in this study was analytical grade toluene (Sigma Aldrich, 99.0%).

2.2. Production of Char

The production of char from almond shells was carried out in a vertical electric furnace. In the production process of the char, the almond shells (100 g) with a particle size of -500+125 μm were placed in a ceramic crucible bowl and pyrolyzed at 350°C for 30 min in a box furnace. The heating rate was not controlled but was consistently 8-10°C/min through the heat-uptime. N_2 of 99.9% purity was used as a sweep gas in the furnace to prevent oxygen from entering. After pyrolysis, the material was allowed to cool overnight in the furnace with nitrogen as the sweep gas. The obtained material was kept in closed bottles to be used in the experimental studies.

2.3. Dynamic Adsorption Process of Gas-Phase Toluene onto Char

The experimental setup used in the adsorption studies is schematically shown in Figure 1. The gas-phase toluene adsorption experiments of the char adsorbent were performed in the fixed bed of a Pyrex-glass reactor with a height of 16 cm and an internal diameter of 0.9 cm.

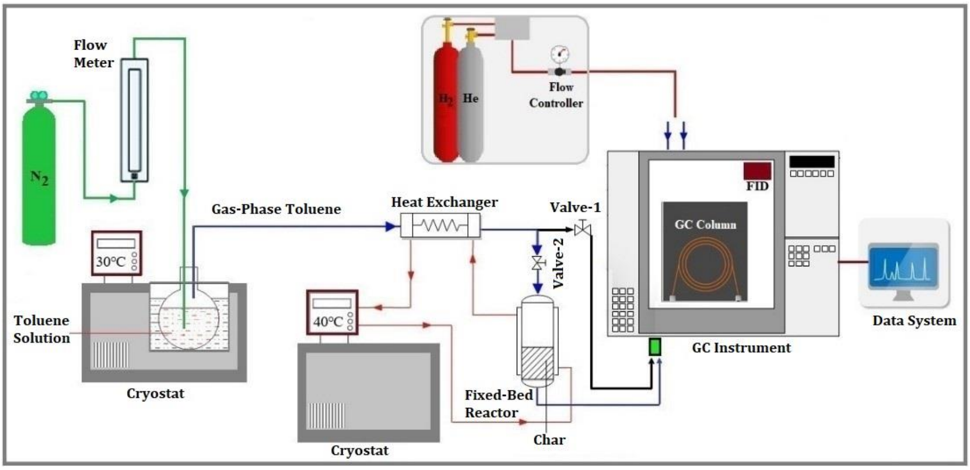

Fig. 1 Schematic diagram of experimental system for the dynamic adsorption of gas-phase toluene onto char

In order to determine the optimum adsorption conditions, the study was carried out under atmospheric pressure at different N_2 flow rates (50-120 mL min^{-1}) as the gas-phase toluene carrier, char amounts (0.25-1.00 g), gas-phase toluene concentrations at the inlet (10.00-15.00 ppm) and temperatures (293-323 K). For this purpose, 300 mL of the toluene solution to be subjected to the vapor dynamic adsorption was placed in a 500 mL glass balloon and then placed in the thermostat set to the study temperature. The gas-phase toluene was introduced into the fixed bed by using N_2 as a carrier gas and it was continuously adsorbed onto the char. The N_2 flow rate during the adsorption process was measured using a volumetric flowmeter. The internal temperature of the jacketed adsorbent, in which the adsorption was carried out, and the gas-phase toluene temperature was kept constant by using the thermostat connected to both the adsorber and the heat exchanger. The concentration of the gas-phase toluene in the N_2 stream at the inlet of the adsorber was analyzed while the valve-2 line was closed and the valve-1 bypass line was open. When the concentration of the gas-phase toluene in the N_2 stream at the inlet of the adsorber reached a steady state, approximately 0.50 g of char was weighed out and charged into the adsorption column after which the experiments were carried out by turning the valve-1 line to the closed position and the valve-2 line to the open position. The concentrations of the gas-phase toluene in the N_2 stream at the inlet and outlet of the adsorber (10.00, 12.50, 13.50 and 15.00 ppm) were produced using a PID controlled heated thermostat at 293, 303, 313 and 323 ± 0.1 K, respectively. The char particles were supported by microsieve at the outlet of the adsorber. The carrier gas containing a previously arranged concentration of the gas-phase toluene was passed through the column until the gas-phase toluene concentration became stable. The concentrations of the gas-phase toluene at the inlet and outlet of the adsorber were measured by a gas chromatography equipped with a flame ionization detector (GC-FID, GC 910, Buck Scientific) and recorded by a computer. After the dynamic adsorption experiments, the adsorption capacity of the gas-phase toluene onto char was determined by calculating the toluene concentrations in the gas flow before and after it moved through the adsorption column. For this determination, the gas-phase toluene was injected continuously to gas chromatography (GC) and was measured every 10 min. The temperature programming of the GC oven started at T = 80°C after which it was increased at 10°C min^{-1} until it reached 200°C and remained at T = 200°C for 3 min (total of 15 min). The retention time was defined as the closest to the peak of toluene and the determination of gas-phase toluene concentrations was carried out by means of a four-point calibration curve. Analyzes in the experiments were performed at thrice and they showed good reproducibility.

2.4. Measurement of the Adsorption Capacity and the Adsorption Efficiency

The adsorption capacity and adsorption efficiency of the gas-phase toluene onto char obtained from almond shells were measured under different experimental conditions.

The adsorption capacity was determined using the following equation [21]:

$$q_t = \sum_0^n \left[\frac{F}{m}(C_{in} - C_{eff})\Delta t\right] \qquad (1)$$

Where, q_t (mg g^{-1}) is the adsorption capacity, that is the amount of gas-phase toluene adsorbed onto char, which was integrated from t=0 to t (min), m *(g)* is the mass of adsorbent, F (L min^{-1}) is the gas flow rate, n is the number of samples taken, C_{in} (ppm) and C_{eff} (ppm) are the concentrations of gas-phase toluene in the N_2 stream at the inlet and outlet (after adsorption) of the adsorber, respectively. In the adsorption process, q_t=qe was achieved when the equilibrium time (t_e) was reached and it refers to the adsorption capacity at equilibrium.

The adsorption efficiency of the gas-phase toluene onto char is defined as follows:

$$\text{Adsorption efficiency (\%)} = \frac{C_{in} - C_e}{C_{in}} \times 100 \qquad (2)$$

Where, C_{in} (ppm) and C_e (ppm) are the concentrations of the gas-phase toluene at the inlet and equilibrium of the adsorber, respectively.

3. Results and Discussion

In this study, the characterization of the char was performed by BET surface area and FTIR measurements. The influences of adsorption conditions on the adsorption process of the gas-phase toluene onto char were determined in a continuous system. In addition, adsorption kinetics, isotherms and thermodynamics of adsorption process were investigated at different temperatures. To demonstrate reproducibility, data in Tables and Figures were marked with error bars.

3.1. Characterization of Char

The structure of the char produced from almond shells was characterized by BET and FTIR. The functional groups of the produced materials were determined with a Bruker Vertex 70 FTIR instrument in the range of 4000–600 cm^{-1} wave number. The FTIR spectra of char adsorbent was analysed in the range of 4000-600 cm^{-1}, and the result was presented in Figure 2. As seen from Figure 2, there are more than one functional group in the structure of char. The peak at 3700 cm^{-1} shows the presence of the OH-functional group bound by hydrogen bonds. The peak at 2380 cm^{-1} indicates the presence of C = C bonds. The peaks in the range of 2250-2000 cm^{-1} are dimmer and show the presence of the COOH functional group. Nitrogen adsorption-desorption of the BET surface area at 77 K was determined by Quantachrome Nova 1200 series instrument. The BET surface area of the char used in this study as adsorbent was determined as 463 m^2 g^{-1}.

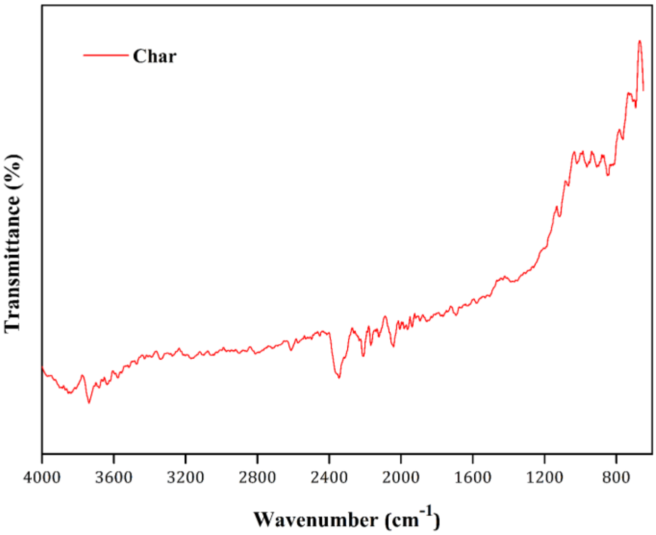

Fig. 2 The FTIR spectra of char adsorbent produced from almond shells

3.2. Influence of Flow Rate on Adsorption Process

In order to illustrate the influence of the flow rate on both the adsorption capacity and the adsorption efficiency of the gas-phase toluene onto char, different flow rates of 50, 75, 100 and 120 mL min^{-1} were used under the experimental conditions of char amount of 0.50 g, temperature of 303 K and concentration of gas-phase toluene at the inlet of 12.50 ppm and the results are given in Figure 3. To determine the equilibrium time of the adsorption, the adsorption capacity was investigated according to the time (0-120 min) (Figure 3a). As shown in Figure 3a, depending on the increase in the flow rate, the adsorption capacity increased. However, in Figure 3b, the adsorption capacity at equilibrium increased with the increasing flow rate, while the adsorption efficiency did not change. This result means that the flow rate in Equation 2, in which the adsorption capacity was determined, changes the adsorption capacity in proportion to the numerical value it has. In other words, it was observed that the amount of toluene adsorbed onto char does not increase at higher flow rates.

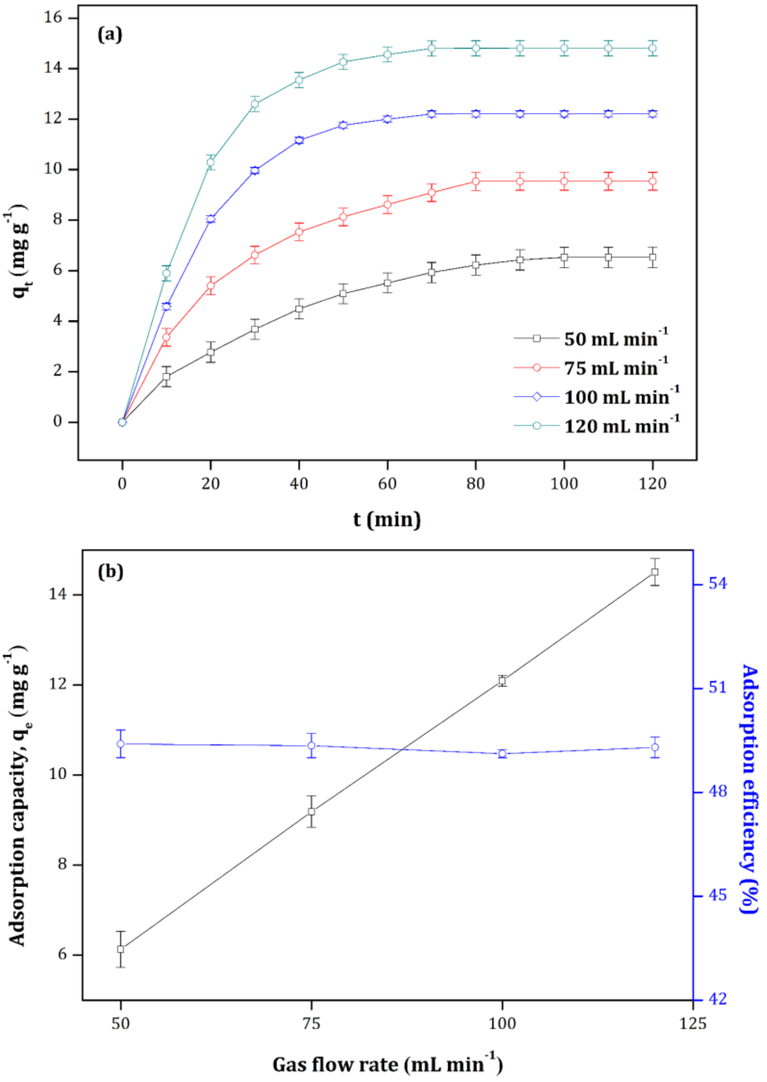

Fig. 3 Influence of flow rate of N_2 as the carrier gas on the adsorption capacity with time (a), and the adsorption capacity at equilibrium and the adsorption efficiency (b)

3.3. Influence of the Char Amount on Adsorption

The amount of adsorbent is one of the most important parameters in the adsorption process. In order to illustrate the influence of the char amount on both the adsorption capacity and the adsorption efficiency of the gas-phase toluene onto char, different char amounts of 0.25, 0.50, 0.75 and 1.00 g were used under the experimental conditions of temperature of 303 K, flow rate of 100 mL min^{-1} and concentration of gas-phase toluene at the inlet of 12.50 ppm and the results are given in Figure 4. To determine the adsorption equilibrium time, the adsorption capacity was investigated according to the time (0-120 min) (Figure 4a). Figure 4a shows that an increase in the amount of char caused a decrease in the adsorption capacity. The possible causes of this result can be expressed as the increase in the amount of char and the increase in the number of activated sites available and the non-saturation of these zones [22], the increase of the activated site ratio of the gas-phase toluene and adsorbent surface and the absence of toluene ions in the medium [23]. As seen in Figure 4b, it was observed that the adsorption capacity at equilibrium decreased with the increasing amount of char, the adsorption efficiency increased up to 0.50 g of char, and did not change with higher amounts of char. An increase in the amount of adsorbent increased the number of active sites available for adsorption, thus increasing the adsorption efficiency [24]. In this study, the minimum amount of adsorbent corresponding to maximum adsorption for char was 0.50 g.

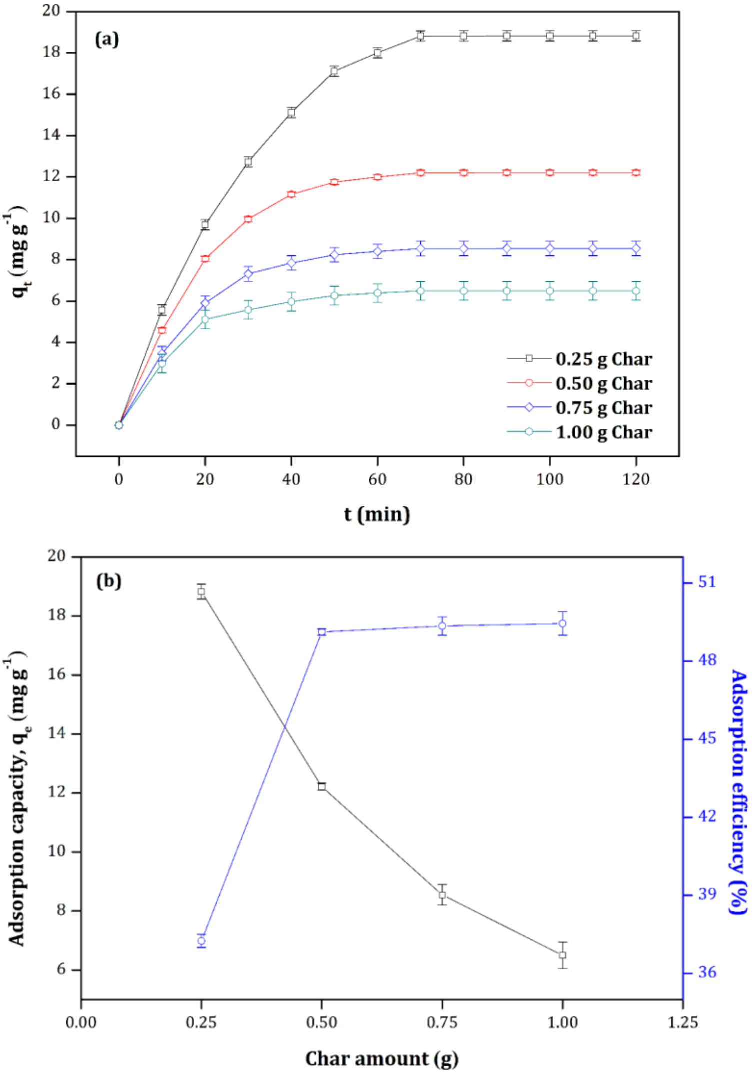

Fig. 4 Influence of the char amount on the adsorption capacity with time (a), and the adsorption capacity at equilibrium and the adsorption efficiency (b)

3.4. Influence of Concentration of Toluene at the inlet on Adsorption Process

In order to illustrate the influence of the concentration of the gas-phase toluene at the inlet on both the adsorption capacity and adsorption efficiency of the gas-phase toluene onto char, different the gas-phase toluene concentrations at the inlet of 10.00, 12.50, 13.50 and 15.00 ppm were used under experimental conditions such as a flow rate of 100 mL min^{-1}, temperature of 303 K and char amount of 0.50 g. The results are given in Figure 5. To determine the adsorption equilibrium time, the adsorption capacity was investigated in accordance with the time (0-120 min) (Figure 5a). As shown in Figure 5a, it was observed that the adsorption capacity increased up to 12.50 ppm and did not change at higher concentrations due to the increase in the gas-phase toluene concentration at the inlet.

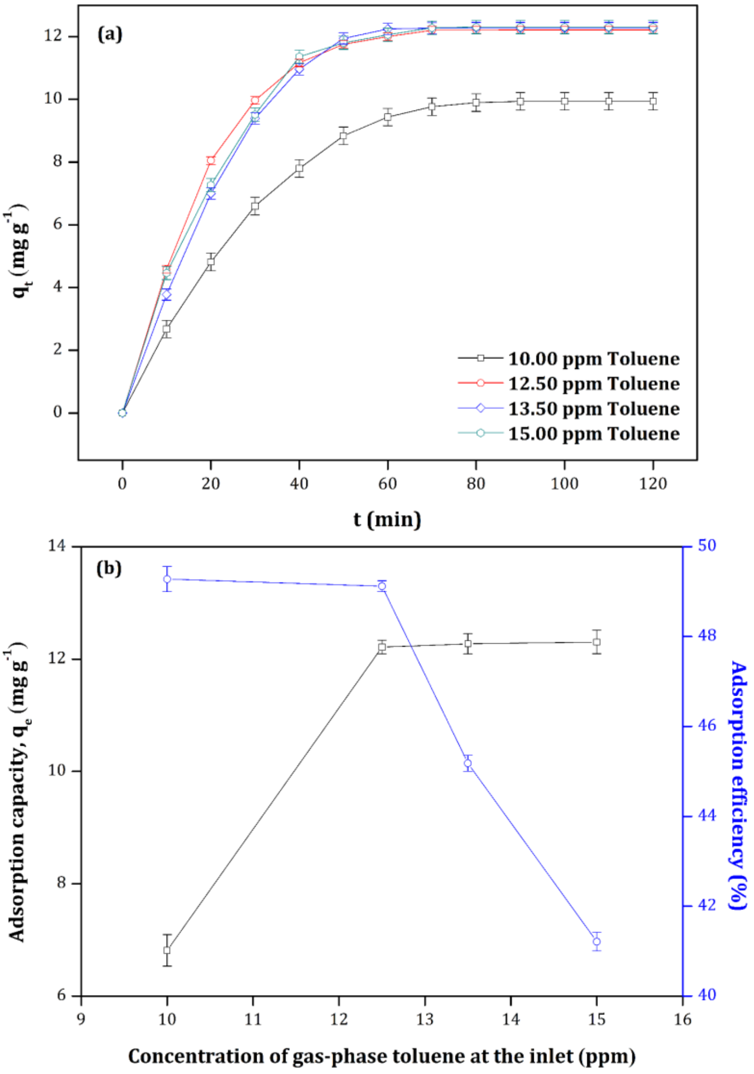

Fig. 5 Influence of concentration on the adsorption capacity with time (a), and the adsorption capacity at equilibrium and the adsorption efficiency (b)

In addition, the increase in the concentration of the gas-phase toluene at the inlet shows that the equilibrium adsorption capacity was reached in a shorter time. These tendencies can be explained with the constant present specific surface area and adsorption area on the char surface and with the fact that an increase in the concentration of the gas-phase toluene at the influent naturally results in a shorter exhaustion time.

In Figure 5b, the increase in the concentration of the gas-phase toluene at the inlet shows that the adsorption capacity at equilibrium increased up to 12.50 ppm and did not change at higher concentrations.

However, the adsorption efficiency was observed to decrease at concentrations greater than 12.451 ppm (Figure 5b). The possible reasons for these circumstances may be the fact that the adsorption capacity, which is a function of the equilibrium concentration, increases with the increasing concentration of the gas-phase toluene at the inlet [25], or with the increase in the number of adsorbate molecules in the vapor that accelerate the adsorption to reach the equilibrium [26].

In all these evaluations, the concentration of the gas-phase toluene at the inlet was taken as 12.50 ppm in other adsorption experiments.

3.5. Influence of Temperature on Adsorption Process

In the adsorption process, temperature plays an important role in the adsorption process. In order to illustrate the influence of the adsorption temperature on both the adsorption capacity and adsorption efficiency of the gas-phase toluene onto char, temperatures of 293, 303, 313 and 323 K were used under experimental conditions such as flow rate of 100 mL min^{-1}, concentration of gas-phase toluene at the inlet of 12.50 ppm and char amount of 0.50 g and the results are given in Figure 6.

To determine the adsorption equilibrium time, the adsorption capacity was investigated according to the time (0-120 min) (Figure 6a). Figure 6a shows that the adsorption capacity did not change until the adsorption temperature reached 303 K and decreased at higher temperatures.

As shown in Figure 6b, both the adsorption capacity at equilibrium and the adsorption efficiency did not change until the adsorption temperature reached 303 K while they decreased at higher temperatures.

Since gas adsorption is an exothermic process, the adsorption capacity decreases with the increasing temperature. This result shows that physical adsorption is a mechanism that separates the gas-phase from liquid phase [27].

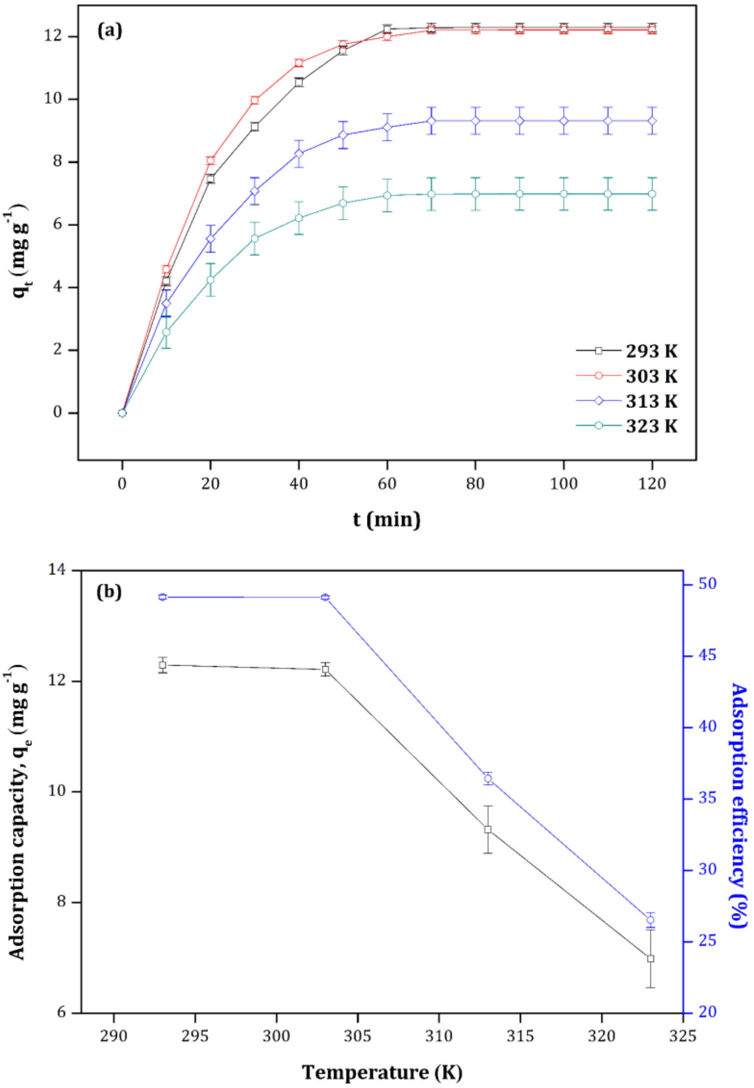

Fig. 6 Influence of temperature on the adsorption capacity with time (a), and the adsorption capacity at equilibrium and the adsorption efficiency (b)

3.6. Adsorption Kinetic Studies

Adsorption kinetics is important in understanding the adsorption dynamics between adsorbate and adsorbent. According to adsorption kinetic data, the degree of adsorption, rate constant and the dynamics of adsorption were determined. Important information regarding the design and modeling of the adsorption process can be obtained with kinetic parameters [28]. Pseudo-first-order and pseudo-second-order models were used to determine the adsorption kinetics and mechanisms in this study. The validity of kinetic models was assessed by R^2, regression coefficient, and Δq (%) [29]:

$$\Delta q(\%) = 100\sqrt{\frac{\sum[(q_{exp}-q_{mod})/q_{exp}]^2}{N-1}} \tag{3}$$

Where, N is the number of data points, q_{exp} and q_{mod} (mg g^{-1}) are the adsorption capacities of kinetic experiments and models, respectively and Δq is the normalized standard deviation.

The pseudo-first-order kinetic model is the first equation to explain the adsorption capacity and adsorption rate [30].The pseudo-first-order kinetic model equation [31] is given below:

$$\ln(q_e - q_t) = \ln q_e - k_1 t \tag{4}$$

Where, q_e (mg g^{-1}) and q_t (mg g^{-1}) are the adsorption capacities at equilibrium and at time t, respectively. k_1 (min^{-1}) is the rate constant, and t (min) is the adsorption time. k_1 is calculated from the slope of the plot of ln(q_e−q_t) against t.

The pseudo-second-order kinetic model equation [32] is given below:

$$\frac{t}{q_t} = \frac{1}{k_2 {q_e}^2} + \frac{1}{q_e}t \tag{5}$$

Where, k_2 (g mg^{-1} min^{-1}) is the rate constant. q_e and k_2 are calculated from the slope and intercept of the plot of t/q_t against t, respectively.

In order to understand the adsorption process of the gas-phase toluene onto char, pseudo-first-order and pseudo-second-order kinetic models were applied to the experimental data obtained at different temperatures. The linear and non-linear plots of the pseudo-first-order and pseudo-second-order kinetic models are shown in figures 7(a)-(b) and 8(a)-(b), respectively. All kinetic parameters, correlation coefficient (R^2) and Δq (%) values obtained from the linear plots of the kinetic models at different temperatures are listed in Table 1. Figure 7(a)-(b) shows that the pseudo-first-order kinetic model did not give beneficial results for the adsorption of the gas-phase toluene onto char, indicating that it is not in good agreement with the adsorption data. On the other hand, Figure 8(a)-(b) shows that the pseudo-second-order kinetic model gave beneficial results for the adsorption of the gas-phase toluene onto char which shows a satisfactory agreement with the experimental adsorption data. All these results show that the R^2 values of the pseudo-first-order kinetic model showed a weak correlation of the gas-phase toluene adsorption onto char and the Δq values showed a high standard deviation, whereas the R^2 values of the pseudo-second-order kinetic model were higher than 0.98 and the Δq values were less than 3% (Table 1).

Table 1. Kinetic model parameters for the adsorption of gas-phase toluene onto char

Models	Parameters	Temperature (K)			
		293	303	313	323
Pseudo-first-order	q_e (mg g^{-1})	13.41±0.14	13.25±0.12	9.461±0.43	7.154±0.52
	k_1 (min^{-1})	0.076±0.14	0.074±0.12	0.035±0.43	0.019±0.52
	R^2	0.889±0.14	0.847±0.12	0.874±0.43	0.837±0.52
	Δq (%)	6.187±0.14	8.356±0.12	7.424±0.43	8.773±0.52
Pseudo-second-order	q_e (mg g^{-1})	14.521±0.14	14.35±0.12	10.02±0.43	7.86±0.52
	k_2 (g mg^{-1} min^{-1})	0.0016±0.14	0.005±0.12	0.008±0.43	0.009±0.52
	R^2	0.9999±0.14	0.999±0.12	0.997±0.43	0.998±0.52
	Δq (%)	0.5118±0.14	0.754±0.12	1.356±0.43	1.278±0.52

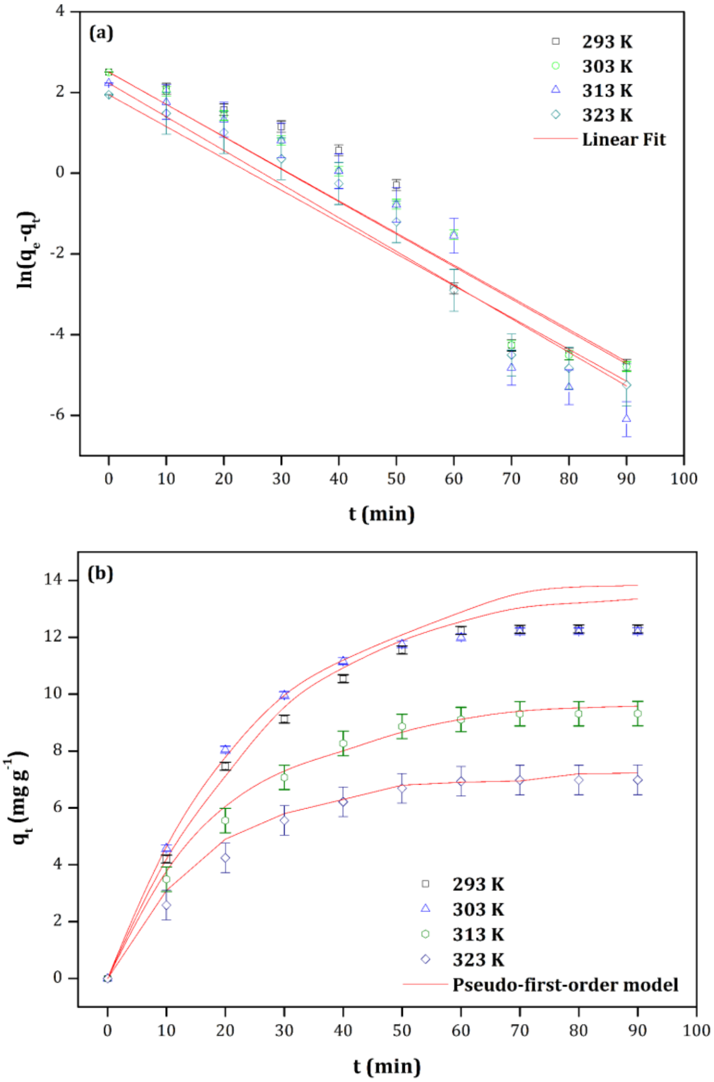

Fig. 7 Pseudo-first-order kinetic model in linear (a) and non-linear (b) methods and experimental kinetics for the adsorption of gas-phase toluene onto char

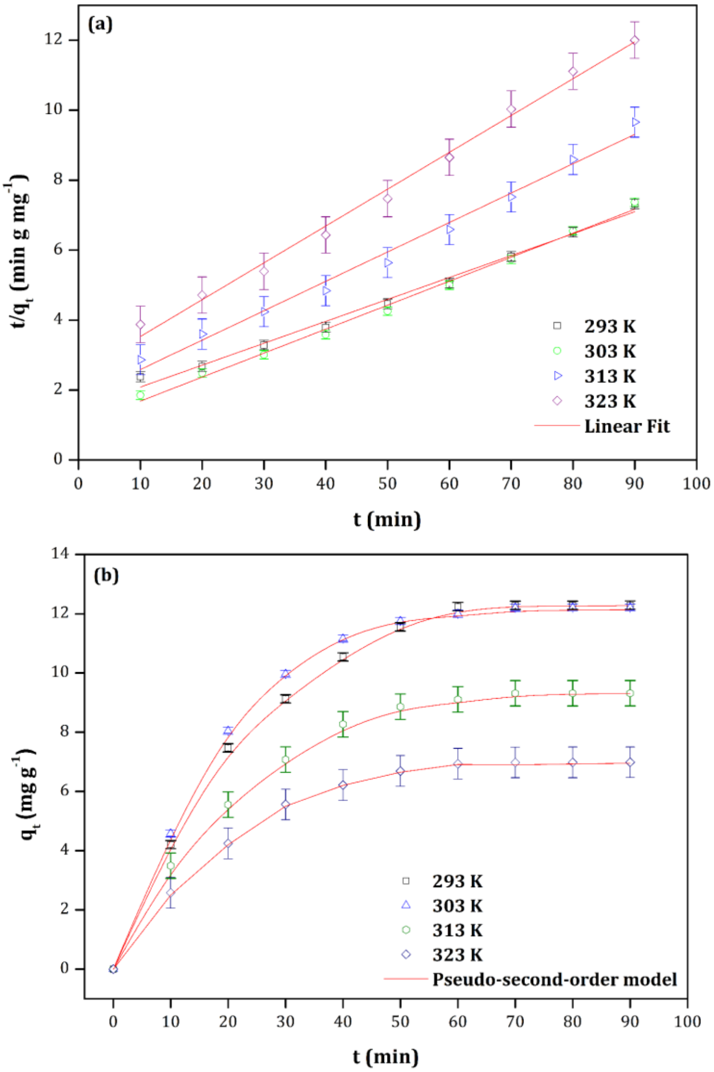

Fig. 8 Pseudo-second-order kinetic model in linear (a) and non-linear (b) methods and experimental kinetics for the adsorption of gas-phase toluene onto char

3.7. Adsorption Isotherm Studies

The most important factors in the interaction between adsorbate and adsorbent are the load and structure of the adsorbent, surface properties of the adsorbent, hydrophobic and hydrophilic structure of the adsorbent, hydrogen bonds, electrostatic interaction, steric effect and Van der Walls forces. The equilibrium studies giving the adsorption capacity of the adsorbent are explained using the adsorption isotherm models [33]. To understand the adsorption process of the gas-phase toluene onto char and to evaluate the equilibrium isotherm, experimental adsorption data obtained at different temperatures were modeled using Langmuir and Freundlich isotherm models. The validity of the isotherm models was assessed by R^2, regression coefficient, and *Δq (%)*.

The Langmuir isotherm model was formed by the adoption of monolayer adsorption. According to this model, monolayer adsorption occurs between the outer surface of the adsorbent and the adsorbate due to the rapid reduction of the distance between the intermolecular forces [34]. The Langmuir isotherm model equation [35] is given below:

$$\frac{C_e}{q_e} = \frac{1}{q_{max}\,K_L} + \frac{C_e}{q_{max}} \qquad (6)$$

Where, q_{max} (mg g^{-1}) is the monolayer adsorption capacity, and K_L (L mg^{-1}) is the Langmuir adsorption constant. q_{max} and K_L are calculated from the slope and intercept of the plot of C_e/q_e against C_e, respectively.

The Freundlich isotherm model was developed by adopting adsorption on heterogeneous surfaces. It is accepted that the active areas are reduced with bonding forces [26]. The Freundlich isotherm model equation [36] is given below:

$$\ln q_e = \ln K_F + \frac{1}{n} \ln C_e \qquad (7)$$

Where, K_F [(mg/g) (L/mg)$^{1/n}$] is Freundlich adsorption constant. $1/n$ indicates the heterogeneity of data distribution of active centers and is a measure of the adsorption intensity. $1/n$ and K_F are calculated from the slope and intercept of the plot of lnq_e against lnC_e, respectively.

Plots of Langmuir and Freundlich isotherm models are presented in figures 9 and 10, respectively. All the obtained parameters, correlation coefficient (R^2) and Δq values calculated from the linear plots of the isotherm models are reported in Table 2.

Table 2. Isotherm model parameters for the adsorption of gas-phase toluene onto char

Models	Parameters	Temperature (K)			
		293	303	313	323
Langmuir	q_{max} (mg g^{-1})	15.05±0.14	15.42±0.12	11.12±0.43	9.35±0.52
	K_L (m^3 mg^{-1})	0.058±0.14	0.043±0.12	0.036±0.43	0.029±0.52
	R^2	0.999±0.14	0.998±0.12	0.988±0.43	0.991±0.52
	Δq (%)	1.49±0.14	1.92±0.12	2.98±0.43	2.02±0.52
Fruendlich	K_F [(mg g^{-1}) (m^3 mg^{-1})$^{1/n}$]	3.136±0.14	3.112±0.12	3.005±0.43	2.567±0.52
	$1/n$	0.212±0.14	0.2236±0.12	0.2641±0.43	0.3254±0.52
	R^2	0.749±0.14	0.7436±0.12	0.7358±0.43	0.7284±0.52
	Δq (%)	8.53±0.14	8.56±0.12	10.07±0.43	12.87±0.52

As can be seen from figures 9 and 10, it is clear that the plots of the Langmuir isotherm model fit well with the experimental data, while the plots of Freundlich isotherm model do not fit. Furthermore, as can be seen from Table 2, while the R^2 values for the Freundlich isotherm model for different temperatures, the weak correlation of the gas-phase toluene adsorption onto char and the Δq values show high standard deviation, the R^2 values of the Langmuir isotherm model are 0.98, and Δq values are less than 3%. This result indicates that the surface energy is homogeneously distributed and that single-plate adsorption occurs [37]. The maximum monolayer adsorption capacity (q_{max}) of the char was calculated as 15.42 mg g^{-1} for 303 K. The n parameter obtained from the Freundlich model is always greater than 1, thus, confirming that the adsorption of the gas-phase toluene onto char is a physical adsorption [38]. However, the reduction of both the Freundlich constants, K_F and n (i.e., the increase of $1/n$), by temperature increase confirms that adsorption is feasible at low temperatures, in other words, low temperatures facilitate the adsorption of the gas-phase toluene onto char [39].

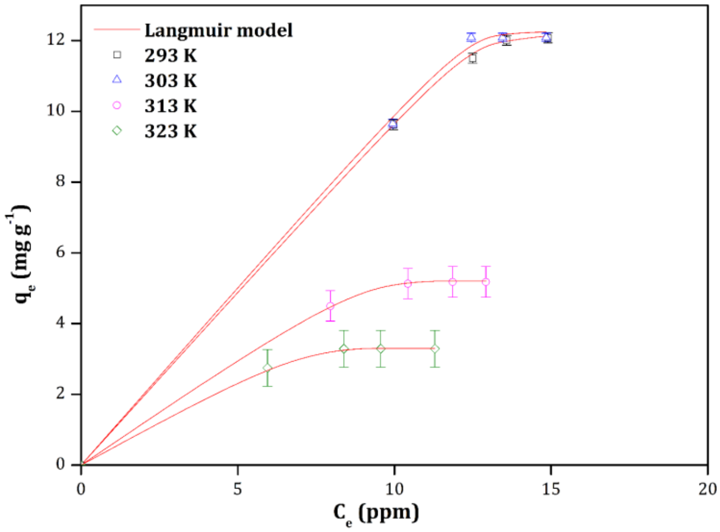

Fig. 9 Adsorption isotherm for the adsorption of gas-phase toluene onto char fitted by Langmuir model at different temperatures

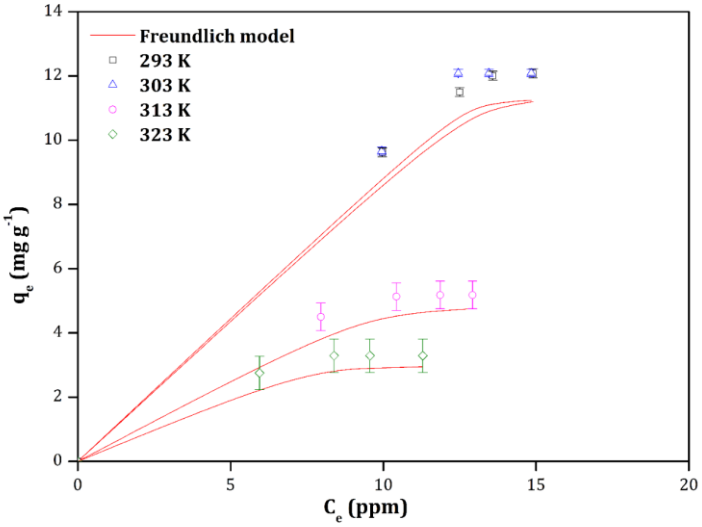

Fig. 10 Adsorption isotherm for the adsorption of gas-phase toluene onto char fitted by Freundlich model at different temperatures

3.8. Adsorption Thermodynamic Studies

The equilibrium state in physical and chemical events in the adsorption process is related to thermodynamics. Whether the adsorption event is an endothermic or exothermic event can be determined in accordance with thermodynamic parameters. Adsorption mechanism can be explained by thermodynamic parameters such as Gibbs free energy change ($\Delta G°$), enthalpy change ($\Delta H°$) and entropy change ($\Delta S°$) [29]. As has been widely reported in the literature [39-41], the thermodynamic laws incorporating experimental data obtained from Langmuir isotherms (the best isotherm model fitted) can be used to determine thermodynamic parameters through the following equations [21]:

$$\Delta G^0 = -RT\ln K_e^{\circ} \tag{8}$$

$$\Delta G^0 = \Delta H^0 - T\Delta S^0 \tag{9}$$

Where, R (8.314 J mol^{-1} K^{-1}) is the universal ideal gas constant and T is the absolute temperature in Kelvin (K). K_e° is the thermodynamic equilibrium constant that is dimensionless. The $\Delta G°$ (kJ mol^{-1}) parameter is calculated directly by Equation 8.

The well-known Van't Hoff equation is obtained by incorporating Equation 8 into Equation 9:

$$\ln K_e^{\circ} = \frac{\Delta S^0}{R} - \frac{\Delta H^0}{R}\frac{1}{T} \tag{10}$$

The $\Delta H°$ (kJ mol^{-1}) and $\Delta S°$ (kJ mol^{-1} K^{-1}) parameters are calculated from the slope and intercept of the plot of $\ln K_e^{\circ}$ against $1/T$, respectively.

In order to determine the thermodynamic parameters, experiments were carried out at four different temperatures: 293, 303, 313 and 323 K. The $\Delta G°$ parameter was calculated directly using Equation 8. The $\Delta H°$ and $\Delta S°$ parameters were determined from the slope and the intercept of the linear plots in Figure 11, respectively. The data of $\ln K_e^{\circ}$ versus $1/T$ were plotted and are shown in Figure 11. The calculated Gibbs Free Energy ($\Delta G°$), enthalpy change ($\Delta H°$) and entropy change ($\Delta S°$) values are presented in Table 3. In Table 3, the negative sign of $\Delta G°$ indicates that the adsorption process was appropriate and spontaneous [42]. The $\Delta G°$ values between -20 kJ mol^{-1} and 0 kJ mol^{-1} were reduced to the physical adsorption range [43]. This result shows that physical adsorption was the dominant mechanism for the adsorption of the gas-phase toluene onto char. The $\Delta H°$ value for the adsorption process was calculated as -17.18 kJ mol^{-1}. The negative value of the calculated $\Delta H°$ indicates that the adsorption process was exothermic. Furthermore, the magnitude of $\Delta H°$ (<20 kJ mol^{-1}) indicates that physical adsorption was predominant [39]. The negative value of $\Delta S°$ indicates that the entropy of the system decreased. This means that the disorder of the system during the adsorption process and the randomization of the adsorbate at the solid/gas interface were reduced [30]. his is because, the gas-phase toluene molecules pass from a random step to a regular step (on the surface of the adsorbent).

Table 3. Thermodynamics parameters for the adsorption of gas-phase toluene onto char

T (K)	$\Delta G°$ (kJ mol^{-1})	$\Delta H°$ (kJ mol^{-1})	$\Delta S°$ (kJ mol^{-1} K^{-1})
293	-6.936±0.14	-17.181	-0.025
303	-7.927±0.12		
313	-8.651±0.43		
323	-9.489±0.52		

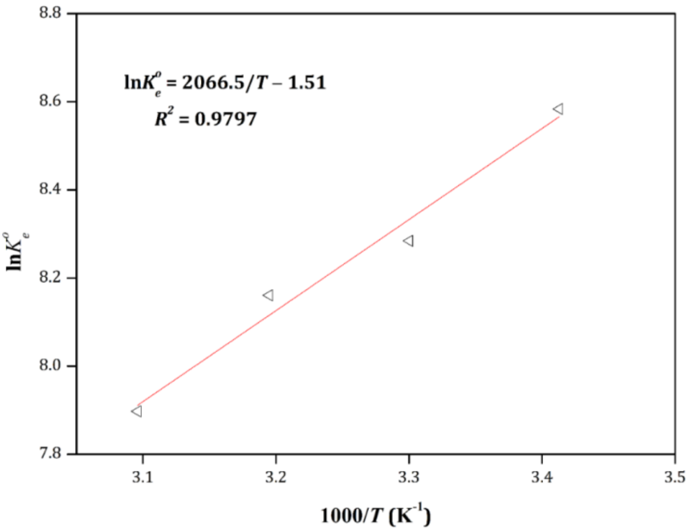

Fig. 11 Plots of $\ln K_e^{\circ}$ versus $1/T$ for the estimation of thermodynamic parameters

4. Conclusions

Toluene is a VOC which is abundantly found in the environment. Toluene is the primary material used in chemical process industries and is often used as a raw material in the production of many chemicals and as a solvent in many engineering processes. The material of char, which is used as an adsorbent, is produced from almond shells. Almond shells, which are abundant and low-cost residues, are suitable to be used as a raw material for the preparation of char. In this study, the adsorption of gas-phase toluene onto char was studied in a dynamic system by using a laboratory-scale fixed-bed reactor under atmospheric pressure. Adsorption parameters such as N_2 flow rate as the gas-phase toluene carrier, char amount, gas-phase toluene concentration at the inlet, and adsorption temperature play an important role in both the adsorption capacity and adsorption efficiency of the gas-phase toluene onto char.

Experimental results showed that the adsorption capacity decreased with increasing temperatures and the amount of char while it increased with the gas flow rate and the concentration of the gas-phase toluene at the inlet. In addition, results of gas flow rate of 100 mL min^{-1}, char amount of 0.50 g, concentration of gas-phase toluene at the inlet of 12.50 ppm, and temperature of 303 K showed good reproducibility. Adsorption kinetics data were analyzed using pseudo-first-order and pseudo-second-order models. The adsorption of the gas-phase toluene onto char can be well represented by the pseudo-second-order kinetic model. Equilibrium isotherm data were analyzed by the Langmuir and Freundlich isotherm models and the results indicated that the adsorption process was described well by the Langmuir isotherm model. The maximum monolayer adsorption capacity (q_{max}) of the char was determined as 15.42 mg g^{-1} for 303 K. Thermodynamic parameters such as $\Delta G° = -7.93$ kJ mol^{-1}, $\Delta H° = -17.18$ kJ mol^{-1}, $\Delta S° = -0.013$ kJ mol^{-1} K^{-1} showed that the adsorption process of the gas-phase toluene onto char was spontaneous, exothermic and physical. The results showed that the material of the char produced from almond shells could be used as a biosorbent to remove the material of the gas-phase toluene from various industrial and natural sources through the adsorption method.

References

[1] Koppmann R. Volatile Organic Compounds in the Atmopshere. UK.: Blackwell Publishing Ltd.; 2007. https://doi.org/10.1002/9780470988657

[2] Ghoshal AK, Manjare SD. Selection of appropriate adsorption technique for recovery of VOCs: an analysis. Journal of Loss Prevention in the Process Industries. 2002;15(6):413-421. https://doi.org/10.1016/S0950-4230(02)00042-6

[3] Khan FI, Kr. Ghoshal A. Removal of Volatile Organic Compounds from polluted air. Journal of Loss Prevention in the Process Industries. 2000;13(6):527-545. https://doi.org/10.1016/S0950-4230(00)00007-3

[4] Pires J, Carvalho A, de Carvalho MB. Adsorption of volatile organic compounds in Y zeolites and pillared clays. Microporous and Mesoporous Materials. 2001;43(3):277-287. https://doi.org/10.1016/S1387-1811(01)00207-4

[5] Srivastava NC, Eames IW. A review of adsorbents and adsorbates in solid–vapour adsorption heat pump systems. Applied Thermal Engineering. 1998;18(9):707-714. https://doi.org/10.1016/S1359-4311(97)00106-3

[6] Tsai W-T. A review of environmental hazards and adsorption recovery of cleaning solvent hydrochlorofluorocarbons (HCFCs). Journal of Loss Prevention in the Process Industries. 2002;15(2):147-157. https://doi.org/10.1016/S0950-4230(01)00023-7

[7] Hindarso H, Ismadji S, Wicaksana F, Mudjijati, Indraswati N. Adsorption of Benzene and Toluene from Aqueous Solution onto Granular Activated Carbon. Journal of Chemical & Engineering Data. 2001;46(4):788-791. https://doi.org/10.1021/je000176g

[8] Jones AP. Indoor air quality and health. Atmospheric Environment. 1999;33(28):4535-4564. https://doi.org/10.1016/S1352-2310(99)00272-1

[9] Gupta VK, Verma N. Removal of volatile organic compounds by cryogenic condensation followed by adsorption. Chemical Engineering Science. 2002;57(14):2679-2696. https://doi.org/10.1016/S0009-2509(02)00158-6

[10] Hwang KS, Dae Ki C, Sung Yong G, Sung Yong C. Adsorption and thermal regeneration of methylene chloride vapor on an activated carbon bed. Chemical Engineering Science. 1997;52(7):1111-1123. https://doi.org/10.1016/S0009-2509(96)00470-8

[11] Naidu G, Jeong S, Johir MAH, Fane AG, Kandasamy J, Vigneswaran S. Rubidium extraction from seawater brine by an integrated membrane distillation-selective sorption system. Water Research. 2017;123:321-331. https://doi.org/10.1016/j.watres.2017.06.078

[12] Shahmirzadi MAA, Hosseini SS, Tan NR. Enhancing removal and recovery of magnesium from aqueous solutions by using modified zeolite and bentonite and process optimization. Korean Journal of Chemical Engineering. 2016;33(12):3529-3540. https://doi.org/10.1007/s11814-016-0218-z

[13] Lillo-Ródenas MA, Cazorla-Amorós D, Linares-Solano A. Behaviour of activated carbons with different pore size distributions and surface oxygen groups for benzene and toluene adsorption at low concentrations. Carbon. 2005;43(8):1758-1767. https://doi.org/10.1016/j.carbon.2005.02.023

[14] Roop Chand Bansal, Goyal M. Activated Carbon Adsorption. 1 st ed. Boca Raton: Taylor & Francis Group; 2005. 263-265 p.

[15] Parra MA, Elustondo D, Bermejo R, Santamaría JM. Quantification of indoor and outdoor volatile organic compounds (VOCs) in pubs and cafés in Pamplona, Spain. Atmospheric Environment. 2008;42(27):6647-6654. https://doi.org/10.1016/j.atmosenv.2008.04.026

[16] Ruthven DM. Principles of Adsorption and Adsorption Processes. New York: John Wiley; 1984.

[17] Allen RWK, D Archer E, MacInnes J. Adsorption by Particles Injected into a Gas Stream. Chemical Engineering Journal - CHEM ENG J. 2001;83:165-174. https://doi.org/10.1016/S1385-8947(00)00264-3

[18] Allen RWK, Archer ED, MacInnes JM. Theoretical account of a dry sorption injection experiment. AIChE. 2001;47(12):2684-2695. https://doi.org/10.1002/aic.690471208

[19] Archer ED, Allen RWK, MacInnes JM. Measurements of VOC take-up by adsorbing particles in a gas stream. Filtration & Separation. 2000;37(10):32-39. https://doi.org/10.1016/S0015-1882(00)80250-5

[20] Balathanigaimani MS, Shim W-G, Lee M-J, Lee J-W, Moon H. Adsorption Isotherms of Benzene and Toluene on Corn Grain-Based Carbon Monolith at (303.15, 313.15, and 323.15) K. Journal of Chemical & Engineering Data. 2008;53(3):732-736. https://doi.org/10.1021/je700575g

[21] Kutluay S, Baytar O, Şahin Ö. Equilibrium, kinetic and thermodynamic studies for dynamic adsorption of benzene in gas phase onto activated carbon produced from elaeagnus angustifolia seeds. Journal of Environmental Chemical Engineering. 2019;7(2):102947. https://doi.org/10.1016/j.jece.2019.102947

[22] Hassan AF, Abdel-Mohsen AM, Fouda MMG. Comparative study of calcium alginate, activated carbon, and their composite beads on methylene blue adsorption. Carbohydrate Polymers. 2014; 102:192-198. https://doi.org/10.1016/j.carbpol.2013.10.104

[23] Noorimotlagh Z, Darvishi Cheshmeh Soltani R, Khataee AR, Shahriyar S, Nourmoradi H. Adsorption of a textile dye in aqueous phase using mesoporous activated carbon prepared from Iranian milk vetch. Journal of the Taiwan Institute of Chemical Engineers. 2014;45(4):1783-1791. https://doi.org/10.1016/j.jtice.2014.02.017

[24] Bazrafshan E., Faridi H., M.F. K, A.H. M. Arsenic removal from aqueous environments using moringa peregrina seed extract as a natural coagulant. Asian Journal of Chemistry. 2013;25:3557-3561. https://doi.org/10.14233/ajchem.2013.13647

[25] de Luna MDG, Flores ED, Genuino DAD, Futalan CM, Wan M-W. Adsorption of Eriochrome Black T (EBT) dye using activated carbon prepared from waste rice hulls—Optimization, isotherm and kinetic studies. Journal of the Taiwan Institute of Chemical Engineers. 2013;44(4):646-653. https://doi.org/10.1016/j.jtice.2013.01.010

[26] Hameed BH, El-Khaiary MI. Equilibrium, kinetics and mechanism of malachite green adsorption on activated carbon prepared from bamboo by K2CO3 activation and subsequent gasification with CO2. Journal of Hazardous Materials. 2008;157(2):344-351. https://doi.org/10.1016/j.jhazmat.2007.12.105

[27] Ramirez D, Qi S, Rood MJ, Hay KJ. Equilibrium and Heat of Adsorption for Organic Vapors and Activated Carbons. Environmental Science & Technology. 2005;39(15):5864-5871. https://doi.org/10.1021/es048144r

[28] M. M. Vargas A, L. Cazetta A, Kunita M, L. Silva T, Almeida V. Adsorption of methylene blue on activated carbon produced from flamboyant pods (Delonix regia): Study of adsorption isotherms and kinetic models. Chemical Engineering Journal. 2011;168(2):722-730. https://doi.org/10.1016/j.cej.2011.01.067

[29] Ammendola P, Raganati F, Chirone R. CO2 adsorption on a fine activated carbon in a sound assisted fluidized bed: Thermodynamics and kinetics. Chemical Engineering Journal. 2017;322:302-313. https://doi.org/10.1016/j.cej.2017.04.037

[30] Gürses A, Doğar Ç, Yalçın M, Açıkyıldız M, Bayrak R, Karaca S. The adsorption kinetics of the cationic dye, methylene blue, onto clay. Journal of Hazardous Materials. 2006;131(1):217-228. https://doi.org/10.1016/j.jhazmat.2005.09.03

[31] Sari A, Tuzen M, Citak D, Soylak M. Equilibrium, kinetic and thermodynamic studies of adsorption of Pb(II) from aqueous solution onto Turkish kaolinite clay. Journal of Hazardous Materials. 2007; 149(2):283-291. https://doi.org/10.1016/j.jhazmat.2007.03.078

[32] Dursun AY, Kalayci ÇS. Equilibrium, kinetic and thermodynamic studies on the adsorption of phenol onto chitin. Journal of Hazardous Materials. 2005;123(1):151-157. https://doi.org/10.1016/j.jhazmat.2005.03.034

[33] Magdy YH, Daifullah AAM. Adsorption of a basic dye from aqueous solutions onto sugar-industry-mud in two modes of operations. Waste Management. 1998;18(4):219-226. https://doi.org/10.1016/S0956-053X(98)00022-1

[34] El-Bindary AA, Hussien MA, Diab MA, Eessa AM. Adsorption of Acid Yellow 99 by polyacrylonitrile/activated carbon composite: Kinetics, thermodynamics and isotherm studies. Journal of Molecular Liquids. 2014;197:236-242. https://doi.org/10.1016/j.molliq.2014.05.003

[35] Langmuir I. The adsorption of gases on plane surfaces of glass, mica and platinum. J Am Chem Soc 1918;40:1361–1368. https://doi.org/10.1021/ja02242a004

[36] Freundlich HMF. Over the Adsorption in Solution. The Journal of Physical Chemistry. 1906;57:385-471.

[37] Guo Y, Li Y, Zhu T, Wang J, Ye M. Modeling of dioxin adsorption on activated carbon. Chemical Engineering Journal. 2016;283:1210-1215. https://doi.org/10.1016/j.cej.2015.08.067

[38] A.O D, Olalekan A, Olatunya A, Dada AO. Langmuir, Freundlich, Temkin and Dubinin–Radushkevich Isotherms Studies of Equilibrium Sorption of Zn 2+ Unto Phosphoric Acid Modified Rice Husk. IOSR Journal of Applied Chemistry (IOSR-JAC). 2012;3:38-45. https://doi.org/10.9790/5736-0313845

[39] A.A. Adelodun, J.C. Ngila, D.-G. Kim, Jo YM. Isotherm, Thermodynamic and Kinetic Studies of Selective CO2 Adsorption on Chemically Modified Carbon Surfaces. Aerosol and Air Quality Research. 2016:3312–3329.

[40] Hauchhum L, Mahanta P. Carbon dioxide adsorption on zeolites and activated carbon by pressure swing adsorption in a fixed bed. International Journal of Energy and Environmental Engineering. 2014;5(4):349-356. https://doi.org/10.1007/s40095-014-0131-3

[41] Singh VK, Anil Kumar E. Measurement and analysis of adsorption isotherms of CO2 on activated carbon. Applied Thermal Engineering. 2016;97:77-86. https://doi.org/10.1016/j.applthermaleng.2015.10.052

[42] He J, Hong S, Zhang L, Gan F, Ho Y-S. Equilibrium and Thermodynamic Parameters of Adsorption of Methylene Blue onto Rectorite. Fresenius Environmental Bulletin. 2010;19:2651–2656.

[43] Duranoğlu D, Trochimczuk AW, Beker U. Kinetics and thermodynamics of hexavalent chromium adsorption onto activated carbon derived from acrylonitrile-divinylbenzene copolymer. Chemical Engineering Journal. 2012;187:193-202. https://doi.org/10.1016/j.cej.2012.01.120

Research on Engineering Structures & Materials
journal homepage: http://jresm.org
Research Group

Research Article

Preparation of amorphous silica from a renewable agricultural waste of rice husk ash by calcination method combined with chemical activation

Gizem Tufaner *[,a], Açelya Çalışkan[b], Huriye Banu Yener[c], Şerife Şeref Helvacı[d]

Department of Chemical Engineering, Ege University, İzmir, Turkey

Article Info

Article history:
Received 12 Dec 2018
Revised 12 Mar 2019
Accepted 28 Mar 2019

Keywords:

SiO2;
Calcination;
Rice husk ash;
Alkali hydroxide;
Chemical Activation

Abstract

In the study, silica particles were synthesized from rice husk ash by calcination method in the presence of activating agents. The parameters which are effective in calcination method on structure and morphology of synthesized silica particles, activating agent type (NaOH and KOH), the calcination temperature (500-850°C), the calcination time (1-3 hours) and the weight ratio of activating agent to ash (4:1 and 5:1), were investigated. The crystal structures of the silica particles were determined by XRD, agent structures by FTIR, sizes and shapes by SEM, surface areas and porous structures by N2 adsorption-desorption analysis. Amorphous silica particles were synthesized in all experimental conditions. Optimum weight ratio, calcination temperature and time were determined as 4:1, 750°C and 2 hours, respectively. The activating agent NaOH was found to be more active than KOH in the preparation of silica.

1. Introduction

Silica particles are one of the most preferred and promising metal oxides due to their unique characteristics such as high thermal stability, porous structure, excellent adsorption properties, low cost, environmentally friendly nature, and good optical and electrical properties. Due to their remarkable properties, they have been used in several applications such as refractory material, high performance cement, paint, flame retardant, insecticide, bio-fertilizer, catalyst, adsorbents, drug carriers, food and cosmetics [1]. Silica particles can be synthesized using inorganic (sodium silicate) or organic (tetraethyl orthosilicate-TEOS) precursors. TEOS is commercial raw material whereas sodium silicate can be obtained from agricultural wastes (rice husk, rice straw, corn cobs, and bagasse). The use of agricultural wastes as a renewable resource has attracted interests due to their low cost, abundance and environmental friendliness. In addition, its usage as a raw material for the preparation of advanced materials reduces the environmental problems associated with agricultural wastes. The rice husk/ash is one of the natural silica sources due to its high silica content (83-90 wt%). Rice absorbs the silicic acid of the soil and accumulates around cellulosic parts. Silica particles are generally produced using NH_4F, CO_2, acidic solutions and by calcination of the shell or ash of rice husk treated with activating agents [2]. Depending on the calcination temperature, the silica produced from the rice husk ash (RHA) may be in the form of amorphous, partially crystalline or crystalline forms. Amorphous silica is more preferable because it is more reactive and the

---

*Corresponding author: tufanergizem@gmail.com
[a]orcid.org/0000-0002-0640-5565; [b]orcid.org/0000-0001-7368-1837; [c]orcid.org/0000-0001-8512-5459; [d]orcid.org/0000-0003-2916-3762

DOI: http://dx.doi.org/10.17515/resm2019.79ma1205

crystal silica is carcinogenic [1]. During the calcination of the RHA, the silica forming the majority of the inorganic content remains as the organic content, lignin and hemicellulose, are removed by thermal degradation. Hemicellulose is degraded around 200-260°C, and lignin around 280-360°C [3]. In the presence of activating agents, the calcination method allows the use of less chemicals and a shorter synthesis time.

Many experimental studies have been conducted on silica production by calcination method from rice husk/ash without using any activating agent. Sankar and coworkers [4] produced spherical and agglomerated silica nanoparticles from RHA by calcination method at 700°C for 2 hours. Wang et al. [5] conducted a study where spherical silica particles in amorphous form was obtained from rice husk at 800°C and 0.5 hour. There are also studies regarding to the synthesis of silica particles using alkali carbonates or hydroxides as activating agents. Liu et al [6] prepared activated carbon and silica particles from RHA simultaneously at 900°C using Na_2CO_3 as activating agent. Liu et al [7] used RHA for the preparation of activated carbon and silica at 1000°C using K_2CO_3 as activating agent. Liu et al. [8] synthesized amorphous silica particles from RHA by calcination method using KOH as the activating agent. They determined the optimum calcination conditions as 700°C and 1 hour. The experimental studies and literature surveys have shown that in order to obtain amorphous and spherical silica particles, it is appropriate to calcine rice husk/ash at temperatures below 900°C with alkali chemicals [3-5, 8-10]. Although, there are studies dealing with the synthesis of silica from RHA by calcination method, less literature is available interested in calcination method using activating agent for the control of the particle properties.

In this study, silica particles were synthesized from RHA using calcination method in the presence of two different alkali hydroxides, NaOH and KOH, as activating agents. The activation parameters investigated were the type of the activating agent (NaOH and KOH), the calcination temperature (500, 650, 750 and 850°C), the weight ratio of activating agent to ash (2:1, 3:1, 4:1 and 5:1), and the calcination time (0.5, 1, 2 and 3 hours). The rinsing water was reused in the synthesis of silica particles. Thus, the study covers the use of a renewable agricultural waste of RHA as the silica source, estimation of the optimum activation conditions to synthesize silica particles with the desired properties, and the reuse of rinsing water in the synthesis. In this respect, the study offers environmentally friendly and low-cost production technology.

2. Materials and Methods

2.1. Materials

Rice husk ash (RHA) kindly supplied by Erdoğanlar Food Industry and Business Company was used as a silica source. The company burnt the rice husk at 700°C for 6 hours under atmospheric conditions. The elemental content of RHA was analyzed with an atomic absorption spectrophotometer (AAS, VarianspectrAA-10Plus). It was found that the RHA contains SiO_2, K_2O and CaO in weight percentages of 91.6, 5.65 and 1.39, respectively, and the remaining are the trace amount of other oxides such as Na_2O, MnO, Al_2O_3 and Fe_2O_3. The ash also contains low amount of unburned carbon. KOH and NaOH (Merck, 99 %) were used as activating agents as received without further purification. The conductivity and pH of the double distilled water used during the experiments were 1.1 $\mu S\,cm^{-1}$ and 6, respectively.

2.2. Preparation of Silica Particles

For the synthesis of silica particles, a definite amount of RHA was mixed with aqueous KOH or NaOH solutions and stirred at 550 rpm for 30 minutes. The mixture was then dried at 110°C for 24 hours. Afterwards, the calcination process was performed in an electrical furnace (Protherm PLF130/9) at the predetermined calcination temperatures and time with a heating rate of 10°C/min. Since the calcination was performed at atmospheric conditions, the unburned carbon in the RHA structure was expected to be removed during the calcination. Thus, the products obtained after the calcination contains high amount of silica, potassium or sodium, and trace amounts of other elements (Fe, Ca, Mg, Al and Mn). The products were washed with distilled water nearly 10 times until they were free of these impurities. The purification process was followed by analyzing potassium and sodium ions in the washing waters using AAS. The products purified were dried at 110°C for 24 hours and then characterized. The rinsing water used for the purification of the particles was evaporated. The concentrated aqueous NaOH/KOH solutions obtained after evaporation was reused as activating agents by adjusting its concentration, and the water condensed as rinsing water. The schematic diagram of the synthesis is shown in Fig. 1.

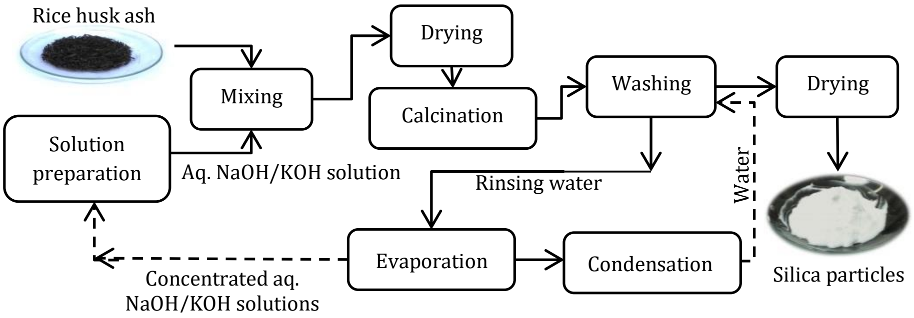

Fig. 1 Schematic representation of silica particle synthesis

2.3. Characterization

The chemical structures of the samples were determined by Fourier transform infrared spectroscopy attached with ATR (ATR-FTIR Perkin Elmer Spectrum 100, Diamond/ZnSe crystal). The crystal structure of the particles was determined by X-ray diffraction (XRD, Philips X'pert PRO–45 kV, 40 mA, 2θ=5-75°CuKα). The surface areas and porosity of the samples were determined by means of N_2 adsorption-desorption isotherms at 77.53 K using a volumetric adsorption system (Micromeritics Instruments Gemini V). The samples were degassed at 300°C for 24 hours prior to measurements to ensure that no gas molecules were adsorbed on the surface and in the pores of the particles. The shape and size of the particles were determined by a field emission gun scanning electron microscope (SEM, FEI QUANTA 250 FEG). Surface charges of the particles produced at optimum conditions were determined by means of the light scattering at different pH values (Malvern Zeta-sizer Nano ZS).

3. Results and Discussions

3.1. Characterization of RHA

The FTIR spectrum of RHA is given in Fig. 2a where the characteristics bands at 1050 and 789 cm^{-1} correspond to the asymmetric and symmetric stretching vibrations of the Si-O-Si bonds, respectively. No peaks belonging to the other components in RHA were detected in the spectrum due to their low amounts in the structure. The calcination of rice husk at 700°C for 6 hours resulted in the partial removal of organic components and at the same time crystallization of silica [11]. Therefore, the XRD spectrum of RHA given in Fig. 2b indicated the characteristic peaks of crystalline silica, cristobalite and tridymite. The peaks at 2θ = 21.99, 28.46, 31.45, 42.68, 47.03 and 48.63° and at 2θ = 20.6 and 36.1 correspond to the cristobalite and tridymite, respectively. The SEM image of RHA (Fig. 2c) reveals low porosity and the heterogeneity in the shape and size of the RHA. The low carbon content in RHA resulted in low porosity and thereby the low surface area. The BET, external and micropore surface areas of RHA were estimated as 11.4, 8.1 and 3.3 m^2/g, respectively. Since the external surface area is greater than the micropore area, it can be said that mesopores are dominating in the RHA structure. The mesopore diameter estimated by BJH method was 10.7 nm.

3.2. Effects of activation parameters on silica particles

The effects of the activating agent (NaOH and KOH), the calcination temperature (500, 650, 750 and 850°C), the weight ratio of activating agent to ash (2:1, 3:1, 4:1 and 5:1), and the calcination time (0.5, 1, 2 and 3 hours) on the structure and morphology of the silica particles synthesized were investigated.

3.2.1 Calcination temperature

The calcination temperatures were selected as 650, 750 and 850°C for NaOH and 500, 750 and 850°C for KOH. For NaOH, a gray-black product was obtained at the end of the calcination time at 500°C, which was thought as an indication of the incomplete carbon removal and silica formation. For the complete removal of the organic compounds in the ash, the temperature should be higher than 500°C which was also determined by the literature research [12]. Thus, the minimum calcination temperature was selected as 650°C for NaOH.

The FTIR spectra of the particles produced using NaOH and KOH at different temperatures are given in Fig. 3. The FTIR spectra was quite similar to that of the RHA given in Fig. 2a. However, the characteristic bands at 1050 and 789 cm^{-1} belonging to the asymmetric and symmetric stretching vibrations of the Si-O-Si bonds shifted towards 974 and 679 cm^{-1}, respectively. The shifts towards the low wavenumbers were due to the inclusion of sodium or potassium ions into the silica structure. In addition, a band at 854 cm^{-1} was assigned to the bending vibrations of the Si-OH. All of these Si bonds showed the formation of the silica structure at all conditions studied. The bands at 1639 and 3372 cm^{-1} correspond to the bending vibrations of the adsorbed and coordinately bound water, respectively.

Although, the RHA consisted of a mixture of cristobalite and tridymite silica (Fig. 2b), the XRD spectra of the particles (Fig. 4) indicated the formation of amorphous silica with the characteristic broad peak between 25 and 30° [4-5, 8, 12]. No significant changes in the XRD spectra of the particles were observed with respect to the calcination temperature and activating agents.

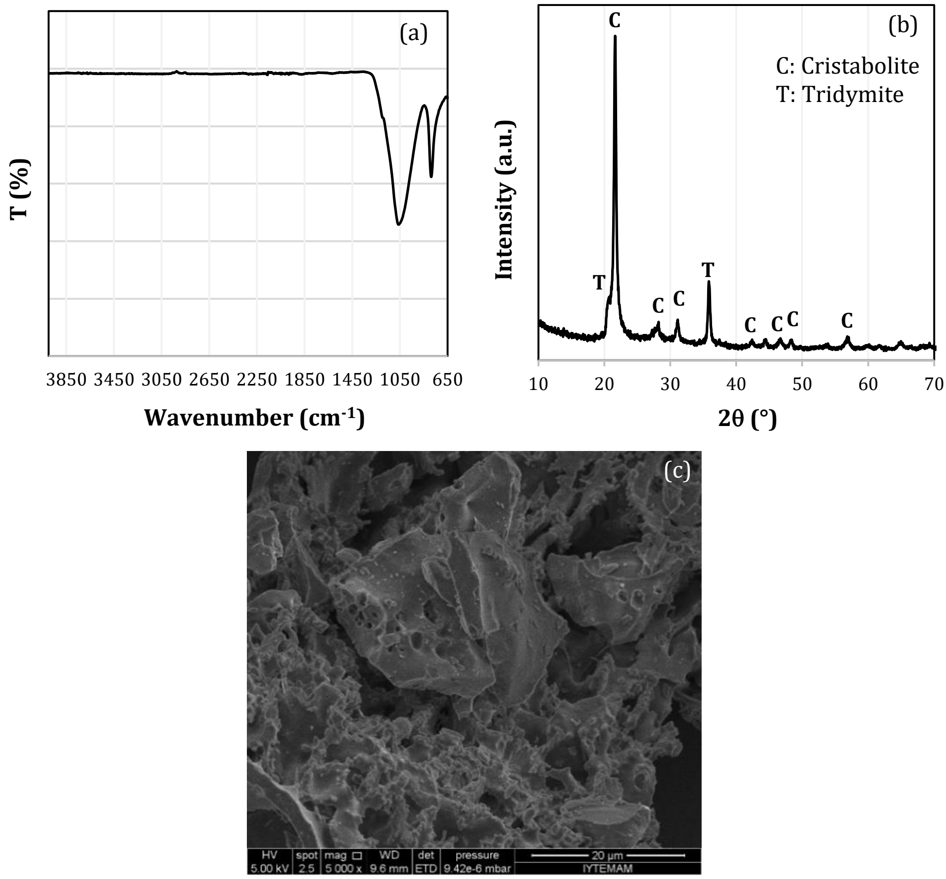

Fig. 2 (a) FTIR, (b) XRD, (c) SEM image of RHA

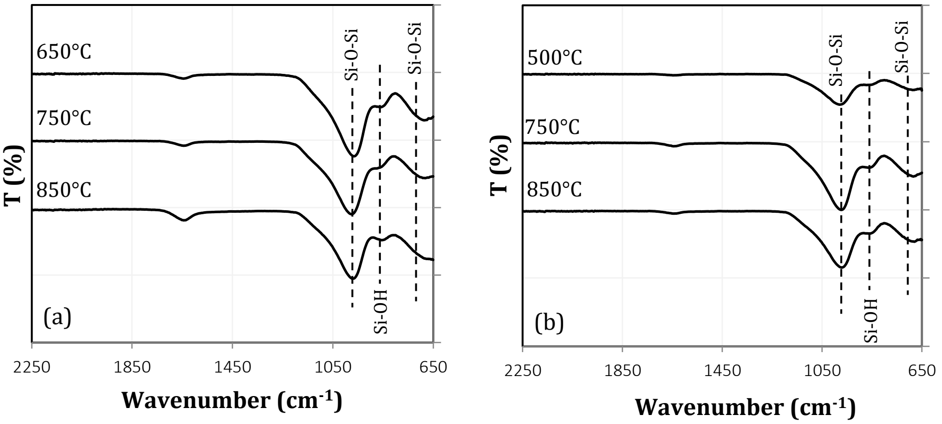

Fig. 3 FTIR spectra of the silica particles in the presence of (a) NaOH and (b) KOH

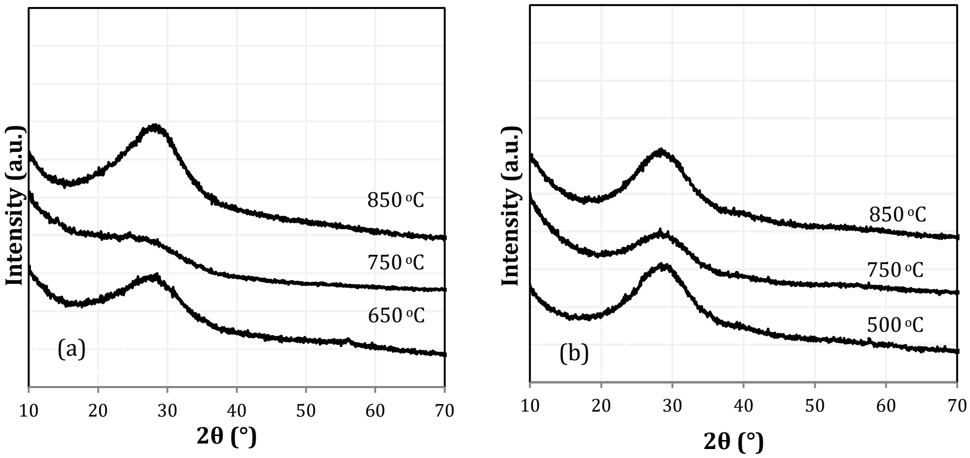

Fig. 4 XRD spectra of the silica particles in the presence of (a) NaOH and (b) KOH

The SEM images given in Fig. 5 (a1-a3 and b1-b3) show the effect of calcination temperature on the shape and size of the particles. For both activating agents, at the lowest temperatures studied, the particles have no clear shapes and have heterogeneous size distribution (Figs. 5-a1 and b1). As the calcination temperature increased from 650 to 750°C for the activating agent of NaOH and from 500 to 750°C for KOH, the shape of the particles became spherical and the size distribution more homogeneous. The size of the particles obtained at 750°C using NaOH (Fig. 5-a2) was found to be smaller than those of KOH (Fig. 5-b2). Further increase in the calcination temperature, from 750 to 850°C increased the agglomeration of the particles with deformation both in their shapes and sizes. The SEM images also show the high porosity of the particles which is different from the RHA's low porosity.

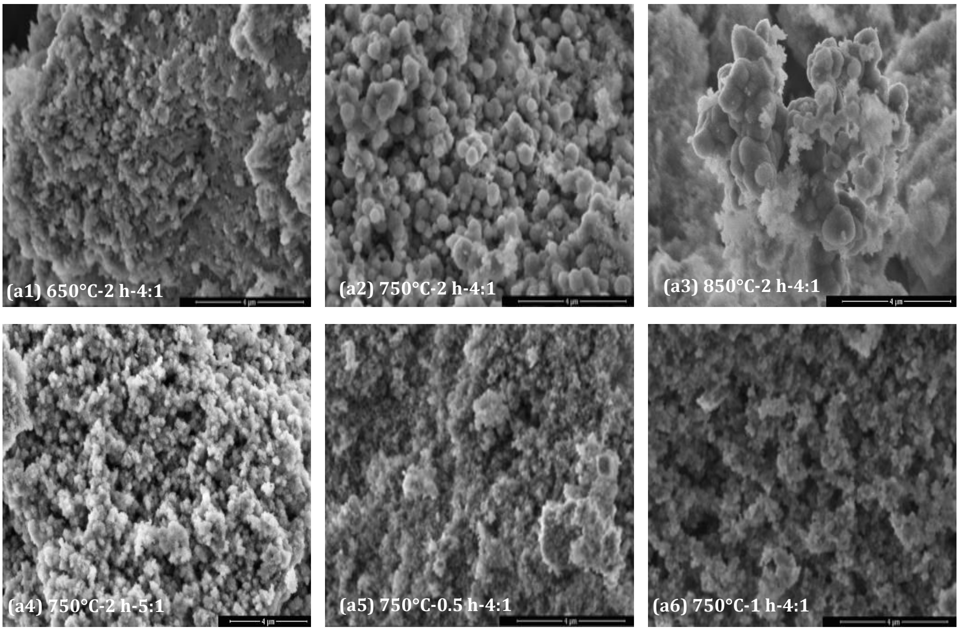

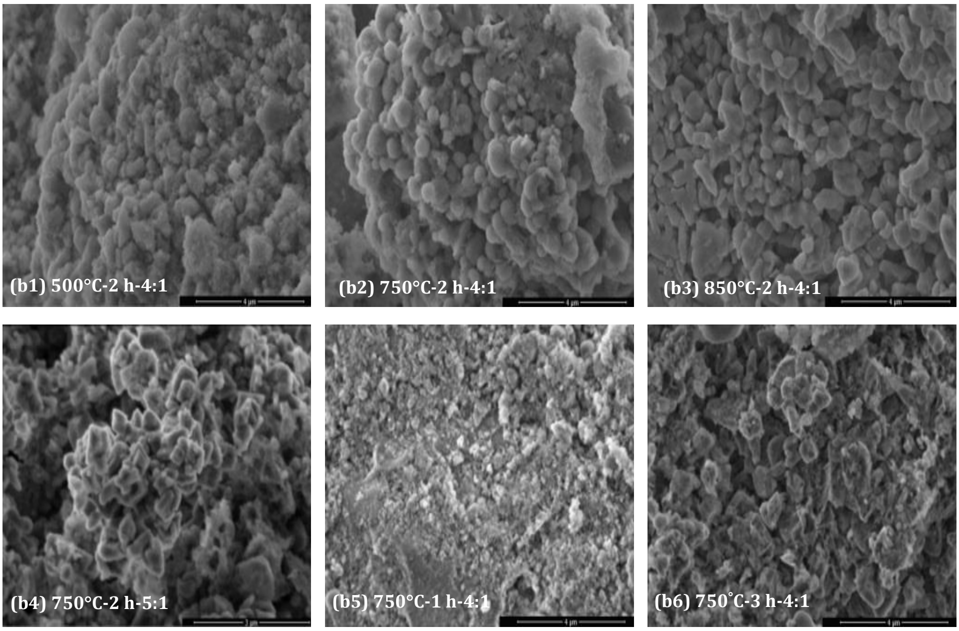

Fig. 5 SEM images of silica particles synthesized using (a) NaOH, (b) KOH

The textural properties of the particles are given in Table 1. Similar to the RHA, all silica particles have mesoporous structures. However, the surface areas of the silica particles (Table 1) were found to be higher than that of the RHA. The penetration of sodium or potassium into the RHA structure at high calcination temperature expanded the matrices in the structure, thereby increased the porosity. As shown in Table 1 for all conditions studied, the external surface areas are greater than the micropore areas indicating the mesoporous structure. It was also supported by the pore sizes changing between 2 and 50 nm. The increase in the calcination temperature speed up the activation reaction increased the consumption of the unburned carbon and so might open the fine and closed pores in the structure. Thus, increased the surface area and decreased the mesopore diameter.

For both activating agents, the most suitable calcination temperature was determined as 750°C. The result obtained was consistent with the studies in the literature [4-5, 8, 10, 12-18] where the optimum temperature was found to be changing between 600 and 800°C. Thus, further parametric studies were performed at the optimum calcination temperature of 750°C.

Table 1 The surface properties of silica particles produced

	Activating Agent					
	NaOH			**KOH**		
Temperature (°C)	**650**	**750**	**850**	**500**	**750**	**850**
BET surface area (m^2/g)	36.33	73.86	78.82	46.95	82.94	94.19
Langmuir surface area (m^2/g)	50.37	101.98	109.13	64.63	114.22	129.75
t-Plot micropore area (m^2/g)	0.64	3.63	2.11	3.70	6.02	6.37
t-Plot external area (m^2/g)	35.69	70.23	76.72	43.25	76.92	87.82
BJH Adsorption diameter (nm)	21.3	16.8	18.8	14.1	8.6	7.7

3.2.2 Weight ratio of activating agent to ash

The effect of the weight ratio of activating agent to ash, 2:1, 3:1, 4:1 and 5:1, were determined at the calcination temperature of 750°C and time of 2 hours. It was observed that the products obtained at the activating agent: ash ratio lower than the 4:1, were gray-black as given in Fig. 6. Since the products with the white color show the formation of silica and complete removal of other organic compounds during the calcination [4, 9, 12, 14, and 17], this gray-black color indicated the unburned organics. In that cases, the amounts of activating agents may be low for the activation reaction, and so silica formation was not completed. Therefore, the particles obtained at low activating agent: ash ratio were not considered as the targeted products, and not characterized. The characterization was performed for the particles obtained at the activating agent: ash ratios of 4:1 and 5:1.

The SEM images of the particles indicated that the increase in the NaOH amount caused the activation reaction to be very fast resulting small sized but highly agglomerated particles (Fig. 5-a4). A similar result was also obtained in case of the KOH, where the increase in the KOH amount caused formation of agglomerated particles with heterogeneous shapes (Fig. 5-b4). Thus, in order to obtain particles with homogeneous shape and size distribution, the activating agent: ash weight ratio of 4:1 is proper at the conditions studied.

Fig. 6 Photographs of the products obtained at different activating agent to ash ratios

3.2.3 Calcination time

The effect of different calcination time on the shape and size of the particles were investigated by keeping the calcination temperature at 750°C and the ratio of the activating agent to ash as 4:1.

The SEM images of the particles obtained using NaOH as the activating agent are given in Figs. 5-a5, a6 and a2 which belong to the calcination time of 0.5, 1 and 2 hours, respectively. It was observed that the calcination time of 0.5 and 1 hours were not long enough for the formation of particles in definite shape. They look like agglomerates of very small spherical particles. However, at the end of 2 hours calcination time, spherical particles with homogeneous size distribution were formed. A similar tendency between the time and particle shape and size was observed in the case of KOH. The calcination time of 1 hour was not enough for the particle formation (Fig. 5-b5), 2 hours resulted in spherical particles with homogeneous size distribution (Fig. 5-b2), and 3 hours heterogeneous particles in both shape and size (Fig. 5-b6). Thus, it can be easily concluded that, the short calcination time was not long enough for the formation of particle and longtime causes the particles to agglomerate. In addition, it is stated in the literature that the existing porosity of the particles has disappeared with increasing time [8]. For these reasons, the most suitable calcination time was determined as 2 hours for both activating agents.

Considering the relation between the activation parameters and the morphological and structural properties of the silica particles synthesized, the optimum activation conditions were found to be activation temperature of 750°C, activating agent to ash weight ratio of 4:1 and activation time of 2 hours for both activating agents. It was found that the activating agent NaOH was more effective in the formation of spherical silica particles and their homogeneous size distributions.

The zeta potentials of the silica particles synthesized at the optimum conditions were measured as a function of the solution pH and given in Fig. 7. The isoelectric points were found to be 2.3 and 2.7 for the particles obtained using NaOH and KOH, respectively. According to the literature, the isoelectric point of the pure silica is 2 [19]. So, the results were found to be consistent with the literature.

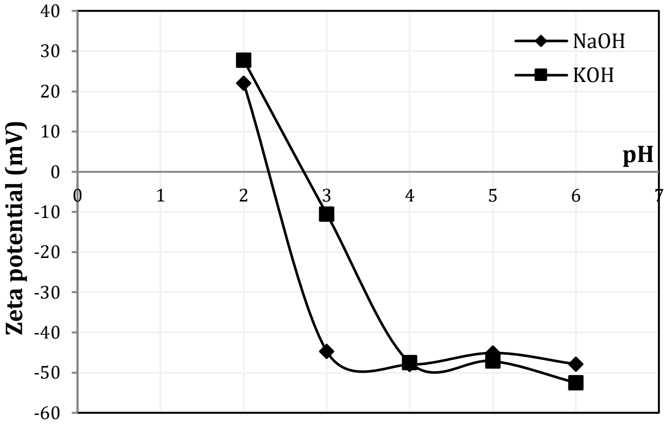

Fig. 7 The zeta potentials of the silica particles with respect to solution pH

4. Conclusion

The present study covers both the optimization of the activation conditions to produce silica particles with the desired properties and the preliminary work for the reduction of the synthesis cost by reusing the rinsing water.

Silica particles were synthesized from RHA by calcination method using alkali hydroxides, NaOH and KOH, as activating agents. The effects of the activation parameters (type of activating agents, calcination temperature, and activating agent to ash weight ratio and calcination time) on the morphological and structural properties of the silica particles were investigated. Although the silica source of RHA is a mixture of cristobalite and tridymite, the silica particles synthesized at all conditions studied were amorphous determined by XRD. For both activating agents, as the calcination temperature increases, the size of the particles increases due to the agglomeration. The increase in temperature speeds up the activation reaction, causing formation of the porous particles. The optimum calcination temperature was found to be 750°C where mesoporous particles with homogeneous size and shape distribution was obtained. A critical activating agent to ash weight ratio, 4:1, was found in the experimental studies. Below this ratio, no pure silica particles were obtained since the organics could not be completely removed at low ratios (2:1 and 3:1). In addition, above the critical ratio, 5:1, due to the fast activation reaction, small sized but highly agglomerated particles were synthesized. For both activating agents, at short calcination time the particles did not have clear shapes, whereas at long time the particles agglomerated causing nonuniform particles. The optimum calcination time was found to be 2 hours both for NaOH and KOH at the conditions studied. Thus, for the synthesis of amorphous, spherical, and homogeneous size distributed particles, the optimum activation conditions were determined as 750°C, 4:1 activating agent to ash weight ratio and 2 hours. Besides, the activating agent NaOH was found to be more effective in the formation of homogeneously distributed spherical particles.

Since the silica particles were amorphous and mesoporous, they have a potential usage as catalyst, adsorbent, or drug carrier in several industrial application fields.

Acknowledgment

The authors thank Prof. Dr. F. S. Ç. Ozkan and specialist Nesrin Tatlıdil (Department of Chemical Engineering, Izmir Institute of Technology) for surface area measurements and Erdoğanlar Food Industry and Business Company for the RHA.

References

[1] Pode RB. Potential applications of rice husk ash waste from rice husk biomass power plant. Renewable and Sustainable Energy Reviews, 2016; 53:1468–1485. https://doi.org/10.1016/j.rser.2015.09.051

[2] Soltani N, Bahrami A, Pech-Canul I, Gonzalez L A. Review on the physicochemical treatments of rice husk for production of advanced materials. Chemical Engineering Journal, 2015; 264:899-935. https://doi.org/10.1016/j.cej.2014.11.056

[3] Carmona VB, Oliveira RM, Silva WTL, Mattoso LHC, Marconcini JM, Nanosilica from rice husk: extraction and characterization. Industrial Crops and Products, 2013; 43:291-296. https://doi.org/10.1016/j.indcrop.2012.06.050

[4] Sankar S, Sharma SK, Kaur N, Lee B, Kim DK, Lee S, Jung H. Biogenerated silica nanoparticles synthesis from sticky red brown rice husk ashes by a chemical method.

Ceramics International, 2016; 42:4875-4885. https://doi.org/10.1016/j.ceramint.2015.11.172

[5] Wang K, Zhao P, Guo X, Li Y, Han D, Chao Y. Enhancement of reactivity in Li4SiO4-based sorbents from the nano-sized rice husk ash for high-temperature CO2 capture. Energy Conversion and Management, 2014; 81:447-454. https://doi.org/10.1016/j.enconman.2014.02.054

[6] Lu Y, Guo Y, Zhu Y, An D, Gao W, Wang Z, Ma Y, Wang Z. A sustainable route for the preparation of activated carbon and silica from rice husk ash. Journal of Hazardous Materials, 2011; 186: 1314-1319. https://doi.org/10.1016/j.jhazmat.2010.12.007

[7] Liu Y, Guo Y, Gao W, Wang Z, Ma Y, Wang Z. Simultaneous preparation of silica and activated carbon from rice husk ash. Journal of Cleaner Production, 2012; 32: 204-209. https://doi.org/10.1016/j.jclepro.2012.03.021

[8] Liu D, Zhang W, Lin H, Li Y, Lu H, Wang Y. A green technology for the preparation of high capacitance rice husk-based activated carbon. Journal of Cleaner Production, 2016; 112:1190-1198. https://doi.org/10.1016/j.jclepro.2015.07.005

[9] Shen Y. Rice husk silica derived nanomaterials for sustainable applications. Renewable and Sustainable Energy Reviews, 2017; 80:453–466. https://doi.org/10.1016/j.rser.2017.05.115

[10] Chen P, Gu W, Fang W, Ji X, Bie R. Removal of metal impurities in rice husk and characterization of rice husk ash under simplified acid pretreatment process. Environmental Progress & Sustainable Energy, 2017; 36: 830-837. https://doi.org/10.1002/ep.12513

[11] Ghasemi Z, Younesi H. Preparation and characterization of nanozeolite NaA from rice husk at room temperature without organic additives. Journal of Nanomaterials, 2011; January: 1-8.

[12] Alshatwi AA, Athinarayanan J, Subbarayan V, Periasamay S. Biocompatibility assessment of rice husk-derived biogenic silica nanoparticles for biomedical applications. Materials Science and Engineering C, 2015; 47:8–16. https://doi.org/10.1016/j.msec.2014.11.005

[13] Chen H, Wang W, Martin JC, Oliphant AJ, Doerr PA, Xu JF, DeBorn K.M, Chen C, Sun L. Extraction of lignocellulose and synthesis of porous silica nanoparticles from rice husks: a comprehensive utilization of rice husk biomass. ACS Sustainable Chemistry and Engineering, 2013; 1: 254-259. https://doi.org/10.1021/sc300115r

[14] Gu S, Zhou J, Luo Z, Wang Q, Ni M. A detailed study of the effects of pyrolysis temperature and feedstock particle size on the preparation of nanosilica from rice husk. Industrial Crops and Products, 2013; 50: 540-549. https://doi.org/10.1016/j.indcrop.2013.08.004

[15] Gu S, Zhuo J, Yu C, Luo Z, Wang Q, Shi Z. A novel two-staged thermal synthesis method of generating nanosilica from rice husk via pre-pyrolysis combined with calcination. Industrial Crops and Products, 2015; 65; 1-6. https://doi.org/10.1016/j.indcrop.2014.11.045

[16] Azadeh M, Zamani C, Ataie A, Morante JR. Three-dimensional rice husk originated mesoporous silicon and its electrical properties. Materials Today Communications, 2018; 14: 141-150. https://doi.org/10.1016/j.mtcomm.2018.01.003

[17] Zhang S, Gao H, Li J, Huang Y, Alsaedi A, Hayat T, Xu X, Wang X. Rice husks as a sustainable silica source for hierarchical flower-likemetal silicate architectures assembled into ultrathin nanosheets foradsorption and catalysis. Journal of Hazardous Materials, 2017; 321: 92-102. https://doi.org/10.1016/j.jhazmat.2016.09.004

[18] Kamari S, Ghorbani F. Synthesis of magMCM-41 with rice husk silica as cadmium sorbent from aqueous solutions: parameters optimization by response surface methodology. Environmental Technology, 2017; 38: 1562-1579. https://doi.org/10.1080/09593330.2016.1237557

[19] Witoon T, Chareonpanich M, Limtrakul J. Effect of acidity on the formation of silica–chitosan hybrid materials and thermal conductive property, Journal of Sol-Gel Science and Technology, 2009; 51: 146-152. https://doi.org/10.1007/s10971-009-1986-2

Research on Engineering Structures & Materials
journal homepage: http://jresm.org
Research Group

Research Article

Production of solid fuel with torrefaction from agricultural wastes

Neslihan Deveci Duranay[a], Nazlı Çaycı[b]

Department of Chemical Engineering, Fırat University, Elazığ, Turkey

Article Info

Article history:
Received 27 Dec 2018
Revised 7 Feb 2019
Accepted 28 Feb 2019

Keywords:

Agricultural waste;
Biomass;
Torrefaction;
Energy yield

Abstract

In this study, it was aimed to produce solid fuel by applying torrefaction process to agricultural wastes, left in the field (usually left to decay) after harvest or post-cultivation period. An eggplant stalk left in the field as an agricultural waste after production period was used in the study. The torrefaction process was applied to the original plant parts cut in certain lengths, and also to the pellets prepared from the same plant. The torrefaction experiments were performed in a pyrex glass reactor placed inside a vertical cylindrical refractory chamber, through which resistance wires are passed. The torrefaction process was performed in N_2 atmosphere at the operation temperatures of 220, 260 and 300°C. The proximate and elemental analyses of the solid product were performed. Besides, the energy yield was determined by measuring the higher heating values (HHV) of the original sample and solid product. Depending on torrefaction temperature ıt was determined a decrease in the solid product yield, an increase in the yields of liquid and gas products. While the volatile matter content of the solid product was decreased, it was found that the rate of fixed carbon increased. It was also determined that elemental carbon ratio increased and oxygen ratio decreased as a result of the torrefaction process. It was detected that the higher heating value of the biomass increased with rising torrefaction temperature and 65.58% of the energy that contained has been maintained at severe (300°C) torrefaction conditions.

1. Introduction

Biomass has recently caught great attention as an energy resource. It is estimated that biomass which is a renewable and carbon neutral energy resource will have a significant role in the energy production in the future. 10% of world total energy consumption and 78% of total renewable energy consist of biomass [1,2]. However, this is lower than expectations considering vast research on biomass energy, oriented to conversion of many varieties of them into substitute fuels for oil and coal. Currently, reducing the effects of global climate change and minimizing environmental consequences of fossil fuel-depended industry, use of renewable sources is still a crucial option for energy supply.

Biomasses can be broadly classified as woody and non-woody types of materials. Woody biomasses are usually obtained from forestry and wood industry while non-woody biomasses are mostly generated from agricultural actions [3]. For most biomasses a generic term of Lignocelluloses are used to refer main plant constituents which form a complex matrix. For example, woody tissues of land plants are composed of cellulose as

---

Corresponding author: nduranay@firat.edu.tr
[a] orcid.org/0000-0001-7259-1864; [b] orcid.org/0000-0003-2700-1639
DOI: http://dx.doi.org/10.17515/resm2019.85en1227

the major component (30-40%) of cell walls, in turn hemicelluloses (25-35%) and lignin (12-30%). These percentages reflect variable compositions of different biomasses. Considering vast types and varieties of plants, lignocelluloses comprise huge variety of materials with distinctive physical and chemical characteristics [4].

Agricultural wastes are one of the important biomass resources; because they are in an excessive amount and their usage in fuel production does not affect the food production. A lot of agricultural wastes are not evaluated and they are accumulated in open areas and cause to air pollution. High moisture content, low heat value, high volume and low bulk density make difficult to use these wastes as fuel. Many biomass improvement (transformation) methods have been developed to decrease these problems. These methods are gasification, pyrolysis, anaerobic decomposition, fermentation and transesterification. Torrefaction process applied for the solid fuel production is also one of these methods [5].

Torrefaction is the low temperature pyrolysis. The main purpose in the torrefaction process is to decrease the humidity of the biomass and increase its heat value. Biomass can be converted into more uniform solids (biochar) by torrefaction [6-8]. During torrefaction of biomasses, majority of hemicelluloses and some fraction of cellulose decompose by dehydration, deoxygenation and dehydrogenation reactions [9]. The contents of low-energy H-C and O-C bonds are decreased, whereas the content of high-energy C-C bond is increased [10,11]. These changes produce a more uniform, reactive, easy to grind and hydrophobic biomass with reduced O/C and H/C ratios and increased energy density [12-14]. The humidity ratio of the biomass to which torrefaction has been applied is very low. For this reason, it is seen that it ignites in a short time [15]. Also, it has been detected that because the volatile compounds are separated, less smoke has occurred and it has burnt in a longer period of time due to the fact that fixed carbon ratio has increased [16].

The parameters effecting biochar yields or mass losses have been studied extensively. Torrefaction temperature was found to be more effective than duration time and woody biomasses gave more amounts of solids compared to agricultural biomasses [17].

The eggplant is a cultigen, grown yearly in warm climates, and is in the shape of a small tree in tropical climates. The eggplant, which is largely consumed in our country, is produced especially in southern regions with hot climate. The aim of the study is providing for especially woody stalks and branches of the eggplant plant, left in the field at the end of the cultivation season, to be converted into a utilizable solid fuel through torrefaction process.

2. Material and Method

Eggplant stalks (ES) used in the study were supplied from Elmapınarı village in the city of Elazig. At the end of the production season, the remaining eggplant plant residues were collected and dried in the laboratory atmosphere. A part of the dried sample was grinded and sieved. Grains in the dimension of <100 mesh was separated for usage in the proximate and ultimate analyses and pellet preparation. ASTM standards (ASTM D-3174 for the ash, ASTM D-3175 for the volatile substance) were used for the proximate analysis of the samples. Proximate analysis was conducted both on the original sample and the samples subjected to the torrefaction process. Tests were repeated for at least three times to check the precision and certainty of the proximate and elemental analysis results and the data showing a deviation higher than ±5 % of the average value were not taken to the scope to ensure the repeatability of the experimental data. Elemental analyses were conducted with LECO (CHNS-932) Elemental Analysis Device. High heat values (HHV) were determined with Julius Peters I Berlin21 adiabatic calorimeter.

Pellet was prepared from grains in the dimension of <0.150 mm using a hydraulic press. For this, 5 tones/cm^2 of pressure was applied to about 1±0.05 g sample for 30 s, accordingly, pellets with 13mm diameter, and 5mm height were obtained. Besides, approximately 3 and 6 cm long bars, similar to each other, were cut from dry sample, and they were used in the torrefaction experiments.

2.1. Torrefaction

Torrefaction experiments were carried out in the system shown in Fig. 1 System consists of a vertical refractor chamber with 45 mm inner and 115 mm outer diameter and 105 mm height and through which resistance wires were placed and a pyrex glass tube reactor with the diameter of 35 mm and length of 150 mm placed inside the chamber. The upper part of the reactor was closed with the pyrex glass cover providing the entrance of the inert gas to the system. The lower part of the reactor was connected to the cooling system. The liquid product collection apparatus used as the cooling system was placed in the ice bath to ensure the collection of the condensable torrefaction steam. Heating of the chamber was made by using a voltage transformer. Temperature control of system was performed with a NiCr thermocouple located so as to touch upper outside surface of the reactor tube.

Before torrefaction of samples, reactor tube and liquid trap were thoroughly cleaned and dried in an oven at 105°C for 2 hours. After loading with stalks of approximately the same size and weighting the reactor and its top cup, it was placed in the chamber and connected to liquid product collection system with a piece of silicone tubing as shown in Fig. 1 Then nitrogen flow (100 ml/min.) was started to pass through the reactor and trap for 5 minutes to remove any oxygen in these spaces. Then chamber was heated to working temperature in 40 minutes and maintained at this temperature for further 10 minutes. This assured all of the apparent volatiles have evolved in this duration. After that, heating was stopped and the system was left to cool under nitrogen flow.

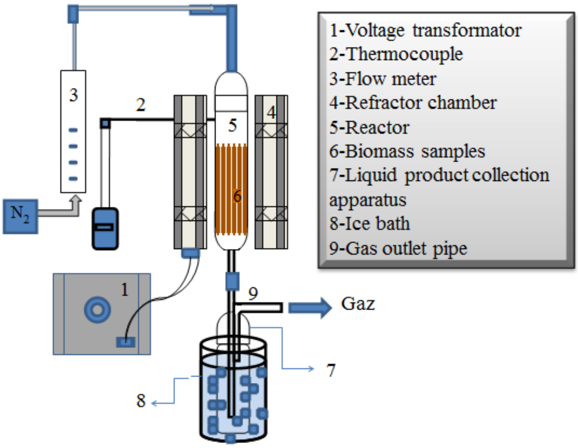

Fig.1 Torrefaction experiment system

The reactor tube with torrefied samples was removed and weighted to estimate solid yield. Liquid traps were also weighted to determine yields and inside contents were transferred into sample tubes. Then traps were rinsed with aliquots of tetrahydrofurane to clean them for the next runs. Gas product yield was estimated from difference. The torrefaction experiments were repeated for 220 (light), 260 (medium), and 300°C (severe). The same processes were applied to prepared pellets at 260°C.

3. Results and Discussion

The colour change in the samples, depending on the temperature of torrefaction is given in Fig. 2. A coal-like view was observed to form as the temperature of torrefaction increased. The increase in weight loss with increasing process temperature is seen in Fig. 3. The high regression coefficient ($R^2 = 0.9875$) indicates a linear relationship between weight loss and the torrefaction temperature. This explains the decrease in solid product yield with increasing temperature, given in Table1. The solid yield was calculated using Eq (1).

$$\text{Solid yield (\%)} = (\text{Weight}_{\text{tor}}/\text{Weight}_{\text{raw}})\times 100 \qquad (1)$$

The subscripts "tor" and "raw" represent torrefied and raw biomass, respectively.

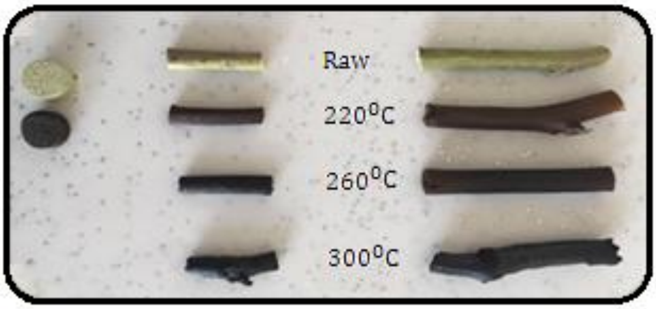

Fig. 2 View of raw and torrefied ES

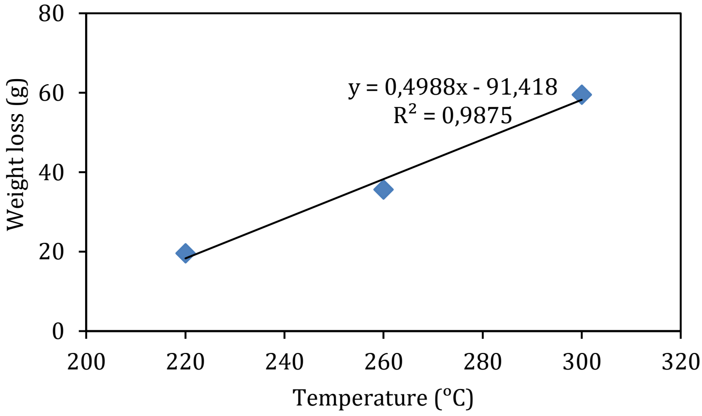

Fig. 3 Change in weight loss of ES with the torrefaction temperature

Table 1. Product yields obtained by the torrefaction of ES at different temperatures

Product	Temperature (°C)	Yield (%) (3 cm)	Yield (%) (6 cm)	Yield (%) (pellet)

Solid	220	80.40	80.38	58.45
	260	64.34	67.02	
	300	40.48	41.50	
Liquid	220	3.35	3.50	13.74
	260	9.82	7.87	
	300	35.81	36.21	
Gas	220	16.26	16.13	27.81
	260	25.84	25.11	
	300	23.71	22.30	

Table1 shows the product yields obtained at three different temperatures for samples of 3 and 6 cm length, respectively. Besides, the torrefaction product yields of the pellet sample at 260 ^{O}C are also given in the same table. It was determined that the amount of liquid and gas products increased as the amount of solid products decreased with rising process temperature. When biomass is heated in an inert environment, the moisture first separates and then begins to decomposition. These components, which form the volatile substance, are separated by the effect of increasing torrefaction temperature and form liquid and gas products. The rising process temperature increases the degradation rate of biomass and causes the amount of solid product to decrease and amounts of liquid and gas products to increase. Therefore, ıt can be said that the solid yield is indicative of the severity of torrefaction. Because, when the torrefaction severity increases, the yield of solid products decreases [18]. On the other hand, it was observed that the stalk length was not effective on the product yields in the reaction zone within the reactor. When the yield of the pelletized sample was compared with that of the stalk samples at the same temperature, it was seen that less solid product and more liquid and gas product were obtained.

The proximate and ultimate analyses result of raw ES and those of the solid product obtained as a result of torrefaction process are given in Table 2. As expected ıt was determined that volatile matter ratio decreased and ash and fixed carbon contents increased with increased torrefaction temperature. The proximate analysis data are also confirmed by elemental analysis data.

Both the product yields and the proximate analysis results show that the pellets prepared from ES behave differently during the torrefaction process. This may be due to the structure of the pellet and the severity of the torrefaction. The structure of the pellet is affected by the moisture content, particle size and lignocellulosic structure of the biomass used [19-22]. Because the pellets were prepared from grains in the dimension of <100 mesh and had a very tight structure. In addition, the most important problem in the development of the torrefaction technology is the predictability and consistency of product quality [23]. It can be said that the temperature and the duration of the torrefaction are not sufficient for the pellet sample.

The elemental analysis results show that carbon content increased as well as oxygen and hydrogen content decreased, with increasing torrefaction temperature. This is because water and low molecular weight components were released from the biomass by devolatilization, with increasing torrefaction temperature. The reduction in hydrogen and oxygen content increases the carbon content [24,25], which leads to improvement in the fuel properties of the solid product. Atomic O/C and H/C ratios in the raw biomass are generally within the interval of respectively 0.4-0.8 and 1.2-2.0. While hydrogen and oxygen from the torrefied biomass are separated by moisture and light volatiles, carbon is retained. This situation causes to the carbonization of the biomass. The Van Krevelen diagram in which the atomic H/C ratio is plotted against the atomic O/C ratio is shown in

Fig. 4. Linear distribution between the two ratios are obviously exhibited in that the regression coefficient of determination (R^2= 0.9669) is high. The two ratios decrease with increasing torrefaction severity [23,26,27]. The slope of the regression line is 1.62, indicating that the impact of torrefaction on the atomic H/C ratio is larger than on the atomic O/C one by a factor of approximately 1.6. The atomic O/C and H/C ratios of the raw sample were found to be 0.98 and 1.91, respectively. In the Van Krevelen diagram, it was determined that ES has approached to the area of cellulose. In this case, it can be said that the ES has high cellulose ratio. It has been observed that O/C and H/C ratios of torrefied ES have been into the interval of 0.4-0.7 and 1.0-1.6 respectively. It was determined that the ratio of lignin in the sample increased with increasing process temperature. The clear change in the ratios of H/C and O/C as a result of the torrefaction process conducted at 300°C in the nitrogen atmosphere is caused by the disintegration of cellulose in this temperature zone [16]. In the Van Krevelen diagram, it has been detected that torrefied samples have approached to the area where peat and lignin were present.

Table 2. The Proximate and ultimate analysis of raw and torrefied samples (* determined from difference)

		Torrefied			
	Raw	**220°C**	**260°C**	**300°C**	**Pellet (260°C)**
Proximate analysis (%)					
Volatile matter	77.00	72.00	60.10	41.70	58.20
Ash	6.10	4.20	6.10	9.70	12.40
Fixed carbon *	16.90	23.80	33.80	48.60	29.40
Ultimate analysis (%)					
C	40.20	47.50	53.80	62.40	
H	6.40	6.54	5.62	5.06	
N	0.40	0.50	0.30	0.70	
S	0.11	0.04	-	0.08	
O*	52.89	45.42	40.28	31.76	

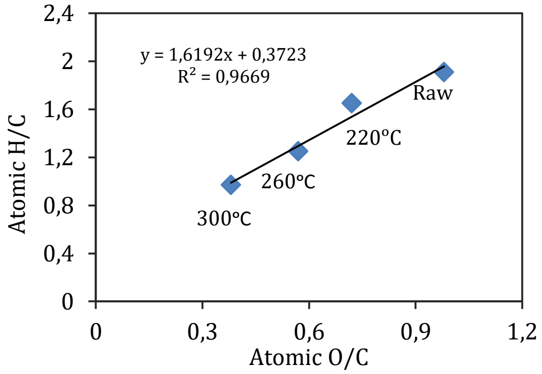

Fig. 4 Change of the atomic H/C and O/C ratios of the raw and torrefied WVS (Van Krevelen diagram)

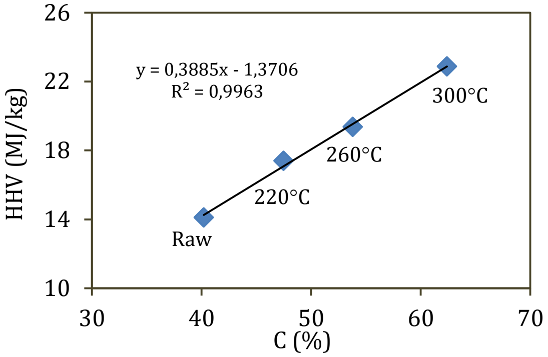

Fig. 5 Change of carbon ratio and HHV of raw and torrefied ES

Fig. 5 shows that HHV increases with the increasing carbon ratio. It is seen that there is a strong linear relationship between HHV and carbon ratio (R^2=0.9963). The hydrogen and oxygen content decreasing together with the increasing carbon in the biomass causes the HHV to increase. The carbon contained by the fuel is the main resource of the heat occurring during the combustion. Hydrogen is also one of the main resources of the combustion heat. However, the excessive hydrogen in the fuel reduces the carbon ratio. The oxygen in the biomass helps the combustion of the fuel, but decreases the heat value of the biomass [16, 28]. This result clearly indicates that the HHV of torrefied biomass can be predicted from the carbon ratio.

Table 3. The effect of process temperature on HHV and energy yield

Sample	**Solid Yield (%)**	**HHV (MJ/kg)**	**Enhancement factor of HHV**	**Energy Yield (%)**
Raw		14.10		
220°C	80.40	17.46	1.24	99.70
260°C	64.34	19.37	1.37	88.15
300°C	40.48	22.87	1.62	65.58
Pellet (260°C)	58.45	17.14	1.22	71.31

Table 3 shows the effect of the process temperature on HHV and energy yield. It was detected that with the increasing temperature, the HHV increased and the energy yield decreased. While the carbon content of the biomass increases as the torrefaction temperature rises, oxygen content decreases [5]. This situation causes to the increase in HHV as the torrefaction temperature increases. It was determined that the HHV increased by 62% when the carbon amount increased by 55% in the torrefaction conducted at 300°C. It was also observed that the energy yield has decreased to 65.58% with the increasing torrefaction temperature. Energy yield can be considered as an important indicator of the amount of energy retained after torrefaction [29]. The energy yield, determined on the basis of solid product yield and HHV, is an indicator of the amount of energy preserved during torrefaction [3]. The energy yield was calculated using Equation 2 and 3 [30]. Taking into account Equation 3, the energy yield is largely dependent on the mass yield values, and it can also be concluded that the energy yield depends on the biomass type [31-33].

$$\text{Enhancement factor of HHV} = HHV_{tor} / HHV_{raw} \quad (2)$$

$$\text{Energy yield \%} = \text{solid yield \%} \times \text{Enhancement factor of HHV} \quad (3)$$

Here; HHV_{tor} and HHV_{raw} respectively show the higher heat values of the torrefied and raw biomass.

The HHV of coal often ranges between 25-35 MJ/kg. It is stated in the literature that the heating value of biomass approximates that of coal as the temperature of torrefaction process increases [12]. It was determined that 65.6% of the energy of the torrefied ES (300°C) was maintained and its HHV approximated that of coal. In the light of these information, this temperature can be said to be appropriate for ES torrefaction process to be performed.

4. Conclusion

The results obtained from this study, in which agriculture waste is aimed to be converted to a usable solid fuel by torrefaction process, are given below:

It was determined that the weight loss of the sample increased and the solid product yield decreased with the increased treatment temperature. In this case, it can be said that the yield of solid products is indicative of the torrefaction severity.

It was observed that the stalk length was not effective on the product yields. Also the high mass loss at 300°C indicated that the eggplant stalks have a high cellulose ratio.

It was concluded that the pellets treated at 260°C behaved differently from the raw sample and the torrefaction severity was not sufficient for the pellets.

It was determined that the ratio C of the solid product increased with the torrefaction severity, the H and O ratios decreased. As a result, O/C and H/C ratios decreased. The net change in H/C and O/C ratios of torrefied ES was detected in 300°C and fuel properties of biomass approached coal.

The energy efficiency decreased and HHV increased with increasing torrefaction severity. It was found that 65.58% of the energy of the biomass was maintained under severe torrefaction conditions. The energy yield is largely dependent on the mass yield values and it can also be said that the energy yield depends on the biomass type. Also ıt was determined that the HHV increased by 62% when the carbon amount increased by 55% in the torrefaction process conducted at 300°C.

It was found that as in many agricultural wastes left to decay at the end of the production season, the fuel properties of eggplant stalks, left to decay, can be improved through torrefaction process. It was determined that the fuel properties of solid product obtained in severe torrefaction conditions (300^{O}C) approximated those of peat. Consequently, it can be said that the solid product obtained from agriculture waste after severe torrefaction conditions can be burned alone or together with coal.

References

[1] Satpathy SK, Tabil LG, Meda V, Naik SN, Prasad R. Torrefaction of wheat and barley straw after microwave heating. Fuel, 2014;124: 269–278. https://doi.org/10.1016/j.fuel.2014.01.102

[2] Bach QV, Skreiberg Ø. Upgrading biomass fuels via wet torrefaction: A review and comparison with dry torrefaction. Renewable and Sustainable Energy Reviews, 2016; 54: 665–677. https://doi.org/10.1016/j.rser.2015.10.014

[3] Chew JJ, Doshi V. Recent advances in biomass pretreatment – Torrefaction fundamentals and technology. Renewable and Sustainable Energy Reviews, 2011; 15: 4212–4222. https://doi.org/10.1016/j.rser.2011.09.017

[4] Prins JM, Ptasinski JK, Janssen FJJG, Krzysztof J. Torrefaction of wood Part 1. Weight loss kinetics. Journal of Analytical and Applied Pyrolysis, 2006; 77:28–34. https://doi.org/10.1016/j.jaap.2006.01.002

[5] Chen W H, Kuo P C. Torrefaction and co-torrefaction characterization of hemicellulose, cellulose and lignin as well as torrefaction of some basic constituents in biomass. Energy, 2011; 36: 803–811. https://doi.org/10.1016/j.energy.2010.12.036

[6] Chen WH, Peng JH, Bi XT,. A state-of-the-art review of biomass torrefaction, densification and applications. Renewable and Sustainable Energy Reviews. 2015; 44: 847–866. https://doi.org/10.1016/j.rser.2014.12.039

[7] Chen WH, Kuo PC. A study on torrefaction of various biomass materials and its impact on lignocellulosic structure simulated by a thermogravimetry. Energy, 2010; 35: 2580–2586. https://doi.org/10.1016/j.energy.2010.02.054

[8] Uslu A, Faaij A, Bergman PCA. Pre-treatment technologies, and their effect on international bioenergy supply chain logistics: Techno-economic evaluation of torrefaction, fast pyrolysis, and pelletisation. Energy, 2008; 33(8): 1206–1223. https://doi.org/10.1016/j.energy.2008.03.007

[9] Chen WH, Zhuang YQ, Liu SH, Juang TT, Tsai CM. Product characteristics from the torrefaction of oil palm fiber hydrothermalcarbonization pelletsin inert and oxidative atmospheres. Bioresource Technology, 2016;199:367–374. https://doi.org/10.1016/j.biortech.2015.08.066

[10] Liu Z, Quek A, Hoekman SK, Balasubramanian B. Production of solid biochar fuel from waste biomass by. Fuel, 2013; 103: 943–949. https://doi.org/10.1016/j.fuel.2012.07.069

[11] Li MF, Li X, Bian J, Xu JK, Yang S, Sun RC. Influence of temperature on bamboo torrefaction under carbon dioxide atmosphere. Industrial Crops and Products, 2015; 76: 149–157. https://doi.org/10.1016/j.indcrop.2015.04.060

[12] Rousset P, Macedo L, Commandré JM, Moreira A. Biomass torrefaction under different oxygen concentrations and its effect on the composition of the solid by-product. Journal of Analytical and Applied Pyrolysis, 2012; 96: 86–91. https://doi.org/10.1016/j.jaap.2012.03.009

[13] Chen WH, Ye SC, Sheng HK. Hydrothermal carbonization of sugarcane bagasse via wet torrefaction in association with microwave heating. Bioresource Technology, 2012; 118: 195–203. https://doi.org/10.1016/j.biortech.2012.04.101

[14] Dudyn´ ski M, van Dyk JC, Kwiatkowski K, Sosnowska M. Biomass gasification: influence of torrefaction on syngas production and tar formation. Fuel Processing Technology, 2015; 131: 203–212. https://doi.org/10.1016/j.fuproc.2014.11.018

[15] Bridgeman TG, Jones JM, Shield I, Williams PT. Torrefaction of reed canary grass, wheat straw and willow to enhance solid fuel qualities and combustion properties. Fuel, 2008 87: 844–856. https://doi.org/10.1016/j.fuel.2007.05.041

[16] Chen D, Zheng Z, Fu K, Zen Z, Wang J, Lu M. Torrefaction of biomass stalk and its effect on the yield and quality of pyrolysis products. Fuel, 2015; 159: 27-32. https://doi.org/10.1016/j.fuel.2015.06.078

[17] Pimchuai A, Animesh Dutta A, Basu P. Torrefaction of Agriculture Residue To Enhance Combustible Properties. Energy Fuels, 2010; 24: 4638–4645. https://doi.org/10.1021/ef901168f

[18] Chen Y-C, Chen W-H, Lin B-J, Chang J-S, Ong HC. Fuel property variation of biomass undergoing torrefaction, Energy Procedia, 2017; 105: 108 – 112. https://doi.org/10.1016/j.egypro.2017.03.287

[19] Kaliyan N, Morey VR. Factors affecting strength and durability of densified biomass products. Biomass Bioenergy, 2009; 33: 337–359. https://doi.org/10.1016/j.biombioe.2008.08.005

[20] Stelte W, Holm JK, Sanadi AR, Barsberg S, Ahrenfeldt J, Henriksen UB. Fuel pellets from biomass: the importance of the pelletizing pressure and its dependency on the

processing conditions. Fuel, 2011; 90: 3285–3290. https://doi.org/10.1016/j.fuel.2011.05.011

[21] Castellano JM, Gomez M, Fernandez M, Esteban LS, Carrasco JE. Study on the effects of raw materials composition and pelletization conditions on the quality and properties of pellets obtained from different woody and non woody biomasses. Fuel, 2015; 139: 629–636. https://doi.org/10.1016/j.fuel.2014.09.033

[22] Pradhana P, Mahajanib SM, Aroraa A. Production and utilization of fuel pellets from biomass: A review. Fuel Processing Technology, 2018; 181: 215–232. https://doi.org/10.1016/j.fuproc.2018.09.021

[23] Rudolfsson M, Stelte W, Lestander T A. Process optimization of combined biomass torrefaction and pelletization for fuel pellet production – A parametric study. Applied Energy, 2015; 140: 378–384. https://doi.org/10.1016/j.apenergy.2014.11.041

[24] Ibrahim RHH, Darvell LI, Jones JM, Williams A. Physicochemical characterisation of torrefied biomass. Journal of Analytical and Applied Pyrolysis, 2013; 103: 21–30. https://doi.org/10.1016/j.jaap.2012.10.004

[25] Gong C, Huang J, Feng C, Wanga G, Tabil L, Wang D, Effects and mechanism of ball milling on torrefaction of pine sawdust. Bioresource Technology, 2016; 214: 242-247. https://doi.org/10.1016/j.biortech.2016.04.062

[26] Van der Stelt MJC, Gerhauser H, Kiel JHA, Ptasinski KJ. Biomass upgrading by torrefaction for the production of biofuels: a review. Biomass Bioenergy 2011;35(9): 3748–62. https://doi.org/10.1016/j.biombioe.2011.06.023

[27] Lestander TA, Rudolfsson M, Pommer L, Nordin A. NIR provides excellent predictions of properties of biocoal from torrefaction and pyrolysis of biomass. Green Chemistry, 2014; 16(12): 4906–13. https://doi.org/10.1039/C3GC42479K

[28] Wu KT, Tsai CJ, Chen CS, Chen HW. The characteristics of torrefied microalgae. Applied Energy, 2012; 100: 52–57. https://doi.org/10.1016/j.apenergy.2012.03.002

[29] Wannapeera J, Fungtammasan B, Worasuwannarak N. Effects of temperature and holding time during torrefaction on the pyrolysis behaviors of woody biomass. Journal of Analytical and Applied Pyrolysis, 2011; 92: 99–105. https://doi.org/10.1016/j.jaap.2011.04.010

[30] Rousset P, Aguiar C, Labbe N, Commandre JM. Enhancing the combustible properties of bamboo by torrefaction. Bioresource Technology, 2011; 102: 8225–8231. https://doi.org/10.1016/j.biortech.2011.05.093

[31] Uemura Y, Omar WN, Tsutsui T, Yusup SB. Torrefaction of oil palm wastes. Fuel, 2011; 90: 2585–2591. https://doi.org/10.1016/j.fuel.2011.03.021

[32] Kim Y-H, Lee S-M,. Lee H-W, Lee J-W. Physical and chemical characteristics of products from the torrefaction of yellow poplar (Liriodendron tulipifera). Bioresource Technology, 2012; 116: 120–125. https://doi.org/10.1016/j.biortech.2012.04.033

[33] Matali S, Rahman NA,. Idris SS, Yaacob N, Alias AB. Lignocellulosic Biomass solid Fuel Properties Enhancement via Torrefaction. Procedia Engineering, 2016; 148: 671 – 678. https://doi.org/10.1016/j.proeng.2016.06.550

Research on Engineering Structures & Materials
journal homepage: http://jresm.org
Research Group

Research Article & Data Set

An acceleration record set for different frequency content, amplitude and site classes

Hayri Baytan Ozmen*[1,a], Hakan Yilmaz[2,b], Hakan Yildiz[2,c]

[1]*Department of Civil Engineering, Usak University, Usak, Turkey.*
[2]*Civil Engineering Division, Graduate School of Natural and Applied Sciences, Usak University, Usak, Turkey.*

Article Info

Article history:
Received 9 Feb 2019
Revised 20 Mar 2019
Accepted 29 Mar 2019

Keywords:

Earthquake properties;
data set;
ground motion record;
record scaling;
shear velocity;
site classification.

Abstract

Dynamic analyses are important tools for seismic evaluation of structures in which the features of the used ground motion records have a key role. For proper estimation, the record set should have the desired extent and variability. However, when present literature is examined, it may be seen that difficulties still exist to have a record set with preferred properties. To ease these difficulties, a study conducted in scope of a project supported by The Scientific and Technological Research Council of Turkey (TUBITAK) under the title of "Change of Earthquake Ground Motions Depending on Soil Properties" and grant number 215M357. A set of acceleration records having different frequency content and soil classes based on average top 30 m shear velocity are given. Set includes 8400 records generated from 84 base rock acceleration passing through 100 different soil cases. The set is assumed to provide a wide range of frequency content, amplitude and soil classification option to researchers. Also, properties of devastating earthquakes in Turkey are investigated. Depth-average shear wave velocity relations are given for sand and clay materials. It is observed that; scaling real earthquake records in 0.7-1.3 range does not alter the frequency-amplitude relationship, records with a PGA of more than 0.4g have higher amplification ratios for waves larger than roughly 1.0 s periods when compared to records with smaller PGA.

1. Introduction

Dynamic analyses are important tools for seismic evaluation of structures. In dynamic analyses, the features of the used ground motion records have a key role. One of the main effects that causes alteration in earthquake ground motion properties is the local site features. The earthquake waves at the base rock alters when passing through the different layers of soil during their course to the surface. It is known that the local site conditions can significantly affect the amplitude and frequency content, which are important features of a ground motion [1, 2].

The instrumental measurements in past earthquakes indicate that soil layers affect seismic ground motion both in time and frequency domain. Several examples can be given to these situations. In 1967 Caracas earthquake, resonance, which can be defined as the site and the structure having similar period, is observed. Since the soil stiffness in Caracas region is relatively uniform, it has been claimed that most of the structural damage is caused by the change in the base rock depth [3]. In the Mexican Earthquake of 1985, the soft soil layers 400 km away from the focus, increased the wave amplitudes 5 times more when compared to the stiff soils, and severely damaged the high rise (10-20 floors) buildings [4]. Spectral

---

*Corresponding author: baytan.ozmen@usak.edu.tr
[a]orcid.org/0000-0001-6750-8632; [b]orcid.org/0000-0001-9329-5394; [c]orcid.org/0000-0002-2872-6634

DOI: http://dx.doi.org/10.17515/resm2019.116ea0209ds

accelerations in the 2 s period were found to be 15-20 times greater in these soft clay layers than in the rock [5]. In the 1989 Loma Prieta Earthquake, low-frequency earthquake wave amplifications in some regions with soft clay soil layers are observed to be between 3 and 6 times [6]. When the highest acceleration values observed in Istanbul at approximately equal distance to the fault compared during the 1999 Kocaeli Earthquake, intensity differences reaching 5 times are reported, which is mainly due to local site conditions [7].

Tezcan et al. [8] examined the soil amplification phenomenon in Avcılar (Istanbul) region 120 km west of the Kocaeli Earthquake of 1999 by using Shake program with 8 representative soil profile combinations. In the analyzes, the Izmit record of 1999 Kocaeli Earthquake was used with different modifications. The results of the analysis indicated three peak periods at 0.70, 1.00 and 1.60 sec, with magnification factors ranging from 2.5 to 5. It can be thought that this situation is compatible with the damage observed in the 5-8-storey buildings, whose periods vary between 0.70 and 1.00 s. The damage in Avcılar is suggested to be a consequence of the site amplification in soft soil layers despite the low acceleration in the base rock and distance to the epicenter [8].

Even though the given examples underline the importance of accounting for the local site conditions, there are limited number of acceleration records with desired features and site classes for the use of researchers using dynamic analyses. Problem of finding acceleration records with chosen characteristics is also mentioned in literature [9, 10]. Therefore, this study is conducted to broaden the ground motion records with different frequency content, amplitude and site classes.

In scope of the study, an input acceleration record set is established using real records, records by deconvolution, scaled versions of real records and generating synthetic records with desired properties. Then the input records set is used to determine the output set which is the form of the input records after passing through the defined soil profiles.

2. The soil profiles

Used soil profiles is given in the supplementary spread sheet files attached to the article under "Site Definitions" page. Establishment of soil properties is performed according to the Uniform Building Code [11] and Turkish Building Seismic Code [12]. These codes classify local site conditions according to the average shear wave velocity of top 30 m soil layers (Table 1).

Table 1 Site classification [11, 12]

Site Class	Soil Type	V_{s30} (m/s)
ZA	Hard Rock	V_{s30}>1500
ZB	Rock	760-1500
ZC	Very dense soil/Soft rock	360-760
ZD	Stiff Soil	180-360
ZE	Soft Soil	V_{s30}<180
ZF	Soils requiring site specific evaluation	N/A

When the attached "Site Definitions" page is examined, it may be seen that first 2 sites are the sites that reflects the conditions of the input motion. Therefore, for these sites, the input and output motions are the same. The successive 31 site definitions include soil profiles with 30 or less than 30 m depth as it is the only value accounted by the codes. The properties of soil layers in these sites are established in a parametric manner to examine code defined values. The rest of the considered sites are deeper than 30 m to examine if the top 30 m is enough to define soil behavior adequately. In determination of the properties of soil layers, the study by Beyaz [13] is referred. In the mentioned study, Beyaz, has investigated the soil profiles of the 64 ground motion recording stations in Turkey using borehole geophysics.

In order to have representative soil layer properties under the 30m depth, the borehole results by Beyaz [13] is examined. Average values of the respective soil shear wave velocities are determined as listed in Table 2.

Table 2 Average and standard deviation values of shear wave velocities of soil layers

	Sand V_s (m/s)		Clay V_s (m/s)	
Depth (m)	Average	Standard Dev.	Average	Standard Dev.
5	377.95	105.41	451.33	188.43
15	633.13	137.43	648.63	216.08
25	659.75	120.32	673.80	170.93
35	733.80	186.15	708.33	207.46
45	820.94	171.56	821.00	117.44
55	796.44	176.96	808.56	174.66
65	792.24	166.27	821.07	168.52
75	837.07	136.30	840.43	147.34
85	810.50	177.62	890.56	138.65
95	870.67	129.77	699.00	44.64

After obtaining average value data, it was aimed to establish a relationship between V_s and depth values in order to get the value at a chosen depth. When the graphs for sand and clay material in Fig. 1 is examined, it seems that for depths smaller than 15 m, there is a steep increase. However, after 15 m the increase in shear wave velocity has a much flat nature. Therefore, it was found appropriate to establish separate relations for the region with low depth (5 -15m) and for the region with higher depth (15 - 95 m). Among the attempted relations, best correlation is obtained by linear relations whose equations are given in the figure. High correlation coefficients obtained from the equations indicates strong relation with good accuracy (Fig. 1). Additionally, Table 2 shows that the coefficient of variation is getting smaller with increasing depth.

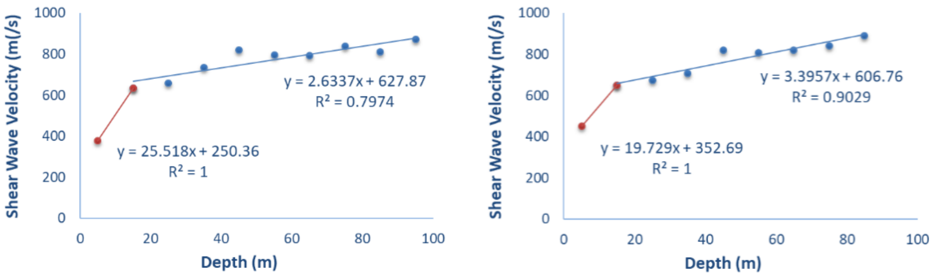

a) sand b) clay

Fig. 1 Average shear wave depth velocity relation for sand and clay

3. Destructive earthquake properties

Before selection of earthquake records the destructive ground motion properties are examined. For a case example, Turkey is selected as an earthquake prone country.

Devastating earthquakes in Turkey between 1903-2011 are investigated. The data is collected from Wikipedia [14], Kandilli Observatory [15] and AFAD [16]. Since the information of these earthquakes was taken from different sources they are checked with the AFAD's [17] database and the parameters of magnitude type, magnitude value and focal depth are obtained in a compatible manner. Fault mechanism information, is taken from "National Strong Motion Data Base of Turkey" which is composed by collaboration of TUBITAK, METU and AFAD. Since some earthquakes have no mechanism data, rake angle values are used to determine the fault mechanism [18]. In spite of all these efforts, fault mechanism information could not be reached for some earthquakes in year 1935 and before. All gathered information is summarized in Table 3.

By the assembled data, certain features of the devastating earthquakes that occurred in Turkey is revealed. The mean depth of focus is 18.61 km. In other words, shallow earthquakes are general destructive earthquake characteristic in Turkey. Earthquakes with a depth of 0-60 km are considered shallow earthquakes. Earthquakes at a depth of 60-300 km are earthquakes with moderate depth. Deep earthquakes are earthquakes with depths of more than 300 km. Most earthquakes occurred in Turkey is in shallow earthquake category. Deep earthquakes are felt in much larger areas, but their damage is inversely proportional to this. However, shallow earthquakes do more damage in a smaller region when compared to deep earthquakes with similar magnitude [15].

When examined in terms of fault mechanisms, there are 22 strike-slip, 7 normal and 3 reverse faults in 32 devastating earthquakes with known fault mechanism information. Strike-slip faults are found to be the dominant mechanism with a 68.75% ratio. It is seen that, with a ratio of 21.88%, normal faults have also an important share in Turkey. However, earthquakes with a reverse fault have a lower ratio of 9.37%.

Table 3 Characteristics of devastating earthquakes in Turkey

Date	Time	Location	Lat.	Long.	Casualty	Mag.	Focal Depth (km)	Fault Mechanism
1903	01:46	Malazgirt, Muş	39.14	42.65	600	6.3 (Ms)	30	
1912	03:29	Mürefte Tekirdağ	40.75	27.20	216	7.4 (Ms)	10	Strike-slip
1914	00:07	Burdur	37.82	30.27	300	7.0 (Ms)	10	
1924	16:34	Horasan, Erzurum	40.00	42.10	60	6.8 (Ms)	10	
1928	02:29	İzmir	38.50	28.00	50	6.2 (Ms)	35	
1929	08:37	Suşehri, Sivas	40.20	37.90	64	6.1 (Ms)	10	
1935	16:41	Erdek, Balıkesir	40.40	27.50	5	6.2 (Ms)	35	
1938	12:59	Kırşehir	39.10	34.00	160	6.6 (Ms)	10	Strike-slip
1939	02:36	Dikili, İzmir	39.10	26.80	60	6.6 (Ms)	10	
1939	23:57	Erzincan	39.77	39.53	32700	7.9 (Ms)	20	Strike-slip
1942	19:01	Bigadiç, Balıkesir	39.20	28.20	16	6.1 (Ms)	10	
1942	14:03	Erbaa, Tokat	40.87	36.47	3000	7.0 (Ms)	10	
1943	17:32	Hendek, Adapazarı	40.60	30.50	336	6.6 (Ms)	10	Strike-slip
1943	22:24	Ladik, Samsun	41.05	33.72	4000	7.2 (Ms)	10	
1944	03:25	Gerede, Bolu	40.80	32.20	3959	7.3 (Ms)	10	Strike-slip
1944	04:34	Ayvalık, Balıkesir	39.37	26.53	30	6.8 (Ms)	40	Normal
1949	20:43	Karlıova, Bingöl	39.54	40.57	450	6.7 (Ms)	40	Strike-slip
1951	18:36	Kurşunlu, Çankırı	40,88	32,87	50	6.9 (Ms)	10	Strike-slip
1953	21:06	Yenice, Çanakkale	40,02	27,53	265	7.2 (Ms)	10	Strike-slip
1955	09:07	Söke, Aydın	37,55	27,05	23	6.8 (Ms)	40	Normal
1957	04:25	Fethiye, Muğla	36,50	28,60	67	7.1 (Ms)	80	Strike-slip

Date	Time	Location	Lat.	Long.	Casualty	Mag.	Focal Depth (km)	Fault Mechanism
1957	06:36	Abant, Bolu	40,67	31,00	52	7.1 (Ms)	10	Strike-slip
1964	16:31	Manyas, Balıkesir	40,10	27,93	23	7.0 (Ms)	34	Normal
1966	12:23	Varto, Muş	39,17	41,56	2396	6.9 (Ms)	26	Reverse
1967	16:56	Mudurnu, Adapazarı	40,67	30,69	89	6.8 (Ms)	33	Strike-slip
1968	10:19	Bartın	41,79	32,31	29	6.5 (Ms)	5	Strike-slip
1969	03:48	Alaşehir, Manisa	38,50	28,40	53	6.5 (Ms)	4	Normal
1970	23:02	Gediz, Kütahya	39,20	29,50	1086	7.2 (Ms)	18	Normal
1971	16:44	Bingöl	38,83	40,52	1000+	6.8 (Ms)	3	Strike-slip
1975	12:20	Lice, Diyarbakır	38,50	40,70	2385	6.6 (Ms)	32	Reverse
1976	14:22	Muradiye, Van	39,12	44,03	3840	7.2 (Mw)	9	Strike-slip
1983	07:12	Erzurum	40,33	42,19	1155	6.6 (Mw)	15	Strike-slip
1992	17,18	Erzincan	39,70	39,69	498	6.6 (Mw)	22	Strike-slip
1995	17:57	Dinar, Afyon	38,06	30,13	90	6.4 (Mw)	31	Normal
1998	16:55	Ceyhan, Adana	36,88	35,31	146	6.3 (Ms)	10	Strike-slip
1999	03:02	İzmit	40,77	30,00	17118	7.5 (Mw)	15	Strike-slip
1999	18:57	Düzce	40,75	31,16	894	7.1 (Mw)	11	Strike-slip
2002	07:11	Sultandağı, Afyon	38,57	31,27	44	6.5 (Mw)	5	Normal
2003	05:26	Pülümür, Tunceli	39,46	39,79	1	6.0 (Mw)	15	Strike-slip
2003	00:27	Bingöl	39,01	40,46	177	6.3 (Mw)	10	Strike-slip
2010	04:32	Karakoçan, Elâzığ	38,87	39,99	41	6,1 (Mw)	5	Strike-slip
2011	01:41	Tabanlı, Van	38,76	43,36	601	7.1 (Mw)	19	Reverse

4. The input ground motion set

In order to have an acceleration record set in consistency with the nature, to have real earthquake records as many as possible is preferred. The acceleration recordings are intended to be selected from the actual earthquakes, recorded on the hard rock in accordance with the bed rock definition. Selecting records with different amplitude and frequency content is aimed to enable comprehensive evaluations.

As many seismic codes use Peak Ground Acceleration (PGA) as the amplitude indicator, it is also used in selection of input ground motions in scope of this study. The acceleration recordings having PGA values between 0 and 0.6 g are selected with 0.05 g increment in each group. In the first 4 groups (0-0.2 g) 8, in the next 4 groups (0.2-0.4 g) 7, in the last (0.4-0.6 g) 4 groups 6 earthquake records are present. The absence of any records with desired features with a PGA of more than 0.6g made it the limiting value.

The intensities of the records are anticipated to be generally amplified by the soil layers during their excursion from base rock to the surface. This situation leads the use of higher number of records with low intensity for the input to have a more uniformly distributed output intensity values.

In order to have records with different frequency content in each 0.05g step, the records are aimed to have different predominant period and Peak Ground Velocity (PGV)/Peak Ground Acceleration (PGA) ratio values. As known, the predominant period is defined as the period of the wave with the largest amplitude in the frequency content. The PGV/PGA ratio has wave period/2π value for a simple harmonic wave [1]. PGV/PGA ratio is known to be an important marker of frequency content and the shape of the acceleration spectrum [19–25].

The establishment of the input acceleration record is done with great care. There are significant limitations and absences in the present natural earthquake records for establishing an acceleration record set with the desired properties which is also the reason of the current study.

For some intervals, if there is not enough number of real earthquake acceleration record with the desired characteristics, alternatives like deconvolution of surface records to base rock form for known soil profiles, scaling some records with scale factors close to unity or generating synthetic records are employed. However, attention has been paid to the characteristics of the synthetic or scaled records to be in accordance with the real earthquake records. In this way, a set of 84 acceleration records with different amplitude and frequency content is established.

4.1. Real earthquake records

Since the selections made for the real acceleration record will constitute the main skeleton of the record set, each selected record should have different characteristics to represent whole behavior range to have appropriate results. However, there are obstacles in finding suitable earthquake records as the input motions that assumed to take place in bedrock should have a V_{s30} (shear wave velocity calculated for the upper 30 m) value around 1500 m/s.

Firstly, PEER (Pacific Earthquake Engineering Center) strong ground motion database [26] is searched to form a set of earthquakes with a V_{s30} value greater than or equal to 1500 m/s. At the same time, shallow earthquakes with smaller EpiD (Epicentral distance to the station) values are tried to be selected. These values are important in terms of being appropriate to the characteristics of devastating earthquakes that are inconsistent with case study. However, only 17 records are founded in the database.

This shows that there are significant difficulties in finding the appropriate acceleration records, because PEER is the center of the richest database. In the present literature, it is seen that Beyaz [13] has given soil profiles of 56 acceleration recording station with base rock information. In these profiles, it is observed that there may be base rocks with shear wave velocity values like 1000-1200 m/s without reaching 1500 m/s velocities. On the basis of this, the search filters are replaced with speeds higher than 1300 m/s to stay in a safe zone. Although, the number of records obtained becomes higher, many records could not be used due to the very low PGA and magnitude values. This situation was an important problem because records with PGA up to 0.6g is needed.

Since the PEER database is not sufficient in the ongoing process, databases of other regions and countries are investigated. They are designated as Japan [27], USA [28], New Zealand [29], Italy [30] and Europe database [31, 32]. As a result of all these efforts, highest possible portion of the acceleration record set that established is obtained from the real earthquake records.

4.2. Records obtained by deconvolution

The insufficiency of the number of seismic acceleration records compatible with bed rock characteristics, necessitates some alternative solutions. One of these is the deconvolution (inverse convolution) technique. In order to perform this process, it is necessary to know the soil properties of the station where the surface earthquake record is taken. Motion at is recorded by the devices on the ground surface. In this case, if the effect of the soil layers up to the surface is accepted as the transfer function, and the surface earthquake record as the output function, the initial form of the record can be determined by the inverse convolution calculations [13]. This process is called deconvolution. In scope of the study, these calculations are made using the ProShake program [33].

4.3. Records obtained by scaling

Although the deconvolution technique has enriched the acceleration record set, it is thought that some earthquakes may be used as scaled since the number of predicted records is not reached. The most important factor to be taken into account when performing this process is that the scale value to be used should be at a level that does not disrupt the characteristic of the current recording. Intensity and frequency content of ground motions are important characteristics which have impact on their effects on structures [34]. Scaling only alters the intensity of the acceleration record, but not the frequency content. However, in literature it is observed that higher intensity ground motions tend to have frequency content with higher period waves [35]. Therefore, with scale factors too different then unity, it is possible to move away from natural results.

It is recommended that the scaling process on actual earthquake records does not exceed certain limits. In literature some suggestions are given: When the acceleration record is scaled outside the range of 0.25-4.00, it is noticed that the spectral behavior of the records becomes uncertain [36]. It is recommended that the maximum value of scale factor is 4.0 for linear analyses and the factor should be in the range of 0.5-2.0 in the nonlinear analyses. Also, this coefficient should not be more than 2.0 for liquefaction studies [37–39].

Considering all these, an appropriate scale range should be determined. The scaling of existing records without disturbing the frequency content-amplitude relationship of the earthquake such as PGV/PGA, mean period and predominant period is seen important in terms of achieving accurate results.

In order to avoid any alteration in the frequency-amplitude relationships, it is found appropriate to select maximum and minimum scale values. This selection is done by visual inspection and trial-error approach in scope of the study. The records are scaled by different values and their frequency content-amplitude relation is examined by using (PGV) and different frequency content parameters (PGV/PGA ratio, predominant period (T_P), mean period (T_M) [40]) graphs. The frequency content-amplitude relation of the scaled records with factors in the range of 0.7-1.30 are observed to be in consistent with unscaled natural earthquakes.

Fig. 2, shows the relationships between amplitude (PGV) and frequency content parameters for the scaled and natural earthquakes used in the study. When these relations are examined, it is seen that there are not any cases such as the separation of the scaled earthquakes from the natural earthquakes, scaled earthquakes in the extremities of the graphs. This shows that the frequency-amplitude relationship of acceleration records is not impaired by scaling. The reason for using PGV as amplitude parameter is that this parameter is shown as the one with highest correlation with other acceleration record parameters in the literature [41, 42] and PGV has a relatively high level of correlation with the seismic damage of various types of structures [43, 44].

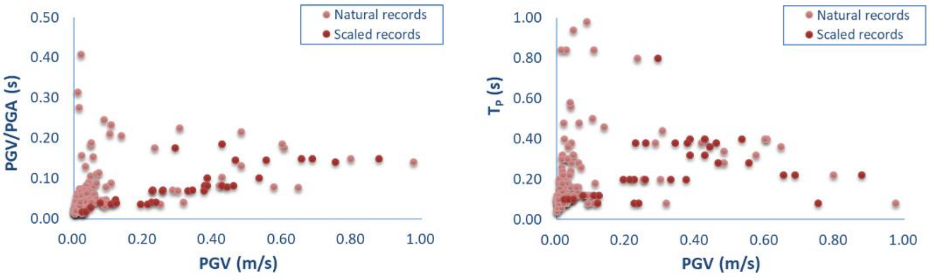

a) PGV/PGA and PGV relation

b) T_P and PGV relation

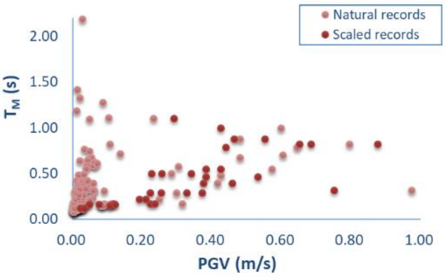

c) T_M and PGV relation

Fig. 2 The relationships between intensity and frequency content parameters for the scaled and natural earthquakes

4.4. Synthetic records

Although the acceleration record set reached a certain abundance by natural, scaled and records obtained using deconvolution method, it was not possible to reach desired quantities. This is due to the fact that the number of actual earthquake records and the recordings produced by the deconvolution technique are relatively low. Since the use of the scaling method many times may result in the dominance of the same records in the set, the addition of synthetic recordings seems to be a necessity.

Compatibility of the produced synthetic recordings with the natural earthquake characteristics is given importance. Produce earthquake records in the base rock feature is one of the first considerations. For this purpose, the use of the SeismoArtif program is deemed suitable since the base rock feature is provided in the software [45]. The acceleration record can be produced by entering hard rock value in the program, and a specific magnitude value can also be defined. The harmony of the produced synthetic records with the natural records is investigated graphically on the basis of PGV and PGV/PGA, T_P (predominant period) and T_M (mean period) relations (Fig. 3). A number of different acceleration records are generated and the ones that are far away from natural records in any of the 3 relations (indication of incompatibility in frequency content) are eliminated.

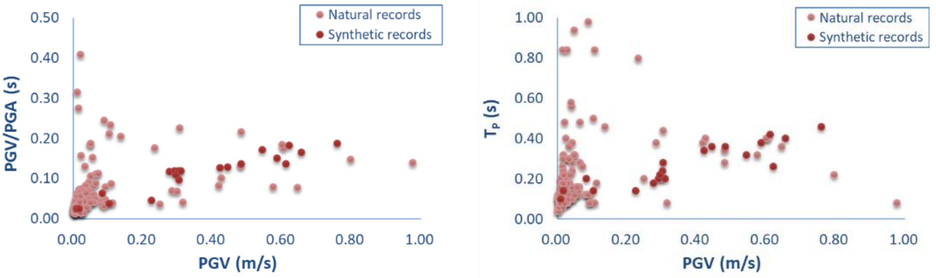

a) PGV/PGA and PGV relation b) T_P and PGV relation

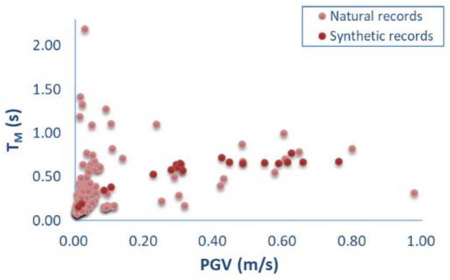

c) T_M and PGV relation

Fig. 3 The relationships between intensity and frequency content parameters for the synthetic and natural earthquakes

4.5. Established acceleration record set

As a result of the explained studies, a set with 84 earthquake acceleration records is obtained by four different methods. In this context, it is thought that the acceleration records are both according to basement rock definition and having different amplitude and frequency content. Precedence is given to the real earthquake records. After these, deconvolution, scaling and synthetic records are used with mentioned priority order. The properties of the used input ground motions are given in the supplementary spread sheet files attached to the article under “Used Ground Motion Info” page.

In each PGA group, attention is paid to find an acceleration record with different properties in terms of fault type, earthquake characteristics, frequency content, and generation method (natural-deconvolution, scaled, synthetic). Due to the low number of natural acceleration records with desired base rock properties, the establishment of the acceleration record set is a very time consuming and demanding process.

These 84 records which are compatible with base rock definition, are used to determine output acceleration records on the surface of the given 100 soil profiles using ProShake software. This way 8400 acceleration records with different frequency content, amplitude and site classes are obtained. These output records are given in the 7 supplementary spread sheet files attached to the article. The files are divided due to the high sizes exceeding 150 MBs.

5. Soil amplification

One of the goals in establishment of this acceleration record set is the investigation of soil amplification for different soil profiles. Exemplary results of soil amplification for a soil profile are given in Fig. 4 for all 84 acceleration records. Amplification ratios for each of the 84 acceleration records for example profile (output/input spectral acceleration ratios for the corresponding period) are given in Fig. 4a. Although the values between 0 and 10 s were obtained in the analysis, the graphical values are given up to 4 s which includes significant amplification zone and the effective range of most of the engineering structures.

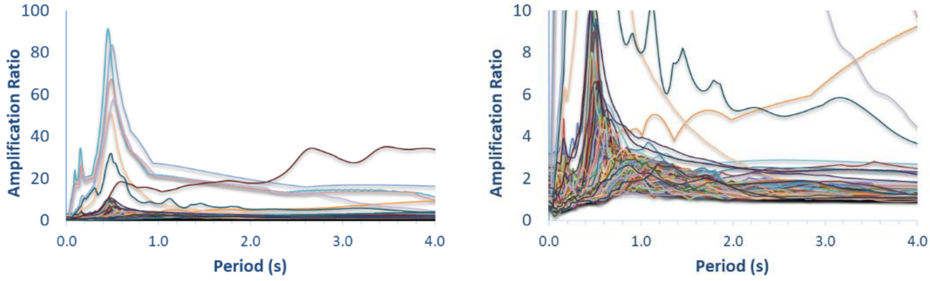

a) Soil amplification for all records b) Soil amplification (up to 10 folds)

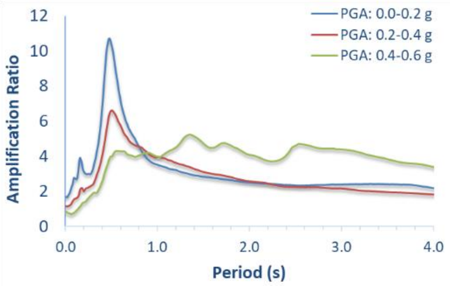

c) Average soil amplification for different PGA ranges

Fig. 4 Soil amplification values for all 84 records and averages for different PGA ranges

In figures, extreme cases of amplification are seen up to 90 times, which is for small amplitude waves. However, the most of the values are up to 10 times amplification which is illustrated in Fig. 4b. The period of the examined soil profile is 0.44 s, which is roughly the value where maximum amplification occurs for most of the records. The average values of the different acceleration records may be more useful to understand the behavior. Therefore, in Fig. 4c, the average values for different PGA ranges are given.

It is seen that the magnification ratios are lower as expected with the increase of the ground motion amplitude. Maximum average amplification is around 10.5 times for 0.0-0.2g PGA group. 0.2-0.4g PGA group follows with 6.5 average amplification. The 0.4-0.6g group has a smaller average amplification of approximately 5.2 at a different period and has significantly higher amplification values than the other groups for periods larger than roughly 1.0 seconds. It is attributable to the richness of higher magnitude records in terms of waves with larger period. Although, it is not given here, same behavior is observed for other soil profiles, as well.

6. Summary & conclusions

As there is a problem in finding acceleration records with chosen characteristics in literature, this study is conducted to broaden the ground motion records for the researchers. Firstly, a set of 84 input records are established in consistent with base rock properties. These records are used to determine output acceleration records on the surface of the given 100 soil profiles. This way an acceleration record set with 8400 records with different frequency content, amplitude and site classes are obtained and given as attachment to this article (for files http://dx.doi.org/10.17515/resm2019.116ea0209.ds). The main conclusions of the study are as follows:

- The present acceleration data recorded from real earthquakes are not sufficient to conduct some scientific studies like the current one. Additionally, it is hard or not possible to find ground motion records for extensive dynamic analyses of some structures, which is also previously stated in literature.
- Depth-average shear wave velocity relations are examined and given for sand and clay materials. It is seen that the coefficient of variation is getting smaller with increasing depth.
- Properties of devastating earthquakes in Turkey are investigated as a case study of an earthquake prone country. The mean depth of focus is found to be 18.61 km. It is observed that shallow earthquakes with strike-slip mechanism is the main characteristics of destructive Turkish earthquakes.
- Scaling real earthquake records in 0.7-1.3 range does not observed to alter the frequency-amplitude relationship.
- It is seen that soil amplification ratios are lower with the increase of the ground motion amplitude. Records with PGAs of more than or equal to 0.4 g are observed to have higher amplification ratios for waves larger than roughly 1.0 s periods when compared to records with smaller PGA. It is attributable to the richness of higher magnitude records in terms of waves with larger period.

Acknowledgement

The authors acknowledge that this study is supported by The Scientific and Technological Research Council of Turkey (TUBITAK) under the project titled as “Change of Earthquake Ground Motions Depending on Soil Properties” and Project No: 215M357.

References

[1] Kramer SL. Geotechnical Earthquake Engineering. Prentice-Hall, Inc. 1996. 653 p.
[2] Demirtas B, Bayraktar A, Dumanoglu A. Model updating effects on the seismic behavior of tall buildings under far and near-fault ground motions. Res Eng Struct Mater. 2017; 3(2):99–112.
[3] Rodriguez-Marek A, Bray JD, Abrahamson NA. An Empirical Geotechnical Seismic Site Response Procedure. Earthq Spectra. 2001; 17(1):65–87. https://doi.org/10.1193/1.1586167
[4] Hays W. Site Amplification of Earthquake Ground Motion. In: Third US National Conference on Earthquake Engineering. Charleston, South Carolina; 1986. p. 357–68.
[5] Seed HB, Romo MP, Sun JI, Jaime A, Lysmer J. The Mexico Earthquake of September 19, 1985—Relationships Between Soil Conditions and Earthquake Ground Motions. Earthq Spectra. 1988; 4(4):687–729. https://doi.org/10.1193/1.1585498
[6] Seed R, Dickenson SE, Riemer MF, Bray JD, Sitar N, Mitchell JK, et al. Preliminary Report on the Principal Geotechnical Aspects of the October 17, 1989, Loma Prieta Earthquake. 1990.
[7] Ansal A, Biro Y, Erken A, Gülerce Ü, Özçimen N. Seismic zonation in Istanbul: A case study. In: Geotechnical Earthquake Engineering and Microzonation Seminar. 2001.
[8] Tezcan SS, Kaya E, Engin Bal İ, Özdemir Z. Seismic amplification at Avcılar, Istanbul. Eng Struct. 2002; 24(5):661–7. https://doi.org/10.1016/S0141-0296(02)00002-0
[9] Bommer JJ, Douglas J, Strasser FO. Style-of-faulting in ground-motion prediction equations. Bull Earthq Eng. 2003; 1:171–203. https://doi.org/10.1023/A:1026323123154

[10] Ozmen HB, Inel M. Strength reduction factors for existing mid-rise RC buildings for different performance levels. Res Eng Struct Mater. 2018; 4(4):241–55. https://doi.org/10.17515/resm2018.60ea3107
[11] UBC-1997. Uniform building code. American Association of Building Officials, Whittier, CA. 1997.
[12] TBSC-2018. Turkish Building Seismic Code. Ministry of Environment and Urban Planning, Ankara; 2018.
[13] Beyaz T. Zemin Etkisinden Arındırılmış Deprem Kayıtlarına Göre Türkiye için Yeni Bir Deprem Enerjisi Azalım Bağıntısının Geliştirilmesi. Dissertation. Ankara University, Graduate School of Scence; 2004.
[14] Wikipedia-2016. Wikipedia web site [Internet]. 2016. Available from: https://tr.wikipedia.org/wiki/türkiye'deki_depremler_listesi
[15] Kandilli-2016. Kandilli Observatory web site [Internet]. 2016. Available from: http://www.koeri.boun.edu.tr/new/tr
[16] AFAD-2016. AFAD web sitesi [Internet]. 2016. Available from: http://www.deprem.gov.tr/tr/depremkatalogu
[17] AFAD. Disaster and Emergency Management Authority. Ankara, Turkey;
[18] Reynolds GH, Davis SJ. The structural geology of rocks and regions. USA: John Wiley & Sons Inc.; 1996.
[19] McGuire RK. Seismic ground motion parameter relations. ASCE J Geotech Eng Div. 1978; 104:481–90.
[20] Tso WK, Zhu TJ, Heidebrecht AC. Engineering implication of ground motion A/V ratio. Soil Dyn Earthq Eng. 1992; 11(3):133–44. https://doi.org/10.1016/0267-7261(92)90027-B
[21] XU L, HU J, XIE L. On Characteristics of Ground Motion Parameters for Special Long-Period Ground Motions. J Earthq Eng Eng Vib. 2008; 28(6):20–7.
[22] XU L, XIE L. Variations of Seismic Design Acceleration Amplitude with Depth for Underground Structures. World Inf Earthq Eng. 2009; 25(2).
[23] Tselentis GA, Danciu L. Probabilistic seismic hazard assessment in Greece - Part 1: Engineering ground motion parameters. Nat Hazards Earth Syst Sci. 2010. https://doi.org/10.5194/nhess-10-25-2010
[24] Kianoush MR, Ghaemmaghami AR. The effect of earthquake frequency content on the seismic behavior of concrete rectangular liquid tanks using the finite element method incorporating soil-structure interaction. Eng Struct. 2011. https://doi.org/10.1016/j.engstruct.2011.03.009
[25] Ozmen HB. Developing hybrid parameters for measuring damage potential of earthquake records: case for RC building stock. Bull Earthq Eng. 2017; 15(7).
[26] PEER. Pacific Earthquake Engineering Research Center [Internet]. 2016. Available from: http://peer.berkeley.edu/smcat/index.html
[27] Cosmos-2016. Global Component of the Center for Engineering Strong Motion Data [Internet]. 2016. Available from: https://strongmotioncenter.org
[28] USGS-2016. United States Geological Survey [Internet]. 2016. Available from: https://earthquake.usgs.gov/data/
[29] GeoNet-2016. New Zealand Strong Motion Database [Internet]. 2016. Available from: http://quakesearch.geonet.org.nz/
[30] Itaca-2016. Italian Accelometric Archive [Internet]. 2016. Available from: http://itaca.mi.ingv.it/
[31] ORFEUS-2016. Observatories & Research Facilities for European Seismology [Internet]. 2016. Available from: https://www.orfeus-eu.org
[32] ESD-2016. The European strong motion database [Internet]. 2016. Available from: http://www.isesd.hi.is/esd_local/frameset.htm
[33] EduPro Civil Systems. ProShake [Internet]. 2016.

[34] Ozmen HB, Inel M, Senel SM, Kayhan AH. Load carrying system characteristics of existing turkish rc building stock. Int J Civ Eng. 2015; 13(1).
[35] Rathje EM, Faraj F, Russell S, Bray JD. Empirical Relationships for Frequency Content Parameters of Earthquake Ground Motions. Earthq Spectra. 2004; 20(1):119–44. https://doi.org/10.1193/1.1643356
[36] Yağcı B. Microzonation methodologies and a study for Balikesir. Dissertation. Balıkesir University, Institute of Science, Department of Civil Engineering; 2005.
[37] Vatansever S. Gerçek Deprem Kayıtlarının Ölçekleme Yöntemlerinin Karşılaştırılması. Dissertation. Gebze Yüksek Teknoloji Enstitüsü; 2011.
[38] Vanmarcke EH. State-of-the-Art for Assessing Earthquake Hazards in the United States: Representation of Earthquake Ground Motions – Scaled Accelerograms and Equivalent Response Spectra. Vicksburg, Mississippi, USA; 1979.
[39] Krinitzsky EL, Chang F. K. State-of the-Art for Assessing Earthquake Hazards in the United States: Specifying Peak Motions for Design Earthquakes. Mississippi, USA; 1977.
[40] Rathje EM, Abrahamson NA, Bray JD. Simplified Frequency Content Estimates of Earthquake Ground Motions. J Geotech Geoenvironmental Eng. 1998; 124(2):150–9. https://doi.org/10.1061/(ASCE)1090-0241(1998)124:2(150)
[41] Amiri GG, Dana FM. Introduction of the most suitable parameter for selection of critical earthquake. Comput Struct. 2005;
[42] Ozmen HB, Inel M. Damage potential of earthquake records for RC building stock. Earthq Struct. 2016; 10(6). https://doi.org/10.12989/eas.2016.10.6.1315
[43] Avşar Ö, Özdemir G. Response of Seismic-Isolated Bridges in Relation to Intensity Measures of Ordinary and Pulselike Ground Motions. J Bridg Eng. 2011;
[44] Avşar Ö, Yakut A, Caner A. Analytical fragility curves for ordinary highway bridges in Turkey. Earthq Spectra. 2011. https://doi.org/10.1193/1.3651349
[45]SeismoArtif-2016. SeismoArtif [Internet]. 2016. Available from: http://www.seismosoft.com/seismoartif

ABSTRACTING / INDEXING

The international journal of Research on Engineering Structures and Materials (RESM) is currently Absracted/Indexed by CrossRef, Google Scholar, Universal Impact Factor, Scientific Indexing Service, Research Bible, CiteFactor, Electronic Journal Library, Open Academic Journals Index, Global Impact Factor, Directory of Research Journals Indexing, Materials Science & Engineering Database (ProQuest) Engineering Journals (ProQuest), ULAKBİM TR Index (Tubitak) and under evaluation by many other respected indexes.

Check web site for current indexing info.

Research on Engineering Structures & Materials

CONTENT

Research on
Engineering
Structures & Materials

Research Group